Apertureless SNOM: A New Tool for Nano-Optics

THÈSE N° 3073 (2004)

PRÉSENTÉE A LA FACULTE SCIENCES DE BASE

Institut de physique des nanostructures

SECTION DE PHYSIQUE

ÉCOLE POLYTECHNIQUE FÉDÉRALE DE LAUSANNE

POUR L'OBTENTION DU GRADE DE DOCTEUR ÈS SCIENCES

PAR

Alpan BEK

M.Sc. in Physics, Bilkent University, Turquie
et de nationalité turc

acceptée sur proposition du jury:

Prof. K. Kern, directeur de thèse
Prof. A. Fiore, rapporteur
Prof. V. Sandoghdar, rapporteur
Prof. J. Weber, rapporteur

Lausanne, EPFL

2004

“Dedeeem” Muammer Hoca’ya

ve

“Anânecim” Süedanım’a

yaşamak şakaya gelmez,
büyük bir ciddiyetle yaşayacaksın
bir sincap gibi mesela,
yani, yaşamın dışında ve ötesinde hiçbir şey beklemeden
yani, bütün işin gücün yaşamak olacak.

yaşamayı ciddiye alacaksın,
yani, o derecede, öylesine ki,
mesela, kolların bağlı arkadan, sırtın duvarda,
yahut, kocaman gözlüklerin,
beyaz gömleğinle bir laboratuvarda
insanlar için ölebileceksin,
hem de yüzünü bile görmediğin insanlar için,
hem de hiç kimse seni buna zorlamamışken,
hem de en güzel,
en gerçek şeyin yaşamak olduğunu bildiğin halde.

yani, öylesine ciddiye alacaksın ki yaşamayı,
yetmişinde bile, mesela, zeytin dikeceksin,
hem de öyle çocuklara falan kalır diye değil,
ölmekten korktuğun halde ölüme inanmadığın için,
yaşamak, yani ağır bastığından.

Nazım Hikmet Ran
(1947)

Abstract

In this thesis a new scanning near field optical microscope based on an apertureless scattering technique is introduced for resolving optical properties of surfaces with lateral resolution reaching 10 nm and better.

The construction of the instrument is based on a dynamic mode operating atomic force microscope (AFM) which is coupled with a sophisticated heterodyne interferometric optical detection system. A continuous wave (cw) laser beam is focused onto the apex of the metallic or dielectric AFM tip. The backscattered light is collected and interfered with a reference beam which is slightly shifted in frequency with respect to the scattered beam. The interfering signals are detected by a fast avalanche photodiode. The result is a temporal beat modulation at the shift frequency. The scattered light consists of two parts of different spatial origin. One of them is the near field that contains information belonging to a very small vicinity of tip apex interacting with surface. The second part is the far field part which comes from parasitic scattering along the illuminated tip body and the sample surface. By demodulating the beat signal at higher harmonics of the tip vibration, the far field part can be suppressed effectively, leaving only the near field information of the surface-tip interaction. By raster scanning the sample under the AFM tip, information about the amplitude and phase of the near field belonging to the surface is obtained simultaneously with topography.

This new apertureless scanning near field optical microscope (***a*-SNOM**) features several advantages over the well-known aperture SNOM: High resolution limited essentially only by the tip apex dimension, and effective background suppression. Particular care has been taken in the operation settings of the AFM, since they are shown to be one of the sources of artifacts in the detected signal due mechanical nature of the AFM. When proper conditions are met, these mechanical interaction artifacts are minimal and the *a*-SNOM produces essentially only optical information. The demonstration of the *a*-SNOM operation on Au pattern on glass surface and Ag colloid on Si surface systems show that a high sensitivity to material contrast as well as a high spatial resolution is achieved.

Résumé

L'objet de ce travail de thèse est le développement d'un nouveau microscope optique en champ proche à balayage. Le principe de fonctionnement de cet appareil repose sur une technique de diffusion dite *apertureless* qui permet l'étude des propriétés optiques de surface avec une résolution spatiale inférieure à 10 nm.

L'instrument est construit autour d'un microscope à force atomique (AFM) fonctionnant en mode dynamique, couplé à un système de détection par interféromètrie hétérodyne novateur. Un faisceau laser continu (cw) est focalisé à l'apex de la pointe métallique ou diélectrique de l'AFM. La lumière rétrodiffusée est collectée et interfère avec un faisceau de référence dont la fréquence est légèrement décalée par rapport à celle du faisceau diffusé. Le signal résultant, un battement à la fréquence de décalage, est détecté par une photodiode rapide à avalanche. La lumière diffusée est la superposition de deux contributions d'origines spatiales différentes. L'une d'elles est le champ proche qui contient l'information correspondant au voisinage immédiat de la pointe en interaction avec la surface. L'autre contribution est liée au champ lointain parasite diffusé par l'ensemble de la pointe et par l'échantillon. La démodulation du signal de battement à des fréquences correspondant aux harmoniques élevées de la vibration de la pointe permet de supprimer efficacement le signal de champ lointain et, ainsi, d'extraire l'information de champ proche liée à l'interaction pointe-surface. En balayant l'échantillon sous la pointe de l'AFM, l'amplitude et la phase du champ proche de surface peuvent être enregistrées en même temps que la topographie de l'échantillon.

Ce nouveau microscope optique en champ proche à balayage *apertureless* (*a*-SNOM) possède plusieurs avantages par rapport à la configuration classique *aperture*: sa haute résolution est essentiellement limitée par les dimensions de l'apex de la pointe et il permet de supprimer efficacement le fond parasite. Un soin particulier a été porté à la détermination des paramètres d'opération de l'AFM, ceux-ci pouvant être une source d'artefacts liés à la nature mécanique du dispositif. Dans ces conditions, ces artefacts d'origine mécanique sont extrêmement réduits et l'information délivrée par le *a*-SNOM est quasiment exclusivement d'origine optique. Des expériences réalisées sur différents échantillons (motifs d'or déposés sur une surface de verre, colloïdes d'argent sur une surface de silicium) ont permis de démontrer un contraste optique très élevé entre matériaux de natures différentes ainsi qu'une excellente résolution spatiale.

Özet

Bu tezde, yüzeylerin optik özelliklerini 10 nm ve/veya altında yatay konumsal çözünürlükle incelemeye yarayan, optik açıklıksız saçılma tekniğini temel alan bir yüzey yakın alan optik tarama mikroskopu gerçelleştirilmiştir.

Aygıt, dinamik bir atomik kuvvet mikroskopuna (AKM) karmaşık bir frekans farklı optik girişim düzeneğinin eklenmesiyle oluşturulmuştur. Bir sürekli-dalga laseri metal veya dielektrik bir AKM iğnesinin ucuna odaklanır. Geri-saçılan ışık toplanarak, frekansı kendi frekansına göre biraz kaydırılmış olan bir referans ışınıyla giriştirilir. Girişim sinyali hızlı bir çığ-etkisi fotodiyotu ile ölçülür. Sonuçta kaydırma frekansına sahip zamansal bir sinyal dalgalanması ortaya çıkar. Saçılan ışık iki konumsal kökene dayanır. Bir tanesi, örnek yüzeyi ile AKM iğnesinin ucundaki çok küçük bir bölgenin etkileşimine ait olan yakın-alandır. İkincisi ise ışığın aydınlattığı iğnenin gövdesi ile yine aydınlatılan geniş örnek yüzeyinden saçılan parazitik uzak-alandır. Sinyalde sözü geçen dalgalanmanın iğne titreşiminin yüksek dereceli harmoniklerindeki genliği takip edilerek bu uzak-bölge alanından kaynaklanan etki bastırılabilir. Geriye kalan yalnızca iğne ucu-yüzey etkileşiminden doğan yakın-alan bilgisidir. Bu AKM iğnesi yüzey üzerinde taranarak yüzeyin yakın-alanına ve fazına ait haritalar, yüzey coğrafyası ile eşzamanlı olarak elde edilir.

Yeni geliştirilen bu açıklıksız tarama yakın-alan optik mikroskopunun (a-TOM) iyi bilinen açıklıklı tarama yakın-alan optik mikroskopuyla (TOM) karşılaştırıldığında ortaya çıkan bir takım üstün özellikleri şu şekilde sıralanabilir: Yalnızca tarama iğnesinin ucunun büyüklüğü ile sınırlı olan çok yüksek bir yatay konumsal çözünürlük ve oldukça etkin bir uzak-alan indirgeme gücü. AKM'nin çalıştırılışı sırasinda bir takım işletim ayarlarına özellikle dikkat edilmelidir çünkü AKM'nin mekanik işletim yapısından ötürü a-TOM sinyalinde yan etkilere neden olabilecekleri ortaya çıkmıştır. Doğru ayarlar tutturulduğunda mekanik etkileşim yan etkileri en az düzeye iner ve a-TOM yüzeylerden arı optik bilgiyi toplar. a-TOM'un işlevinin cam üzerinde şekillendirilmiş altın ile silisyum üzerine kondurulmuş kolloidal gümüş örneklerin üzerinde gösterilmesi sırasında malzeme türüne karşı yüksek duyarlık ve çok yüksek bir yatay konumsal çözünürlük

başarılmıştır.

Contents

Chapter 1

Introduction

Revealing the properties of materials constituting surfaces, at a high spatial resolution, is the central interest in this work. Light-matter interaction has proven to be an effective means in acquiring information about materials in the last century. More recently, in the last couple of decades, surface scanning techniques like "scanning tunneling microscopy" (STM) [1] and "atomic force microscopy" (AFM) [2], have been introduced as immensely successful ways of investigating surfaces at a spatial resolution down to even sub-atomic dimensions. They do provide, however, no optical information.

The quest for extraction of optical material properties with a finely resolved spatial dependence, has forced researchers to improve optical microscopy towards obtaining the smallest possible focal diameter. The diffraction limit was reached in optical microscope instrumentation. Further, the introduction of monochromatic, coherent, and high intensity light sources, i.e. lasers, into optical microscopy was welcomed by many researchers of all fields from material science to biology. "Confocal scanning laser microscopy" (CSLM) [3, 4] equipped with spectroscopic instrumentation has become the current state-of-the-art optical microscope for research from live cells [5] to single molecules [6] and related processes like fluorescent resonant energy transfer (FRET) [7].

In the classical reflective-diffractive optical instrumentation, the limit for the smallest resolvable optical feature size is the diffraction limit of light, that is $\lambda/2n$. In order to achieve high resolution, one needs smaller wavelengths λ and/or higher refractive indices

n of the media. Efficient reduction of the focal diameter is not practical due to these limitations.

Profiting from the well-established surface scanning techniques, new optical technologies were developed like the "scanning near-field optical microscope" (SNOM) [8–12] for achieving higher resolution optical experiments, about one order below the far-field diffraction limit in the visible wavelength range of the electromagnetic continuum. Since 1984 with the advent of SNOM an intriguing alternative to diffractive optics has been widely established in many branches of science. It allowed to push the spatial resolution to values of approximately $\lambda/15$ but not more, due to throughput problems at the aperture. [13] Thus for visible light the typical resolution achieved by SNOM lies in the range of 50 nm to 100 nm.

The fundamental goal of my research was an optical spatial resolution of 10 nm and better. For achieving this goal a novel class of instrument has been suggested in the mid 1990s. It is based not upon transmission through an aperture but on the strongly spatially localized field enhancement at sharp geometrical features such as the now widely used STM and AFM tips. [14, 15] Theoretical calculations have predicted a field enhancement of more than 3 orders of magnitude under favorable conditions. [16]

From early on two main versions of this field enhancement based near field optics tool have been suggested. Early reports of huge Raman scattering cross-section enhancement described the use of *static* field enhancement under an STM or metallized AFM tip. [17–23] That is, the tip-sample distance was not varied as for example in the dynamic mode AFM technique, which present an alternative approach to using field enhancement. The static approach requires extreme field enhancement factors, similar to what has been observed in "hot spots" in surface enhanced Raman spectroscopy (SERS), [24–26] to overcome the parasitic signal from the immediate neighborhood of the sample area of interest. The sporadic nature of these "hot spots" imposes severe limitations on the feasible use of static enhancement based instruments as routine laboratory equipment. Recent reports estimate only $\sim 20\%$ yield at the very best of identically prepared tips

to show enhancement factors sufficient to see any effect at all. [27] In contrast, the *dynamic* mode variant relies on the modulation effects on the observed signal which in combination with the strong non-linearity of the field enhancement as a function of tip-sample distance results in higher harmonics coming from exclusively the area of interest to separate the parasitic signal. This variant of a near-field microscope can tolerate lower field enhancement factors than the static one and is thus much better suited to become a routine method for nano-optical investigations.

From the outset of my thesis work, I wanted the class of samples to be not restricted to transparent samples. In particular, semiconductor and metallic substrates are frequently used in solid state research and their surfaces can be structured to feature sizes ranging from few nm to several μm. Hence, a non-negotiable specification was that the instrument has to be able to study such opaque samples. This condition limits the options for optical illumination and collection choices. Clearly a commercial, short working distance objective lens system with a high numerical aperture (NA) is not possible due to geometrical reasons. Instead, a long working distance objective at a modest angle above the sample surface has to be used to allow the AFM or STM field enhancement tip to be placed in the focus.

Another requirement for this machine was that it operates under ambient conditions. This is not a strict limitation; in principle a similar machine can be also envisioned, operating under UHV and/or low temperature conditions.

In the implementation I first studied the static field enhancement option as it promised in particular to give characteristic spectroscopic signatures from the local objects under investigation, as mentioned above. It turned out, however, that the achievable enhancement factors under everyday conditions in the lab are in the range of 10 to 100 at best, which is not sufficient to overcome the detector noise limit and efficiently suppress the parasitic signal. While some groups have opted to investigate the intricacies of the tip manufacturing process itself to achieve the necessary field enhancement more frequently [28,29] I decided to switch to the dynamic field enhancement

technique and implemented an apertureless scanning near-field optical microscope (*a*-SNOM) based on a commercial AFM with home built interferometric detection [30] of the complex optical signal. The apertureless near-field enhancement approach to nano-optics has been applied in the infrared and visible by F. Keilmann et al. [31, 32] With interferometric amplification, their instrument was shown to be able to extract material specific optical amplitude and phase contrast from surfaces with high lateral resolution. Their initial results were motivating to develop a similar instrument with additional and improved features.

The interferometrically achieved high sensitivity in *a*-SNOM means freedom from requirement of resonant enhancement at the tip-sample interaction. In practice, nearly any sharp dielectric or metallized tip was found to be useable as a local probe, contrary to techniques based on very high but sporadic field enhancement factors like SERS. This reflects the potential of *a*-SNOM as a reliable instrument for routine laboratory use. Due to the interferometric detection technique, *a*-SNOM is not designed for spectroscopic analysis of the detected radiation. However, the wavelength and polarization dependence of near fields enriches *a*-SNOM as a versatile instrument. [32–36]

In this thesis, I report on the successful development and operation of *a*-SNOM as an alternative near-field optical technique for solid state research on surfaces. The second chapter gives a background on near field optics and microscopy. The third chapter discusses theoretical near field amplitudes in a quasi-static dipole approximation. The fourth chapter is the description of the *a*-SNOM setup based on commercial AFM, interferometry optics and RF circuitry. In the fifth chapter I report on results of detailed characterization and performance tests I made on *a*-SNOM. In the sixth chapter I demonstrate the high spatial resolution and sensitive material contrast achieved by *a*-SNOM on sample surfaces and interpret results in view of control experiments done for testing topography related artifacts. And in the last chapter I give my conclusion.

Chapter 2

Optics at the nm scale – near field microscopy

Nanostructures composed of up to a few hundreds of atoms can be produced in the laboratories in a well controlled manner thanks to chemical and physical fabrication strategies. [37–39] While the spectrum of materials technologically structured at the nm scale in the laboratories is broadening, the interest on the functionality of biological molecules and systems is also growing rapidly. The size of sub-cellular biological building blocks is often also in the nm range. Moreover, the ever growing need in information processing has also demands on reduction of physical bit size in information storage and computation for high speed and small storage size requirements. Therefore, the feature sizes in ultra large scale integrated electronics circuitry are getting smaller down to the few nm scale. The necessity of investigating properties of matter at the nm scale has been growing and the trends show no deviation for the next years.

The experimental methods that have been used to investigate matter at μm level and slightly less since many years continue to constitute the basics of investigation of matter also at the nm scale. Many of the mechanical, electronic, optical, magnetic, and other techniques, that used to be applied to bulk materials have been modified in applications to allow for high enough spatial resolution for nanoscale materials. The scanning probe microscopy (SPM) [40, 41] techniques have evolved because of this need

for high resolution. The scanning probe techniques have been implemented in almost all of the aforementioned material characterization methods: AFM as a mechanical, STM as an electronic, MFM [42] as a magnetic and aperture based SNOM as an optical tool for the nanoscale. While in STM and AFM even atomic resolution has been achieved, in MFM the resolution is about a few nanometers and in SNOM in the visible about 50 to 100 nm could be achieved so far, in the infrared even less.

The ideal case for a nano-optical experiment is the one in which a certain nanoscale target in an ensemble of nanoscale objects could selectively be excited, and the scattered optical field could selectively be detected.

The road towards a high resolution optical microscope lies in revealing the near-field properties of matter. The optical near fields present at very close proximity of matter usually contain information about the matter at the highest spatial resolution. That fact indirectly implies that the information has to be collected from within this close proximity of the matter to achieve highest resolutions, otherwise the collected data contains mainly far field information on a larger scale landscape of the material, as large as the diffraction limited spot size of the optical instrument.

2.1 Light-matter interaction

2.1.1 Elastic scattering

Rayleigh scattering is the prime example of elastic or energy conserving scattering processes. In other words, it is a process in which the incoming light onto material and outgoing light from the material have the same energy.

The origin of the Rayleigh scattering: In the 1850s James Clerk Maxwell summarized and extended the empirical knowledge on electromagnetism in a set of mathematical equations. He postulated a set of equations between the electric field, magnetic field, electric polarization, magnetization, and static and dynamic charges, from which all the electrodynamic phenomena could be explained together with the material properties. In

general at the boundary between two domains of different media properties (polarizability and permeability) these give rise to a new set of equations, the so-called boundary conditions. The boundary conditions explain one example of elastic optical phenomena well-known to everyday life: Visible specular reflection at smooth surfaces, as well as diffuse reflections at rough surfaces. More generally, any energy conserving interaction process of light with matter into any direction is called elastic scattering.

Light-matter interaction is usually studied in two spatial domains, qualitatively classified into the far and the near fields with an ill-defined intermediate region. Starting from the time independent vector potential [43]

$$\mathbf{A}(\mathbf{r}) = \frac{\mu_0}{4\pi}\int \mathbf{J}(\mathbf{r}')\frac{e^{ik|\mathbf{r}-\mathbf{r}'|}}{|\mathbf{r}-\mathbf{r}'|}d^3r'. \tag{2.1}$$

for a current distribution $\mathbf{J}(\mathbf{r}')$, where $k = \omega/c$ is the wavenumber, the electric and magnetic fields $\mathbf{B}$, $\mathbf{E}$ given by

$$\begin{aligned}\mathbf{B} &= \nabla \times \mathbf{A}\\ \mathbf{E} &= i\frac{c}{k}\nabla \times \mathbf{B}\end{aligned}$$

can be calculated from the integral in Eq. 2.1. The harmonic time dependency $e^{-i\omega t}$ shall be kept in mind for the full description of $\mathbf{A}(\mathbf{r},t)$ and the fields $\mathbf{B}$ and $\mathbf{E}$. If the source dimensions are of order d and the wavelength is $\lambda = 2\pi c/\omega$, there are three spatial regions of interest:

$$\begin{aligned}\text{The near field zone}: &\quad d \ll r \ll \lambda,\\ \text{The intermediate zone}: &\quad d \ll r \sim \lambda,\\ \text{The far field zone}: &\quad d \ll \lambda \ll r.\end{aligned}$$

The shaded zone in Fig. 2.1 is an illustration of the near field zone. In the near field zone where $r \ll \lambda$ (or $kr \ll 1$ since $\lambda = 2\pi/k$) the exponential in Eq. 2.1 can be approximated

by 1. Then the vector potential and hence the fields become quasi-stationary, oscillating harmonically as $e^{-i\omega t}$, but otherwise static in character. In the far field zone where $r \gg d$

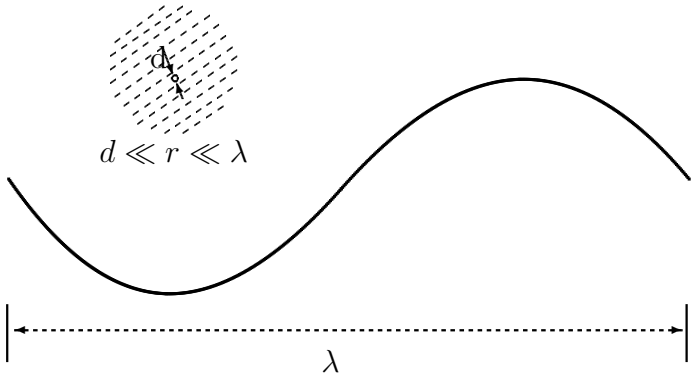

Figure 2.1: An illustration of the near field zone around an object of dimension d and a radiation wavelength λ. The shaded volume is an illustration of the near field zone with the condition $d \ll r \ll \lambda$.

it is adequate to approximate:

$$|\mathbf{r} - \mathbf{r}'| \simeq r - \mathbf{n} \cdot \mathbf{r}'$$

where $\mathbf{n}$ is a unit vector in the direction of $\mathbf{r}$. By focusing the interest on the leading term kr, the inverse distance in Eq. 2.2 can be replaced by r. Then the vector potential becomes

$$\lim_{kr\to\infty} \mathbf{A}(\mathbf{r}) \quad = \quad \frac{\mu_0}{4\pi}\frac{e^{ikr}}{r}\int \mathbf{J}(\mathbf{r}')e^{ik\mathbf{n}\cdot\mathbf{r}'}d^3r'.$$

The factor e^{ikr}/r simply describes an outgoing spherical wave whose strength is given by the integral of the source volume. Such a vector potential leads to propagating, radially transverse fields $\mathbf{E}$ and $\mathbf{B}$ at the far field zone.

2.1.2 Inelastic scattering

In inelastic scattering some portion of the energy of incident photons is either dissipated in the matter or some amount of energy is gained from the matter. The incoming light energy, i.e. frequency, differs from the outgoing light energy, i.e. frequency, by the

amount of this dissipated or gained energy. The energy of the photons, is not conserved. Photoluminescence and Raman scattering are examples of inelastic scattering. When spectrally analyzed, the absolute energy of the outgoing photons or the energy differences between the incident and scattered photons correspond to material specific internal energy levels which can be electronic states in atoms and molecules, excitonic states in semiconductors, vibrational and rotational states in molecules, phononic states in crystals, etc.

The spectroscopy of nanoscale materials is exciting because they exhibit properties which lie in the transition range between atomic/molecular and bulk properties. For example, size effects on the electronic properties of the material can be studied, and the size of the nano objects can be used as a tuning parameter to obtain a certain electronic property like the photoluminescence in case of semiconductors. [44]

Another interesting issue is that, the surface-to-volume ratio increases as the size of the material decreases. In the nm range, certain surface specific properties of matter, such as surface states, surface reactivity, catalytic activity, or optical surface enhancement effects emerge as very interesting mesoscopic phenomena for the study of theoreticians and experimentalists in all areas of natural sciences.

2.2 Principal approaches to high lateral resolution in optical imaging

Objects either of nm size geometry or having nm size range variations in their material properties are the subject matter of nanoscale science. When such nanoscale objects are sparsely dispersed (usually over a host surface or in a volume of suspension) it may be sufficient to study their light-matter interaction with usual far field methods like classical optical microscopy techniques. In the case of densely distributed nanoscale objects, optical experiments at the nanoscale require optical fields to be also confined to the same scale for obtaining sufficiently high lateral spatial resolution.

In developing strategies for working with nanoscale objects with light-matter interaction (frequently referred to simply as "nano-optics"), two basic approaches of obtaining ultimate lateral optical resolution have evolved: resolution by *confinement* of a light source to an aperture and resolution by strongly localized *field enhancement*, where this enhanced interaction volume acts as a source.

Generally, due to time reversal symmetry and reciprocity considerations, one can envision any such nanoscale *light source* also to act as a nanoscale light *detector*. Always, a nm size illumination source (or detector) is brought to within nm proximity of the matter under investigation, detecting the optical *near fields*. By raster scanning the nanosource over a surface, one can observe the light-matter interaction with a resolution at the order of the nanosource size.

Scaling the optical elements down to the nanoscale in order to be able to *confine* the optical fields to nanoscale is the fundamental idea of Synge, [8] who proposed to use a hole in a metal screen to confine the optical fields laterally to the extent of such an aperture. The realization of this approach is the aperture-based SNOM, [45, 46] which has been used successfully to study light emitted from nanoscale objects (which can be as small as a single molecule) also with spectroscopic resolution. [47–49]

An interesting alternative to light confinement is the optical *field enhancement*. It has been long known that the electric fields at the apex of conical tips diverge to infinite magnitudes, if the the apex can be infinitesimally sharp (thus restricting the product of optical energy density and volume to finite values as required by energy conservation.) With the advent of nm sized AFM tips, it became possible to envision their utilization as a nanoscale optical detectors/sources. The corresponding optical experiment uses classical elements to illuminate such a structure and to collect radiation emerging from it. Nevertheless, the resolution is achieved by a nanoscatterer that increases the optical interaction in its immediate vicinity a higher level than any other optical processes in the larger neighborhood. In Sec. 2.3.3, I choose a sharp AFM tip as an example for such a nanoscatterer. [17, 50–54]

In passing I note that the increased Raman scattering cross-section in SERS is believed to be a result of a rather similar effect as it involves the random formation of nanoscatterers at rough metal surfaces.

2.3 Experimental methods in nano-optics

In the classical reflective-diffractive optical instrumentation, the limit for the smallest resolvable optical feature size is the Rayleigh diffraction limit of the light, that is $1.22\lambda/(2n_0)$, where λ and n_0 are the wavelength of the light and refractive index of the medium respectively. [55] In order to achieve higher resolution, one needs light of shorter wavelength λ and/or higher refractive index media. Limiting factors for ever-increased resolution by such instruments include: the absorption edge of air at $\lambda/2 \sim 190\,\mathrm{nm}$, lack of transparent refractive materials for lenses and reflective coatings for mirrors in the deep UV, and last but not least the high energy of individual UV photons (several eV) which tends to destroy the very structures under investigation. Far field methods are currently reaching technological and budgetary limits in the industrial fabrication of the semiconductor structures where large scale lithographical patterns with structures of sizes below 90 nm need to be written. Similar limitations persist also in the far field technologies developed to read the individual data bits of such small size. Especially the end-user market can not afford the costs of integrating optical data reading technology with specialized deep UV material optical elements. So for all practical reasons a focal diameter of around 300 nm is the nominal size scale with which a scientist has to live using far field instrumentation such as confocal scanning laser microscopes at visible wavelengths. This size resolution limitation of the far field instrumentation is not necessarily an inability for investigating the optical processes taking place at the nanoscale. For studies in which very high spatial resolution is not of great importance, use of the far field instruments may even be advantageous. High solid angle collection of high NA objective lenses are very desired in cases of low photon numbers. Far field instruments are usually made of free space optical components, which makes it easy

to integrate them with minor modifications on the optical components to various other system such as spectroscopic units. Far field instruments are widely and successfully used in imaging, spectroscopy, interferometry, time resolved experiments, distance measurement, profilometry, ellipsometry, polarimetry and many other scientific applications and investigation methods.

Historically, far field instruments were realized much earlier than near field instruments. The first telescopes and microscopes indeed date back to times earlier than the full description of optics theories used today.

Individual and ensemble dispersive nanoscale objects, quantum dots, molecules can be investigated by far field instruments with spectroscopic and time resolution very efficiently. Some nanoscale effects can be revealed by analysis of the data acquired through far field methods. SERS is an example of how nanoscale optical phenomena may also be very effectively used by far field methods.

2.3.1 Confocal scanning laser microscopy

Laser scanning confocal microscopy is a type of microscopy in which a diffraction limited focal spot is realized and utilized effectively in imaging surfaces with very high far field resolution. The far field instrument achieving highest resolution is a variant of confocal microscope utilizing point spread function engineering via 4Pi confocal microscopy and stimulated emission depletion (4Pi-STED) [56, 57]. In the simplest form of confocal microscope, the illumination source is selected to be a certain line of either a gas or a solid state laser. The nearly perfect monochromaticity ensures the total cancellation of chromatic aberration effects on the focal spot. High NA objective lenses, usually oil or water immersion lenses, are used so that the entire half hemisphere volume angle can be used to achieve the diffraction limit. This focal spot of about one half wavelength diameter is then raster scanned on the surface by two scan mirrors, one for each lateral axis. The back scattered radiation from the surface is then taken out from the beam path by a beamsplitter and used to generate an image of the surface by plotting intensity bit by

bit on each scan point. Another option is to use the transmitted light when transparent samples are under investigation. In both cases the scattered light is collected *confocal* to the illumination objective—hence the name. It means, an aperture of appropriate diameter is overlapped exactly with the image position of the focal volume.

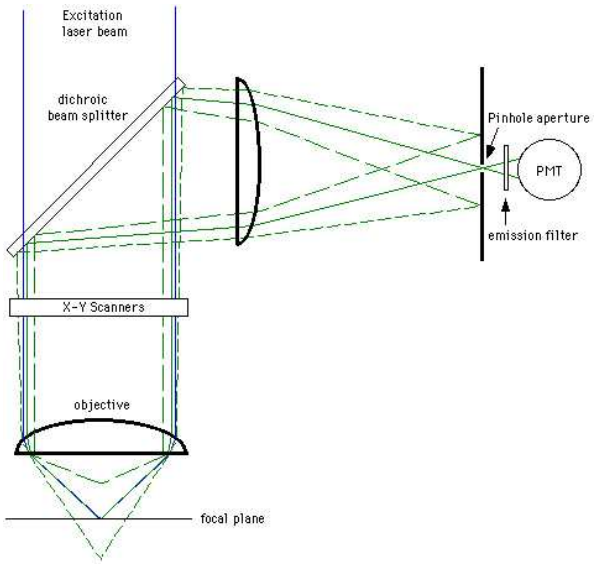

Figure 2.2: Diagram showing the reflective confocal geometry and spatial filtering in the depth of field for fluorescence microscopy with ultimate far field spatial resolution

The aperture in the collected beam path serves in addition as a spatial filter for the vertical direction. The confocally collected light from the sample is spatially filtered in the optical axis direction for discrimination signals coming from different heights in the optical axis around the focal volume. (See Fig. 2.2.) This way the collected signal is restricted to a volume which is defined by the focal depth, which is approximately twice the focal width. By moving the sample in the optical axis direction step by step and taking scans at every slice, one can compose a three dimensional image of the sample, similar to computer tomography in medicine.

Extension of confocal laser scanning microscopes with spectroscopic analysis capability has resulted in a valuable tool for scientists especially in biology. Following the specific signatures of special dye label molecules, 2D or 3D distribution of a certain molecule can be mapped with diffraction limited resolution. When the scattered beam is analyzed in both elastic and inelastic components, a three dimensional map of spec-

imens, for example live cells, can be made with spectroscopic content. For example, fluorescent dye molecules are used to selectively label certain functional groups in large biological specimens allowing to map out the spatial distribution of these functional groups.

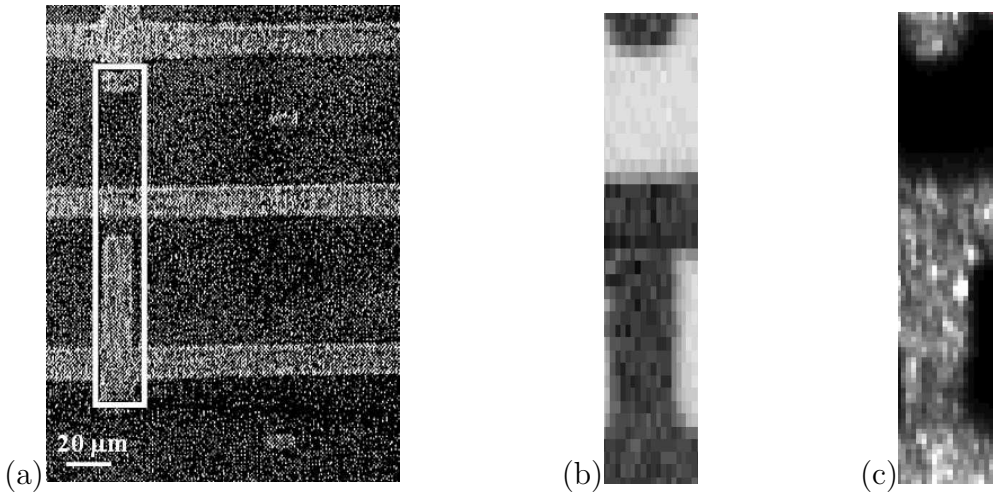

Figure 2.3: (a) SEM image of a carbon nanotube patterned Si surface. The box in the SEM image shows a representative $20\,\mu\mathrm{m} \times 100\,\mu\mathrm{m}$ area. From a similar area (b) an optical reflection CSLM image and (c) Raman CSLM image are taken. The Raman image is taken by integrating the $1500\mathrm{cm}^{-1}$ line of the carbon nanotube Raman spectrum.

Fig. 2.3 displays sample confocal Raman and reflection images taken from a carbon nanotube (CNT)-patterned substrate with a home-built version of a scanning confocal microscope during my initial investigation into the possibilities of static near field optical spectro-microscopy. Clearly visible are the spatial correlations of CNT patterns and the CNT Raman signal, as well as the unresolved structure inside the CNT covered area. Here, the near field enhancing tip of an apertureless SNOM could, in principle, probe the material structure locally with much enhance lateral resolution. Soon it became clear, however, that a confocal microscope setup might not be applicable as a method to observe spectroscopic signals with nm lateral resolution from opaque sample surfaces—mainly due to the insufficient focussing and collection power of the objective, which must operate at large working distances. Even for thins films deposited on and observed through transparent samples, which allows for the ultimate confocal resolution and collection power, only the most robust and strong Raman scattering molecular

species have been possible to investigate so far. [27, 58] For these reasons, I decided to implement a dynamic version of a near field enhancing optical microscope.

2.3.2 Near field-confining techniques (SNOM)

Basics

Scanning near-field optical microscopy (SNOM or NSOM) [9, 10, 12] is a surface characterization method for investigating the optical properties of the surfaces with a high spatial resolution. SNOM combines the idea of collecting the optical field at the "near zone" (see Ch.9 of [43]) of a surface of interest with the scanning probe microscopy (SPM) technique. (See for example [40] or [41] for a review of scanning probe techniques.) The original idea dating back to 1928 [8] envisioned observation of biological specimens behind a minute aperture of 10 nm size in an opaque film. 10 nm is obviously much smaller than the wavelength of the optical radiation at the visible range of the electromagnetic spectrum ($\lambda \sim 500\,\mathrm{nm}$), so this technique was suggested as an ultramicroscopic tool to overcome the resolution limit. The idea was to illuminate a planar surface of a sample through the 10 nm aperture by a very strong light source and raster scan the aperture while the transmitted optical radiation was collected by an optical microscope and its amplitude was plotted against the position of the aperture which should depend on the different opacities of the specimen at different aperture positions. The earliest experimental realization of this idea was only possible after 56 years. [10]

Although the basic idea is the same, the common SNOMs used in the laboratories today scan a miniature aperture at the metal coated end of tapered optical fiber instead of a planar opaque film. The fiber end with the aperture is brought into close proximity of a material surface while optical radiation is sent through the fiber and the aperture to the surface. The fiber end is usually machined to much smaller diameters than that of the original fiber ($\sim 125\,\mu\mathrm{m}$ for single mode fibers) by either mechanically tapering the fiber while heating, [59] or wet chemical etching. [60] This tip-like end of the fiber is usually coated with metals to effectively shield against optical leakage through the

fiber sidewalls. In the metal coated end of the fiber a small hole is opened by means of focused ion beam (FIB milling, etching, mechanical tapping or sputtering by local optical absorptive heating. Fig. 2.4 shows a sketch of a SNOM probe made of glass fiber with a metal coating and an aperture at its apex.

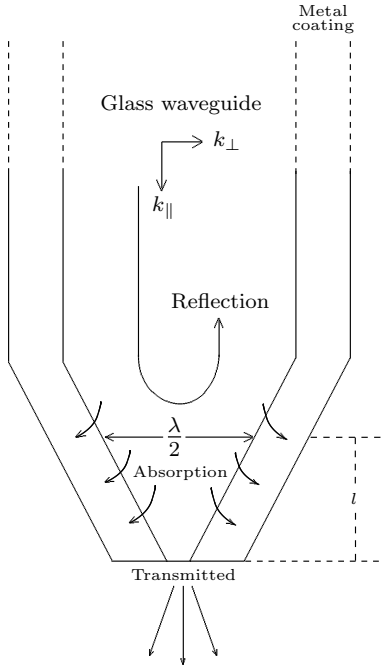

Figure 2.4: A sketch of an aperture probe (SNOM tip). The glass waveguide is sharpened and coated with metal. Most of the field incident on the aperture from the waveguide is reflected back due to wavelength and waveguide diameter dependent cut off. In the apex region below the cut-off diameter $\lambda/2$, the field possesses an imaginary wave vector, meaning an exponentially decaying field amplitude. The field amplitude at the aperture is attenuated by factor $e^{-k_\parallel l}$, where $k_\parallel$ is the parallel component of the wave vector and l is the distance between the aperture and the cut-off diameter $\lambda/2$. In addition, in this range the metal coating gives rise to significant field dissipation because of absorption.

Operation Modes

Today SNOM utilizes a mechanical feedback mechanism to regulate the separation between the aperture and the surface while the aperture is raster scanned on the surface of the sample. The early versions of SNOM were built such that the near field amplitude was used as a feedback signal. This type of feedback mechanism was soon found to generate severe artifacts in the near field images. The invention of shear force feedback mechanism utilizing piezoelectric quartz tuning-forks attached close to the aperture end

of optical fibers allowed an independent distance regulation scheme [61, 62]. The distance regulation is managed by monitoring the piezovoltage between the two arms of the tuning fork at the fork's eigenfrequency as a function of the aperture-surface distance. The near field images taken this way contain fewer artifacts than the previous designs. Although most of the commercial or lab grade SNOMs are today based on shear force, there also exists some commercial SNOMs which use cantilevered SNOM probes and optical motion sensors as in AFMs. [63]

There are different operation configurations: 1) Illuminating a sample with SNOM aperture and collecting the transmitted radiation through the sample as suggested in the original idea of Synge using an inverted optical microscope, 2) Collecting the back reflected signal from the sample by the aperture, 3) Collecting the reflected signal from the sample via external objectives at oblique incidence 4) Illuminating the sample from underneath with an inverted microscope and collecting the transmission by the SNOM aperture, 5) Illuminating the sample with an oblique incidence objective and collecting the scattered light with the SNOM aperture.

Lateral resolution, optical throughput

The lateral resolution of SNOM is basically given by the aperture diameter. The most common methods for manufacturing the aperture do allow for aperture diameters of 100 nm size. In some extreme cases the diameter may go down to 50 nm or less. Although the technical improvements in nano machining can indeed make still smaller aperture sizes, another basic limitation is set by the optical power throughput. The optical radiation in the fiber travels with a wave vector $k = k_{\parallel} + k_{\perp}$, where $k_{\parallel}$ is the component of the wave vector along the fiber axis and $k_{\perp}$ is the component of the wave vector perpendicular to the fiber axis. At the same time the wave vector magnitude is given by

$$k^2 = \mu\varepsilon\omega^2 = \frac{4\pi^2}{\lambda^2}.$$

where $\omega = 2\pi c/\lambda$ is the angular frequency and λ is the wavelength with μ and ε denoting the permeability and the dielectric constant of the medium, respectively. The propagation of the field in the optical fiber stops when

$$\begin{aligned} k_{\parallel} &= 0 \\ \Rightarrow k_{\perp} &= \frac{2\pi}{\lambda}. \end{aligned}$$

This condition is met when the diameter of the fiber determining $k_{\perp}$ equals $\lambda/2$ as shown at the axial position r_0 in the figure. At this position most of the incident power will reflect back into the optical fiber. In the range below r_0, where the diameter is smaller than $\lambda/2$, the parallel component of the wave vector is imaginary since perpendicular component will become

$$\begin{aligned} k_{\perp} > \frac{2\pi}{\lambda} \quad &\Rightarrow \quad k_{\parallel}^2 = \frac{4\pi^2}{\lambda^2} - k_{\perp}^2 < 0 \\ &\Rightarrow \quad k_{\parallel} = i|k_{\parallel}|. \end{aligned}$$

The optical field in this range shows an exponentially decreasing evanescent behavior like

$$E = E_0 e^{-|k_{\parallel}|(r-r_0)}$$

meaning that the field amplitude decreases exponentially towards the aperture. In addition to this geometrical cut-off resulting in an exponential decrease in the field amplitude, the metal coating around the fiber attenuates the field because of absorption. The input amplitude E_0 can not be increased to arbitrarily high values in order to increase the amplitude at the aperture $E_0 e^{-kl}$ since absorption may damage the metal coating due to excessive heat generation. The optical transmission coefficients in standard SNOM probes are reported to be around 10^{-6} to 10^{-5}. [60]

2.3.3 Near field-enhancing and localizing techniques (*a*-SNOM)

Interesting near field variations take place over smaller distances than $\lambda/2$, at about 5 nm to 10 nm range since they result from objects of similar scale dimensions. Recently interest was focused on exploring these effects as they are found to be at the origin of surprisingly high optical response on roughened metallic surfaces. In scattering experiments, these enhancement effects due to nanometrically corrugated conducting surfaces are utilized to enhance scattering cross sections to allow for detection of even single molecules. As an example, networks of few nanometer diameter metal clusters can show strongly confined and high intensity near field distributions at nm wide gaps between them. [64–72] The nature of these "gap modes" is still not fully understood. Precise fabrication of engineered gaps is not yet possible, but the stochastic nature of wide scale metallization processes like metal evaporation, sputtering or electro- or electroless-deposition of metals yield corrugated surfaces which are rich in such inter-particle gaps. These surfaces are used mostly in Raman scattering in order to increase the effective Raman scattering cross-section by 10 orders of magnitude and more. Such an enhancement factor allows Raman spectroscopy even on isolated single molecules [73–80].

Strong field intensities are not only restricted to the gap-modes. Metallic nanoscale particles were also found to generate strong near fields at specific wavelengths. The wavelength dependence of this effect implied some resonance phenomena to be at work. Soon these effects were pinned to plasmon resonance modes depending sensitively on the size, geometry, wavelength and metal element. Most interesting results were obtained with nano sized Ag and Au spheres. An immediate idea to implement such a resonant field enhancing metal particle could be to attach it to the end of an AFM tip, and scan this field enhancing nanoscatterer as a nanosource over the surface of interest [81]. One severe limitation was the strong dependence of the resonance effect on the above mentioned variables like size and geometry. Smallest disturbances in these had dramatic changes.

Perhaps the most attractive amongst various nanoscale scatterers is the sharp apex of an AFM tip itself. Metallized AFM tips have shown to generate strong near fields at their apex when illuminated. Fig. 2.5 shows SEM images of Au and Ag coated AFM cantilever tips produced for my own research. Typically, metal coatings of Si tips exhibit surface that show corrugations, as can be seen from Fig.2.5. The corrugated nature of the film coating is considered to influence the near fields generated at the tip apex in a somewhat stochastic manner. Theoretical studies predict a very strong near field

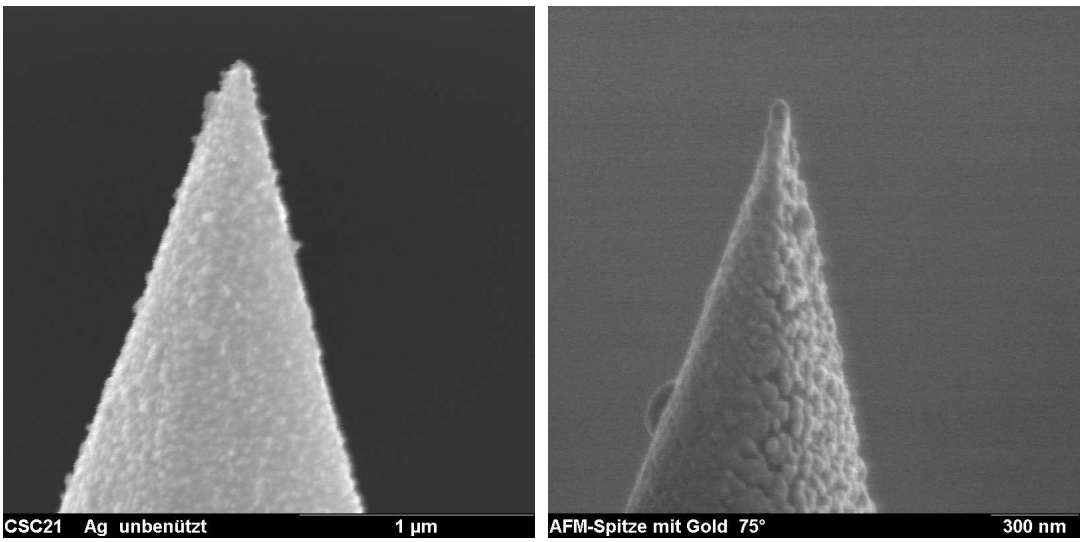

Figure 2.5: SEM images of two Si AFM tips. On the left a Au coated tip, and on the right a Ag coated tip. The metal coatings are 10 nm each. The metal films lack continuity around the Si tip.

enhancement at the tip apex also in non corrugated surfaces. Fig. 2.6 shows the near field distribution on the surface of a conical Au AFM tip ending in a 10 nm radius spherical cap. The field distribution shows a strong confinement and enhancement at the apex. This enhancement effect is analogous to the high gain antennas in radio waves. [82–85] The calculations show enhancement factors of about 1 to 2 orders of magnitude in field strength. These calculations are made by the research group members Dr. Ralf Vogelgesang and Ruben Esteban by using multiple multipole method (MMP).

Although the field enhancement factors for sharp tips are calculated to be typically one or two orders magnitude, it offers new possibilities in the near field optics instrumentation for nm resolution as it can be associated with the well established AFM

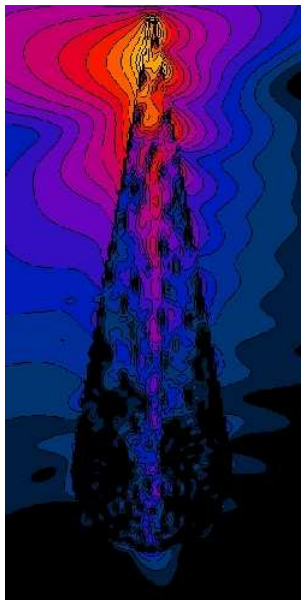

Figure 2.6: The near field amplitude on the surface of a 3μm long Au tip in case of 1μm Gaussian focus illumination centered at the apex, which has a spherical shape of 10 nm radius. The field distribution shows a strong confinement and enhancement at the apex.

technique. Fig. 2.7 illustrates an illuminated AFM tip in close proximity of a hypothetical surface with dispersed nanoparticles. When the scattered field amplitudes can be elevated to a high enough level locally at the AFM tip apex, and also a mechanism is found to suppress the parasitic background scattering amplitude effectively, then it can be used as a tool to image surfaces in their near fields at a spatial resolution approaching that of AFM.

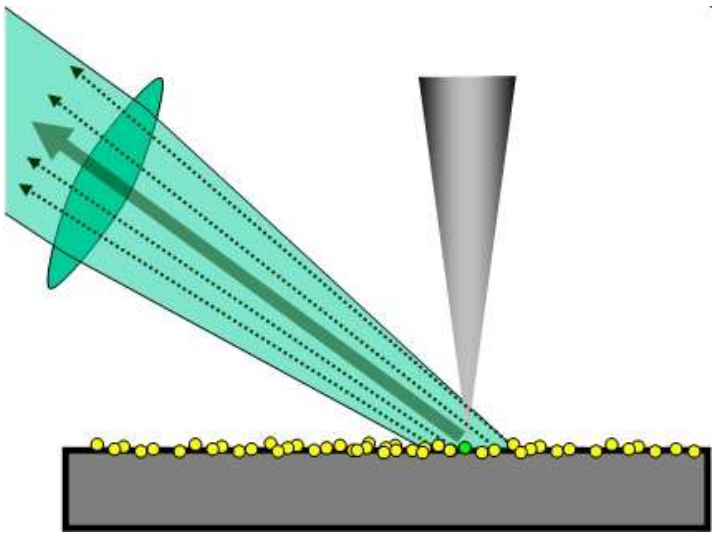

Figure 2.7: Using the tip as a local probe for the near field at the surface.

Two aspects of field enhancement are important in the context of achieving *observable* signal levels:

1. On the one hand the desired part of the radiation generated by a sample must be above the noise floor of the detection system,

2. on the other it must be bigger than the parasitic part.

Static near field enhancing optical microscopes

The first condition can, of course always be ensured, if single photon detectors such as photo multiplier tubes, avalanche diodes, or CCD cameras may be used. Single photon detection schemes are, however, necessarily accumulative and do not work well in conjunction with techniques like modulation plus lock-in amplification or interferometric optical amplification, which require an at least quasi-continuous signal. Furthermore, even these types of detectors do exhibit noise, due to the ubiquitous background high-energy cosmic radiation, which is virtually impossible to suppress. As a useful figure of merit, count rates of one per second are the minimum tolerable signal. Also in terms of experiment time, of course. Anything less would lead to forbiddingly long acquisition periods for full images. Considering the Raman scattering as an example, we find typical scattering cross section are in the range of 10^{-30} cm^2 per unit cell. Even for the exceptionally robust and strongly scattering carbon nano tubes (CNTs) the cross section reaches only about 10^{-26} cm^2 per atom, *i.e.*, a 1nm long piece exhibits a cross section of about 10^{-24} cm^2 for $\lambda_{laser} = 632$nm. A flux of several hundred kW/cm^2 is required to generate one Raman photon per second from this little material. While it poses no technical problem to focus light to such areal power densities, to avoid the destructive heating effects of large area illumination, localized field enhancement of *several* orders of magnitude must be employed, spatially confining the strong optical fields to a few nm. As of today, no methodical way has be demonstrated for achieving this. Only by chance (in approximately 10 percent of the cases or less) metallized AFM tips exhibit this kind of enhancement (private communication Satoshi Kawata, Achim Hartschuh,

Volker Deckert.) It is a bleak outlook to realize that even in the best of these cases another 4 orders of magnitude enhancement are required before the study material of more typical Raman cross sections (10^{-30} cm^2) becomes feasible. From this point of view, a more viable alternative are other light-matter interaction mechanisms such as luminescence or elastic scattering, whose cross sections reach 10^{-15} cm^2 and more.

Still, the second condition for observability has to be met for these types of interaction also. The discrimination of desired from parasitic background radiation by sheer static field enhancement is basically an evaluation of geometric ratios. Consider the diffraction limited collection optics to have an effective focus volume of diameter D and the sample volume of interest to have a diameter of Δs. If the latter is part of linear material (such as CNTs) the necessary enhancement factor must be

$$\Phi \gg \frac{D}{\Delta s} \; ;$$

for a two-dimensional sample system

$$\Phi \gg \left(\frac{D}{\Delta s} \right)^2 \; .$$

That is, even if one uses an ideal, diffraction limited confocal microscope for radiation collection (limiting oneself to transparent substrates observed from below) with a focus size of $D \approx 300\,\mathrm{nm}$, a $10\,\mathrm{nm}$ lateral resolution by static enhancement requires $\Phi \gg 1000$ in the two-dimensional case – a requirement difficult to realize, as discussed above. For opaque samples, observed from above with smaller NA collection optics, the analysis gets even worse.

In summary, these considerations on the required field enhancement factors, together with the empirical finding that it is currently not possible to reliably manufacture AFM or STM tips which exhibit these properties, and the restriction to transparent substrates, strongly point away from static enhancement schemes towards a dynamic mode optical near-field microscopes.

Dynamic near field enhancing optical microscopes

In the dynamic version of near field enhancing optical microscopes, the distance between the field enhancing AFM or STM tip and the sample surface is periodically altered and the modulation in the observed far field intensity observed with a lock-in amplification scheme. This is very simply implemented in the case of non-contact mode AFM, which already uses a vibrating tip for topography imaging. The modulated detection scheme allows to effectively eliminate all static contributions the far field, stemming mostly from the parasitic collection of optical signals from the whole illuminated sample area.

One must, however, keep in mind that not only the near field optical signal is modulated, but also – through basic reflection and shadowing effects – the remaining sample area in the collection focus. Thus, at the fundamental modulation frequency, there is still a significant contribution from parasitic non-local scattering effects to be expected. Here, an additional trick helps to also eliminate these parasitic signals, namely the fact that the near field optical interaction is highly non linear, whereas reflection and shadowing are linear effects. The former will generate signals also at the higher harmonics $2\Omega, 3\Omega, \ldots$ of the fundamental modulation frequency Ω; the latter will not. Therefore, observation at these higher harmonics allows one to obtain truly near field optical contrast. The instrument presented in this thesis is based on this principle.

Chapter 3

Theoretical considerations for *a*-SNOM

Considering the optical response of nm-sized material features, it becomes clear that nano-optical investigations may indeed serve as tests to the validity of the classical electrodynamic concepts usually employed. It is well-known, for example, that bulk dielectric constants of metals are not appropriate when geometrical restrictions smaller than the free electron path lead to increased scattering of free charge carriers, which in turn lead to changes of the dielectric function of the material objects. [86, 87] For the purpose of the present thesis an elementary classical electrodynamic description is developed.

Even in this framework, finding an analytical result is not possible, except for the simplest, most idealized geometric shapes, such as a plane or a sphere, and ideally uniform material properties. In general, numerical simulations of the interaction must be consulted.

The model I present in the first part of this chapter analyzes the simplified problem of a spherical homogeneous tip above a planar surface in the quasi-static approximation. It serves well to represent qualitative trends but certainly has its limitations for quantitative predictions.

I will discuss in the second part as an extension the topic of static resonances, which

helps to emphasize the consequences of the stochastic nature of tip fabrication and surface roughness at the nm scale.

3.1 Quasi-static dipole model of *a*-SNOM

3.1.1 Derivation of the dipole model

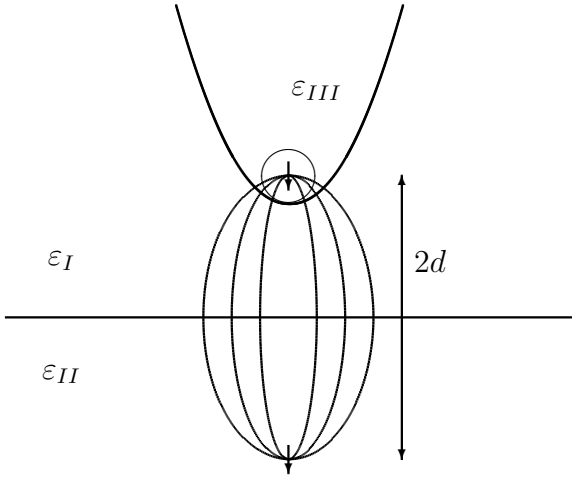

Figure 3.1: The quasi-static dipole model for the interaction of a dielectric AFM tip with a surface. The incident radiation excites a dipole in a sphere, which represents the tip. This in turn induces an image dipole in the material, which also interacts with the sphere. The combined system responds with an effective total polarizability.

In this section I derive expressions for the optical response of a dielectric sphere above a dielectric medium to the complexity level of the dipole-image dipole interaction. The action of an *a*-SNOM tip is rather well represented by a sphere [88] of the same material and with a radius equal to the effective apex radius, see also Fig. 3.1. After the Maxwell equations for dielectric media are reviewed, the method of image charges is introduced to solve boundary conditions for specific scenarios like point charges/multipoles above a dielectric medium and a sphere in a homogeneous electric field. Finally, the case of a small, dipole-polarizable sphere above a dielectric surface is studied.

Maxwell equations

The macroscopic Maxwell Equations in SI units are

$$\nabla\cdot\mathbf{D} = \rho \tag{3.1a}$$

$$\nabla\cdot\mathbf{B} = 0 \tag{3.1b}$$

$$\nabla\times\mathbf{E} = -\dot{\mathbf{B}} \tag{3.1c}$$

$$\nabla\times\mathbf{H} = \mathbf{J}+\dot{\mathbf{D}} \tag{3.1d}$$

where $\mathbf{D}$ is the polarization, ρ is the charge density, $\mathbf{B}$ is the magnetic induction, $\mathbf{E}$ is the electric field, $\mathbf{H}$ is the magnetic field and $\mathbf{J}$ is the current density. Together with the Lorentz equations for changes in energy and momentum density they form a complete description of the classical electrodynamic world. A necessary addition are the constitutive material equations. Among the possible choices the following three equations are the most commonly used

$$\mathbf{D} = \varepsilon\mathbf{E} \tag{3.2a}$$

$$\mathbf{H} = \mu^{-1}\mathbf{B} \tag{3.2b}$$

$$\mathbf{J} = \sigma\mathbf{E} \tag{3.2c}$$

Here ε is the dielectric constant, μ is the permeability, and σ is the conductivity of the material.

At mathematically ideal, smooth (no infinitely sharp vertices or wedges) interfaces Maxwell's equations imply so-called boundary conditions between the field in the two

neighboring dielectric media I and II

$$\mathbf{n} \cdot \left(\mathbf{D}^I - \mathbf{D}^{II}\right) = \hat{\rho} \tag{3.3a}$$

$$\mathbf{n} \cdot \left(\mathbf{B}^I - \mathbf{B}^{II}\right) = 0 \tag{3.3b}$$

$$\mathbf{n} \times \left(\mathbf{E}^I - \mathbf{E}^{II}\right) = 0 \tag{3.3c}$$

$$\mathbf{n} \times \left(\mathbf{H}^I - \mathbf{H}^{II}\right) = \hat{\mathbf{J}} \tag{3.3d}$$

where $\mathbf{n}$ is the normal vector at the surface element, $\hat{\rho}$ is the surface charge density, and $\hat{\mathbf{J}}$ is the surface current density. The superscripts I and II represent the fields in medium I and medium II respectively.

All the experiments described in this thesis were conducted using highly monochromatic laser light, justifying the use of the so-called time-harmonic approximation, in which all time-variable field quantities are assumed to exhibit oscillatory behavior like

$$\exp\left(-i\omega t\right)$$

where ω is the angular frequency of the laser light employed (typically in the range of 10^{15} Hz for visible light.) The material properties are functions of this frequency. In particular, the dielectric constant $\varepsilon(\omega)$ and the conductivity $\sigma(\omega)$ are conveniently merged into a single, complex-valued effective dielectric constant

$$\varepsilon^*(\omega) = \varepsilon(\omega) + \frac{i}{\omega}\sigma(\omega) \tag{3.4}$$

which gives the time-harmonic Maxwell equations the rather simple form

$$\nabla \cdot \left(\underline{\underline{\varepsilon}}^* \mathbf{E}\right) = 0 \tag{3.5a}$$

$$\nabla \cdot \mathbf{B} = 0 \tag{3.5b}$$

$$\nabla \times \mathbf{E} = +i\omega\mathbf{B} \tag{3.5c}$$

$$\nabla \times \left(\underline{\underline{\mu}}^{-1}\mathbf{B}\right) = -i\omega\underline{\underline{\varepsilon}}^*\mathbf{E} \tag{3.5d}$$

For many bulk materials the complex dielectric functions have been accurately measure and tabulated. It must be mentioned, however, that for particles of very small dimensions (*e.g.*, metal particles much smaller than the free electron path length,) the effective dielectric constant might differ from the bulk values. This very effect may, of course, be made subject to nano-optical investigations.

In the following I will employ the so-called *quasi-static approximation* to the complete Maxwell theory. This approximation uses static Maxwell Theory ($\omega \to 0$) but retains the material properties at the laser frequency ($\varepsilon^*(0) \to \varepsilon^*(\omega_L)$, *etc.*) It is considered applicable whenever the size of relevant objects is much smaller than the wavelength of propagating fields, as is the case in many nano-optical studies.

Image charges and response function of planar dielectric interfaces

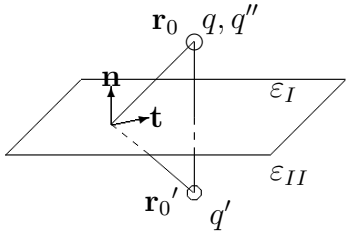

Figure 3.2: A charge located at $\mathbf{r}$ inside medium I induces a image charges in both media at its own location and its mirror location.

For a point charge located at $\mathbf{r}_0$ in a dielectric medium of dielectric constant ε_I, which is separated from another medium ε_{II} by an infinite plane with surface normal $\mathbf{n}$ (see Fig. 3.2), the solution to Maxwell's equations and boundary conditions is given by the well-known scalar *image charge* potentials

$$\begin{aligned} \Phi_I &= \frac{1}{4\pi\varepsilon_0}\frac{q}{|\mathbf{r}-\mathbf{r}_0|} + \frac{1}{4\pi\varepsilon_0}\frac{q'}{|\mathbf{r}-\mathbf{r}_0{}'|} \ , \\ \Phi_{II} &= \frac{1}{4\pi\varepsilon_0}\frac{q''}{|\mathbf{r}-\mathbf{r}_0|} \ . \end{aligned}$$

where the magnitudes of the image charges are

$$\begin{aligned} q' &= \beta' q \ , \\ q'' &= \beta'' q \ . \end{aligned}$$

The terms

$$\beta' = \frac{\varepsilon_{II} - \varepsilon_I}{\varepsilon_{II} + \varepsilon_I} \ , \tag{3.6a}$$

$$\beta'' = \frac{2\varepsilon_I}{\varepsilon_I + \varepsilon_{II}} \ . \tag{3.6b}$$

are called the *response functions* of the interface.

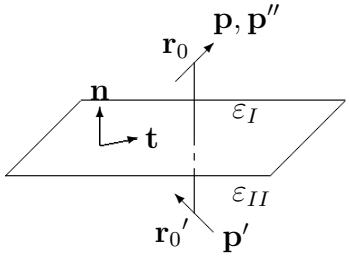

Figure 3.3: A point dipole located at $\mathbf{r}_0$ inside medium I induces image point dipoles in both media at its own location and its mirror location.

The analysis of single charges is easily extended to dipoles and higher order multipoles. Following the idea of Fig. 3.2, a point dipole can be described as the limiting object derived from two equal charges of opposite signs, separated by a distance $\mathbf{d}$, centered at $\mathbf{r}_0$. This corresponds to making the distance infinitesimally small and simultaneously the charge magnitude infinite, such that the value of the dipole

$$\mathbf{p} = q\mathbf{d}$$

is constant. Due to the additive nature of electric fields, the values of the image charges are individually determined using the same response functions Eq. (3.6) that hold for a single charge. The direction vector $\mathbf{d}'$ between the two image charges in medium II is

given by $\mathbf{d}' = \mathbf{d} - 2\mathbf{n}(\mathbf{n}\cdot\mathbf{d})$, thus

$$\mathbf{p}' = q'\mathbf{d}' = \beta'\left(\mathbf{p} - 2\mathbf{n}(\mathbf{n}\cdot\mathbf{p})\right) , \tag{3.7}$$

$$\mathbf{p}'' = q''\mathbf{d}'' = \beta''\mathbf{p} . \tag{3.8}$$

Finally, I mention that the response of a dielectric interface to an incident homogeneous field $\mathbf{E}_{inc}$ (which may be thought of as created by two equally distant equal charges of opposite sign) is given by

$$\mathbf{E}' = \beta'\left(2\mathbf{n}(\mathbf{n}\cdot\mathbf{E}_{inc}) - \mathbf{E}_{inc}\right) , \tag{3.9}$$

$$\mathbf{E}'' = \beta''\mathbf{E}_{inc} . \tag{3.10}$$

Dielectric sphere in homogeneous background field

The field generated by dielectric sphere (of radius R and dielectric constant ε_{III}) embedded in medium ε_I and subject to an external homogenous electric field $\mathbf{E}$ (See Fig. 3.4.) can be described by an internal homogeneous field

$$\mathbf{E}' = \frac{3\varepsilon_I}{\varepsilon_{III} + 2\varepsilon_I}\mathbf{E}$$

and an external field of an electric dipole $\mathbf{p}$ located at the center of the sphere

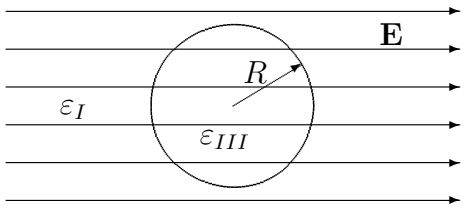

Figure 3.4: A dielectric sphere (of radius R and dielectric constant ε_{III}) embedded in medium ε_I and subject to an external homogenous electric field $\mathbf{E}$.

$$\mathbf{p} = 4\pi R^3\varepsilon_0\frac{\varepsilon_{III} - \varepsilon_I}{\varepsilon_{III} + 2\varepsilon_I}\mathbf{E} . \tag{3.11}$$

In analogy with Eq. (3.6)

$$\hat{\beta}' = \frac{\varepsilon_{III} - \varepsilon_I}{\varepsilon_{III} + 2\varepsilon_I} , \tag{3.12a}$$

$$\hat{\beta}'' = \frac{3\varepsilon_I}{\varepsilon_{III} + 2\varepsilon_I} \tag{3.12b}$$

might be called the response functions of the dielectric sphere. As I will discuss in Sec. 3.2, however, it is more suitable to discuss the resonant behavior of small dielectric bodies in the broader context of static resonances. At this point I only introduce

$$\alpha = 4\pi R^3 \varepsilon_0 \frac{\varepsilon_{III} - \varepsilon_I}{\varepsilon_{III} + 2\varepsilon_I} \tag{3.13}$$

as the *polarizability* of the sphere.

Small dielectric sphere above a dielectric interface

Consider a very small dielectric sphere above an interface between two dielectric media. The dielectric medium containing the sphere is characterized by ε_I, the other by ε_{II}. The distance from the center of the sphere to the surface shall be d. (See Fig. 3.5.)

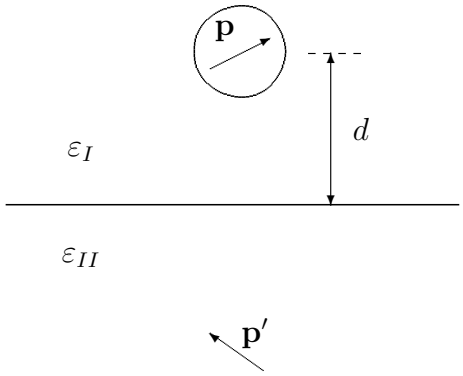

Figure 3.5: A small dielectric sphere in medium ε_I, located at a d above an interface between another dielectric media with ε_{II}.

The radius of the sphere is small in the sense that the electric field $\mathbf{E}$ in medium I at its location is nearly constant, *i.e.*, the quasi-static approximation may be applied. Let the field be represented by its value at its center, which is the sum of an "exciting" external field $\mathbf{E}_{inc}$ and response fields created by the dielectric media as $\mathbf{E} = \mathbf{E}_{inc} +$

$\mathbf{E}_{sphere} + \mathbf{E}_{interface}$.

The response of the interface is easily written down with the use Eq. (3.9) as

$$\mathbf{E}_{interface} = \beta' \left(2\mathbf{n}(\mathbf{n}\cdot\mathbf{E}_{inc}) - \mathbf{E}_{inc}\right)$$

According to Eq. (3.11), the response of the dielectric sphere to the total constant external electric field $\mathbf{E}$ is that of an effective dipole $\mathbf{p}$ acting upon medium I

$$\mathbf{p} = \alpha\mathbf{E}$$

which in turn induces an image dipole $\mathbf{p}'$ according to Eq. (3.7)

$$\mathbf{p}' = \beta' \left(2\mathbf{n}(\mathbf{n}\cdot\mathbf{p}) - \mathbf{p}\right)$$

The electric field contribution of this image dipole to the total field in medium I at the location of the sphere is

$$\mathbf{E}_{sphere} = \frac{1}{4\pi\varepsilon_0}\frac{3(\mathbf{p}'\cdot\mathbf{n})\mathbf{n} - \mathbf{p}'}{(2d)^3} = \frac{\beta'}{4\pi\varepsilon_0}\frac{(\mathbf{p}\cdot\mathbf{n})\mathbf{n} + \mathbf{p}}{(2d)^3}$$

Thus the equation for the dipole induced in the sphere can be obtained as

$$\frac{1}{\alpha}\mathbf{p} = \mathbf{E}_{inc} + \frac{\beta'}{4\pi\varepsilon_0}\frac{(\mathbf{p}\cdot\mathbf{n})\mathbf{n} + \mathbf{p}}{(2d)^3} + \beta' \left(2\mathbf{n}(\mathbf{n}\cdot\mathbf{E}_{inc}) - \mathbf{E}_{inc}\right)$$

which can not easily be expressed in closed form due to the different responses to polarization perpendicular ($\mathbf{p}\cdot\mathbf{n} = |\mathbf{p}|$, $\mathbf{E}_{inc}\cdot\mathbf{n} = |\mathbf{E}_{inc}|$) and parallel ($\mathbf{E}_{inc}\cdot\mathbf{n} = \mathbf{p}\cdot\mathbf{n} = 0$) to the surface. Therefore I adopt the case-by-case notation

$$\begin{Bmatrix} \mathbf{p}_\perp \\ \mathbf{p}_\parallel \end{Bmatrix} = \frac{\alpha(1 \pm \beta')}{1 - \frac{3\pm1}{2}\frac{\alpha\beta'}{32\pi\varepsilon_I d^3}} \begin{Bmatrix} \mathbf{E}_{inc\perp} \\ \mathbf{E}_{inc\parallel} \end{Bmatrix}$$

This dipole and its image dipole Eq. (3.7)

$$\begin{Bmatrix} \mathbf{p}'_\perp \\ \mathbf{p}'_\parallel \end{Bmatrix} = \begin{Bmatrix} +\beta' \mathbf{p}_\perp \\ -\beta' \mathbf{p}_\parallel \end{Bmatrix}$$

are both acting on medium I. The total "scattered" field generated by the incident field in medium I is thus given by the sum of the two dipole fields, which for large distances may be described by a single effective induced dipole, whose effective polarizability is the sum of the two individual polarizabilities.

$$\begin{Bmatrix} \alpha_\perp^{eff} \\ \alpha_\parallel^{eff} \end{Bmatrix} = \frac{\alpha \left(1 \pm \beta'\right)^2}{1 - \frac{3 \pm 1}{2} \frac{\alpha \beta'}{32 \pi \varepsilon_I d^3}} \tag{3.14}$$

This kind of model has been used to analyze the scattering from an extended tip over different surfaces. [89] It should be noted that the model used in the cited work did not take into account the reflected field from the interface in the square of the $(1 \pm \beta')$ term in Eq. 3.14. In that respect the model given here is one step closer to represent the real situation. The central assumption at this point is that this effective polarization of the tip-surface system is directly proportional to the measurable far field intensity. Using this assumption, a number of consequences can be drawn, which are at least qualitatively verified by experiment. In the following I will discuss how the localized enhanced *near fields* are detected only for tip-sample distances of a few nm – which serves as a basis for experimental verification of purely near field optical contrast – and how the detected far field signals allow to distinguish different materials, that is the material contrast mechanism central to *a*-SNOM.

3.1.2 Complex optical approach curves and material response

Approach curves

Using Eq. 3.14, it is possible to estimate numerically many aspects of the near field optical effects of tip-sample interaction under the assumption that the far field detected power is radiated by the dipole that is induced by the effective polarizability of the tip-sample system $\alpha_{\perp}^{eff}$. In this section I calculate the complex-valued approach curves for

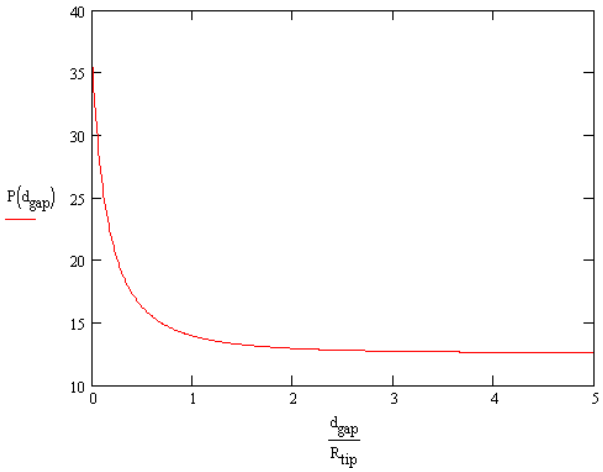

Figure 3.6: Typical static approach curve calculated using Eq. 3.14. Shown is the field strength (in arbitrary units) of the dipole radiation induced in the tip-sample system for varying gap distances (in units of the sphere radius). The calculation is made for an excitation wavelength of $\lambda = 633\,\mathrm{nm}$; the sample and tip are taken as made of Au, with a tip sphere radius assumed as $R = 10\,\mathrm{nm}$.

the example of a Au sphere on Au surface ($\varepsilon_{Au} = -10.5 + i1.35$). As Fig. 3.6 shows, the near field optical power is nearly constant for large tip-sample distances, but increases dramatically as the probe approaches to distances less than approximately the effective tip apex radius.

This curve is the basis to simulate the registered signal in the case of a dynamic mode AFM operation in which the tip vibrates vertically above the sample surface, sweeping a portion (equal to the vibration amplitude) of this static approach curve periodically. The scattered field amplitude in dynamic AFM mode can be monitored at the tip frequency as well as at its higher harmonics, thus simulating the action of a lock-in amplifier operating at the corresponding reference frequencies.

By taking a vibration amplitude of about the tip radius, I calculated the dynamic

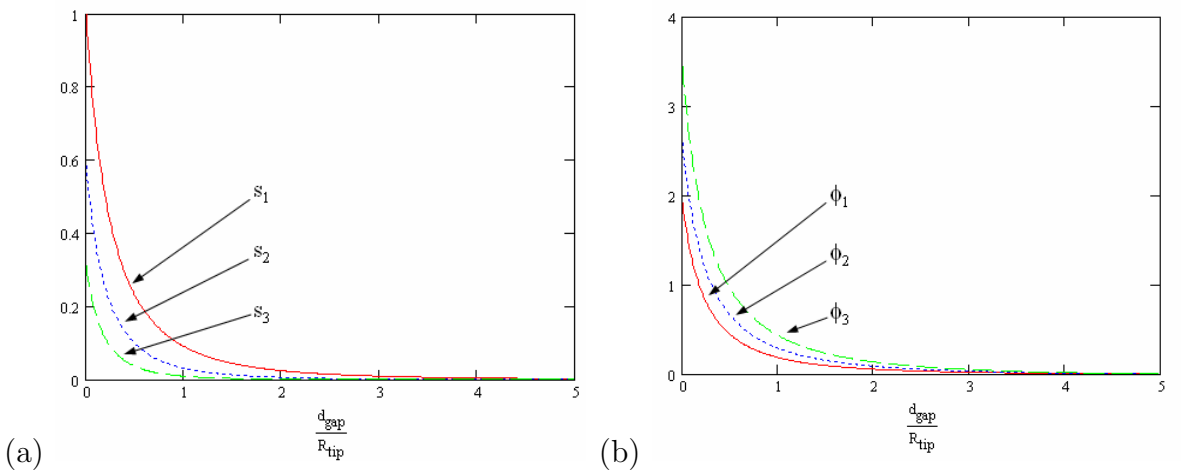

Figure 3.7: (a) dynamic approach curves for the optical amplitude (normalized to the s_1 value at zero distance) calculated at 1Ω, 2Ω, and 3Ω demodulations where Ω is the tip vibration frequency. (b) dynamic approach curves of the optical phase (in degrees) for the same demodulation orders as in (a). The phase at infinite distance is set to zero. For both parts, a vibration amplitude of 20 nm is taken and the static approach curve shown in Fig. 3.6 is used.

approach curves at the first three harmonics of the tip vibration frequency. The scattered optical field amplitude at the tip frequency is denoted by s_1, at twice the tip frequency as s_2 and so on. The same notation is also used in the scattered optical phase as φ_n ($n = 1, 2, 3, 4, ...$). Fig. 3.7 shows plots of dynamic approach curves for optical amplitude and phase calculated by using the static approach curve as in Fig. 3.6.

Several things can be noted from these curves: Clearly, both amplitude and phase show significant contrast, when the tip approaches to less than its effective apex radius. This holds generally for the relevant range of apex radius values, i.e., $R = 1 \ldots 100\,\mathrm{nm}$. While the contrast magnitude of the amplitude decreases for increasing demodulation order, it increases for the phase contrast. It should be noted, however, that the phase contrast, which is related with phase shifts in the scattering event due to absorption, is usually very weak, especially, when tip and/or sample materials are involved which do not exhibit large imaginary contributions to the dielectric constant. Furthermore, for very small apex radii ($R \to 0$) the predicted near field amplitudes diverge, while the far field can not, of course, due to energy conservation reasons (see also Sec. 3.1.3.)

Material contrast

Using the quasi-static dipole model, one can also study the dependence of the optical amplitude and phase on different sample materials in the dynamic mode operation. Modelling a 10nm radius Au sphere as a representative of a gold coated AFM tip apex, Fig. 3.8 shows in the dynamic AFM operation mode the third harmonic optical amplitude s_3 dependence on the surface material. The displayed curves show the s_3 dependence on the real part of the dielectric constant ε for different imaginary parts, equal to 10, 5, 1, and 0.5. The corresponding s_3 values for glass, Au, Si, and PtIr are shown by dots in the plot. Between the materials shown in Fig. 3.8, Au and glass

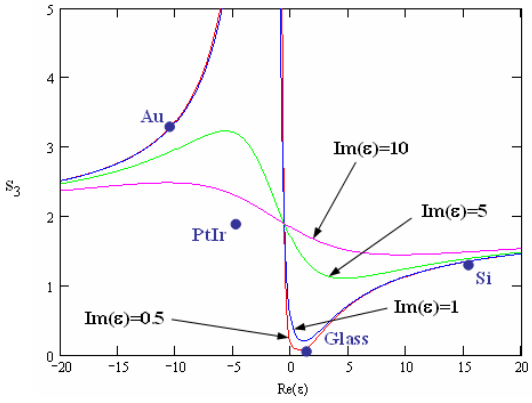

Figure 3.8: The third harmonic optical amplitude signal strength s_3 as a function the real part of the dielectric constant for a number of values for the imaginary part. The values for the materials glass, Si, Ag, Au, and PtIr for $\lambda = 632.8$nm excitation are also indicated. The AFM tip is represented as a 10 nm radius Au sphere.

are expected to show the highest material contrast at the chosen wavelength of 633nm using a gold tip. When a surface containing both glass and Au material is to be imaged in s_3 with a Au tip, it is expected to observe a sharp optical contrast between them. A Si-glass surface system on the other hand is expected to generate only 1/3 of the expected contrast from a Au-glass surface system. In Fig. 5.7 the optical contrast from the material is displayed and in Sec. 6.4 a discussion of material contrast is provided.

3.1.3 Discussion of the quasi-static dipole model

The quasi-static dipole model for the interaction of an illuminated AFM tip with a dielectric interface certainly has its merits. Besides the obvious fact that is analytically tractable, whereas a full analysis of the dynamic situation is only doable numerically, it captures the main qualitative trends, such as the resonance effects due to changing material properties, which predicts material contrast in the dielectric constant and allows to maximize the local near fields by tuning the exciting laser wavelength. The model also predicts a strong non-linear increase in the fields as the sphere-substrate distance is reduced – which is the basis of my experimental technique.

One severe defect of this approach is of course that far fields can not grow to infinite amplitudes, whereas the dipole polarizability may do so for resonant materials. While the near fields may indeed become infinite (over infinitesimal volumes), the radiated far field energy must be finite by energy conservation, which points to deviations in the observable far field intensities from the local near fields under observation.

The quasi-static dipole model although qualitatively predicts the experimentally observed results, the model is a reduction of the real situation in a convenient manner to provide fast analytical calculations as a guide to the experimentalist. The model neglects retardation effects which could be in depth taken into account by applying full Mie scattering theory. The reduction of the sharp tip geometry to a simple sphere is also employed in the model that clearly needs to consider extended tips shape for a more truthful representation of the actual situation. The dipole model also has limitations specifically for very short sphere interface separations. At this range true charge distribution over the sphere and interface has to be taken into account or higher order multipole schemes have to be applied.

Another important aspect is the effect of the tip material that has been neglected in the spherical approximation. As it turns out, the stem of the tip enhances the polarizability along its direction by an appropriate factor. [88] As a consequence, the

approximated spherical tip should be described by an anisotropic polarizability tensor

$$\underline{\underline{\alpha}} = 4\pi R^3 \varepsilon_0 \frac{\varepsilon_{III} - \varepsilon_I}{\varepsilon_{III} + 2\varepsilon_I} \begin{pmatrix} 1 & 0 & 0 \\ 0 & 1 & 0 \\ 0 & 0 & f \end{pmatrix}$$

instead of Eq. 3.13. Here f is a complex valued extra enhancement factor for the polarization along the tip's axis, which depends on the tip material and shape and the illumination used.

In particular the dependence of the local near fields at the tip apex on the shape of the tip may have drastic consequences, as I will show in the next section. Whereas the highly symmetric spherical tip predicts only one resonant optical frequency (where $\varepsilon(\omega) = -2$), a less symmetrical shape can become resonant for a number of frequencies, thus improving the chances for strong near field enhancement, even if the spherical resonance condition is not fulfilled.

3.2 Quasi-static shape resonances for huge near field enhancement

As was discussed in Sec. 3.1, the most promising way to ultimate optical resolution is the utilization of strongly enhanced, highly localized near fields. In general, such fields are generated at the vicinity of small, metallic clusters or at gaps between such clusters. As was demonstrated in the previous section, the enhancement factor near objects of basic geometrical shapes such as spheres or ellipsoids can be calculated analytically. In this section, I will outline the more general quasi-static theory of near fields of arbitrarily shaped objects. This leads to two important conclusions: firstly, even for simple objects, there are in general many dielectric resonances, not just one ($\varepsilon = -2$), as in the case of the highly symmetric sphere. Secondly, such resonances occur only for negative dielectric constants, as are found in many metals, which calls for the use of *metallized* AFM tips

in *a*-SNOM. Especially in view of the first statement, there is a fair chance of producing highly enhancing tips in this way because metallic coatings applied to AFM tips usually do not exhibit perfectly smooth texture (see also Fig. 2.5.)

Consider a closed domain of dielectric constant ε_{II} and arbitrary but "well-behaved" shape (most importantly, the shape shall not contain any wedges or vertices. [90, 91].) When this domain is enclosed in a medium of dielectric constant ε_I the normal boundary condition Eq. (3.3a) for the electric field on the surface of this domain reads[1]

$$\varepsilon_I \mathbf{E}_I \cdot \mathbf{n} \;=\; \varepsilon_{II} \mathbf{E}_{II} \cdot \mathbf{n}$$

where $\mathbf{n}$ is the surface normal and $\mathbf{E}$ is the local electric field, which in the static case may be derived from a potential [93]

$$\Phi(\mathbf{r}) \;=\; \frac{1}{4\pi\varepsilon_0} \int\limits_S \frac{\hat{\rho}(\mathbf{r}')}{|\mathbf{r}-\mathbf{r}'|} dS'$$

created by a single layer of surface charge density $\hat{\rho}$ on the surface S. The electric field $\mathbf{E}$ is the negative of the gradient of the potential,

$$\mathbf{E} \;=\; -\nabla\Phi$$

The potential is continuous everywhere, but the normal component of the first derivative of the single-layer potential suffers a jump equal to $\hat{\rho}/\varepsilon_0$. When inserted into the boundary equation, this yields the following integral eigenvalue equation:

$$\begin{aligned} \hat{\rho}(\mathbf{r}_0) &= \ell \frac{1}{2\pi} \int\limits_S \hat{\rho}(\mathbf{r}') \frac{(\mathbf{r}_0 - \mathbf{r}') \cdot \mathbf{n}}{|\mathbf{r}_0 - \mathbf{r}'|^3} dS' \\ \ell &= \frac{\varepsilon_{II} - \varepsilon_I}{\varepsilon_{II} + \varepsilon_I} \end{aligned}$$

It can be shown that the eigenvalue spectrum is discrete and real. $\ell = 1$ is an eigenvalue;

[1] The discussion of quasi-static resonance follows largely that of reference. [92]

it corresponds to the static distribution of surface charges on a charged domain II. All other eigenvalues fulfill

$$|\ell| > 1$$

and correspond to source-free or *resonance* modes. Notice that these modes are completely independent of the scale of the object volume. Only the shape matters, as long as the overall size remains considerably smaller than the free space wavelength, *i.e.*the quasi-static approximation is valid. The electric fields associated with these modes obey an orthogonality relation (i, k are the mode indices)

$$\int_{V_I} \mathbf{E}_i \cdot \mathbf{E}_k dV = \int_{V_{II}} \mathbf{E}_i \cdot \mathbf{E}_k dV \quad = \quad 0 \quad \text{if} \quad i \neq k$$

which is useful to analyze the coupling of incident radiation to a particular mode. A general ellipsoid, for instance, has three resonance modes for which the electric field is uniform inside domain II. As can be shown, these modes occur for dielectric constants fulfilling ($i = 1, 2, 3$)

$$\varepsilon^{*(i)}_{II} + \frac{1 - N_i}{N_i} \varepsilon^*{}_I \quad = \quad 0$$

where $N_1 + N_2 + N_3 = 1$. Notice how the sphere – being the special ellipsoid $N_1 = N_2 = N_3 = 1/3$ – is resonant for

$$\varepsilon^{*(i)}_{II} + 2\varepsilon^*{}_I \quad = \quad 0$$

which is exactly the resonant denominator of the response-function of a sphere Eq. (3.12a). Viewed in the present context, this response function simply expresses a triply degenerate resonance mode. As the ellipsoid resonance modes are exactly uniform inside domain II, the orthogonality relation means that *only* these uniform modes can be strongly excited by uniform (inside domain II) radiation.

For a more general case – *i.e.*, for a particle of complex geometry – any mode may

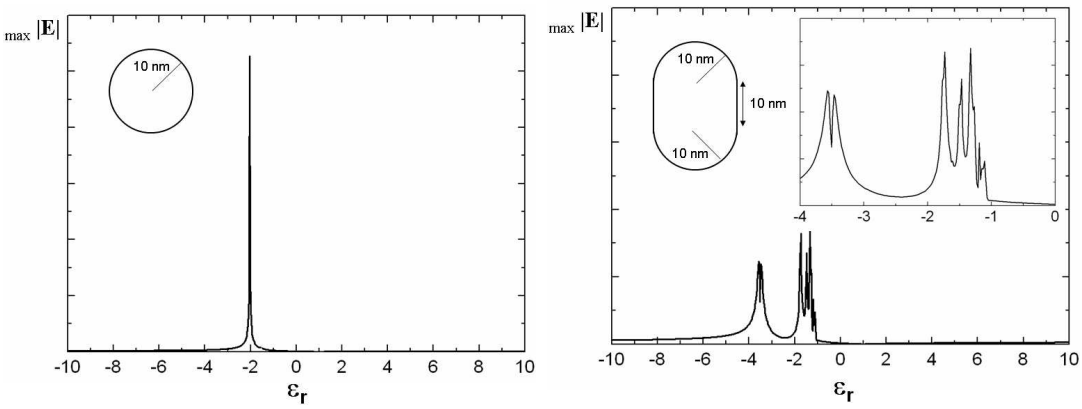

Figure 3.9: Shape resonances in a sphere (on the left) and a pill (on the right) as calculated at the MPI-FKF with the multiple multipole method. The maximum field modulus outside the object is plotted as a function the object's dielectric constant. The imaginary part of the dielectric constant is assumed zero (no damping). Excitation is simulated as linearly polarized 514nm radiation.

be excited which shows a significant average value of electric field components. To demonstrate the consequences of this result, Fig. (3.9) shows calculated field enhancements near a 10nm sphere and a pill-like shape of similar but different geometry (*i.e.*, a cylinder of length 10nm, capped by two semi-spheres of 10nm radius.) Plotted is the strongest field outside the object as a function of the object material dielectric constant ${\varepsilon^*}_{II}$. The solution was obtained with the multiple multipole technique – a fully three dimensional Maxwell solver. Excitation by linearly polarized laser radiation of 514nm wavelength was simulated.

As can be seen in Fig. (3.9), for a sphere exactly one resonance is found, precisely at ${\varepsilon^*}_I = -2$, as predicted. All other resonance modes can not be excited by this nearly perfectly uniform excitation radiation. For the pill-like particle, however, there are quite a number of resonances – corresponding to those eigenmodes of the object that exhibit appreciable average field values. It should be noted that this shape is rather close to being spherical; yet, its spectrum is vastly different!

To predict at what excitation frequencies (or free space wavelengths) these resonances can be observed, one has to consult the tabulated dielectric function of the object's material and located the frequency, at which it coincides with the resonance value. It is particularly noteworthy that for general particle this value is not simply (-2), as

would be suggested by a sphere-approximation; even relatively sphere-like shapes give rise to resonances elsewhere. A general conclusion can be drawn, nevertheless, from the requirement $|\ell| > 1$. As this can only be fulfilled for negative dielectric constants

$$Re(\varepsilon^*) < 0 \ ,$$

such resonances are expected predominantly for small metal particles or highly doped semiconductors, whose Drude-like behavior ensure negative dielectric constants at appropriate frequency regions.

Finally, I comment on the phenomenon of SERS, which occurs at rough metal surfaces. It has been found recently that the so-called "hot-spots" [65, 94, 95] at which Raman scattering of adsorbed molecules can be enhanced by several orders of magnitude by and large are located in the gap between two particles or surface protrusions. A possible interpretation in the context of shape resonances presents itself naturally. One of the two particles might couple efficiently to incident radiation, which necessarily is nearly uniform. The mode that is excited in this manner, however, may be strongly *non-uniform* in its near field. Thus, it may be able to excite modes in the nearby other particle that would be silent otherwise. The secondary modes in turn may lead to excitation of additional modes in the first particle, and so forth.

At least qualitatively it becomes clear in this manner how non-spherically shaped particles may excite each other resonantly, when placed in close proximity of each other. Also it becomes clear that this process is extremely fickle, as it depends very sensitively on the exact shape and relative location/orientation of the particles involved, which dampens any hopes of predicting or even manufacturing such hot-spots in a well-controlled fashion.

Chapter 4

Implementation of a tip-enhanced near field microscope for optical amplitude and phase-contrast

In this chapter I present the experimental details of the *a*-SNOM instrument which relies on elastic scattering for optical information retrieval at the nm scale. As mentioned in Ch. 1, my design builds upon a similar instrument as a starting point. [31] I introduced several modifications and improvements which are of essential importance for operation reliability and flexibility as well as enabling future experiments that are not possible with the instrument described in [31]. These modifications and distinctions are made keeping in mind the key factors of ensuring optimal optical alignment, reducing sources of possible mechanical artifacts and providing integrability to further other optical characterization methods. Before the detailed description of the instrument itself, I introduce and motivate the most important differences.

The ability of *both* the AFM tip and the sample to scan the light-matter interaction volume turned out to be extremely valuable. The previous design with a home made AFM lacks the tip-scan option and must manipulate the focusing optics to optimize alignment with the tip apex. With the setup presented here, recording x-y cuts of the optical illumination by tip-scan at successive z positions allows for mapping the 3

dimensional focal volume (Sec. 5.1.2). Having this 3 dimensional field map at hand one can accurately place the tip apex at the optical focus with nm precision. Indeed, it is straightforward in the present setup to decouple the incident radiation from the collection optics to excite independent near fields at arbitrary sample structures, which can be mapped out with the otherwise unchanged instrument. Moreover one can use two different acquisition schemes; one with fixed sample, and one with fixed tip–depending on the desired information from the surface and experimental circumstances. The details regarding multiple scan environment can be found in Secs. 4.1, 5.1.2 and 5.2.2.

There is also an important difference regarding the generation of the reference signal for lock-in detection between the two setups. In the current instrument, the reference signal is obtained directly from the detected tip vibration signal which is generated as a result of the real mechanical motion of the AFM cantilever (Sec. 4.8). This approach is superior to the synthetic reference signal synchronization scheme used in the other reported setup for the purpose of recording optical information. The mechanical phase of the tip oscillation is automatically excluded and needs not be recorded separately and subsequently subtracted. The *a*-SNOM presented here also has improvements and differences in the following parts of the setup as compared to the original design:

It is a plug and play instrument for a wide range of laser sources (limited in wavelength only by the optical elements used) thanks to the fiber optic laser delivery unit adding further flexibility to the setup (Sec. 4.2.1). It has a built-in delay line in the reference beam for setting the path difference to zero for optimum interference contrast (Sec. 4.2.2). The signal and reference beam lines are well separated on a larger INVAR base plate. This allows mounting of further optical elements like polarization control or spatial filters for confocal operation, etc. A trade-off is met in the complication of maintaining low noise and stability. A live camera looking at the tip region helps for initial naked eye characterization of cantilevers, optical alignment, sample surfaces, etc. (Fig. 4.5) The optical detector is an avalanche photodiode, not a p-i-n diode, but they can be regarded as equivalent, since the APD is used in the linear response regime. The

acousto-optical modulator is used with a parallelized beam for optimal generation of the frequency shifted beam in contrast to the focused alignment option (Fig. 4.6). Finally, the reference and signal beams are divided *before* the wavelength upshift takes place for retaining the pure line shape of the laser radiation and thus avoiding the inter-beam crosstalk of the shifted and unshifted frequencies resulting from the use of the AOM.

Basics of *a*-SNOM

In this technique the sample area under investigation is illuminated using diffractive far-field optics. The sharp apex of an AFM is brought to the center of the illuminated area using non-contact AFM feedback. The sample is then raster scanned under the AFM tip while the scattered light is collected using the same optics as used for illumination. Since the AFM apex stays as close as a few Angstroms to the surface, it interacts with the near field of the surface as well as the far field. The scattered light contains information including both parts. The near field information is discriminated from the overall scattered light by means of interferometric amplification of the entire signal and demodulation of this signal at the AFM cantilever frequency and its higher harmonics to suppress the far field components. The extracted near field signal shows lateral variations at the order of nanometers like an AFM images the topography. The resolution achievable by this method is limited mainly by the AFM tip apex radius which can be as sharp as 5 nm or better. Because an *interferometric* detection scheme is used, the full complex optical information can be obtained, i.e., not only the intensity of the near field but also its *optical phase*.

In apertureless scanning near-field optical microscope (*a*-SNOM) design, there are two essential independent experimental work horses that are joined together in a sophisticated lock-in detection technique. These are the atomic force microscope and the optical interferometer. Since the detection technique required dedicated and not so straightforward electronics, it is described in a separate section.

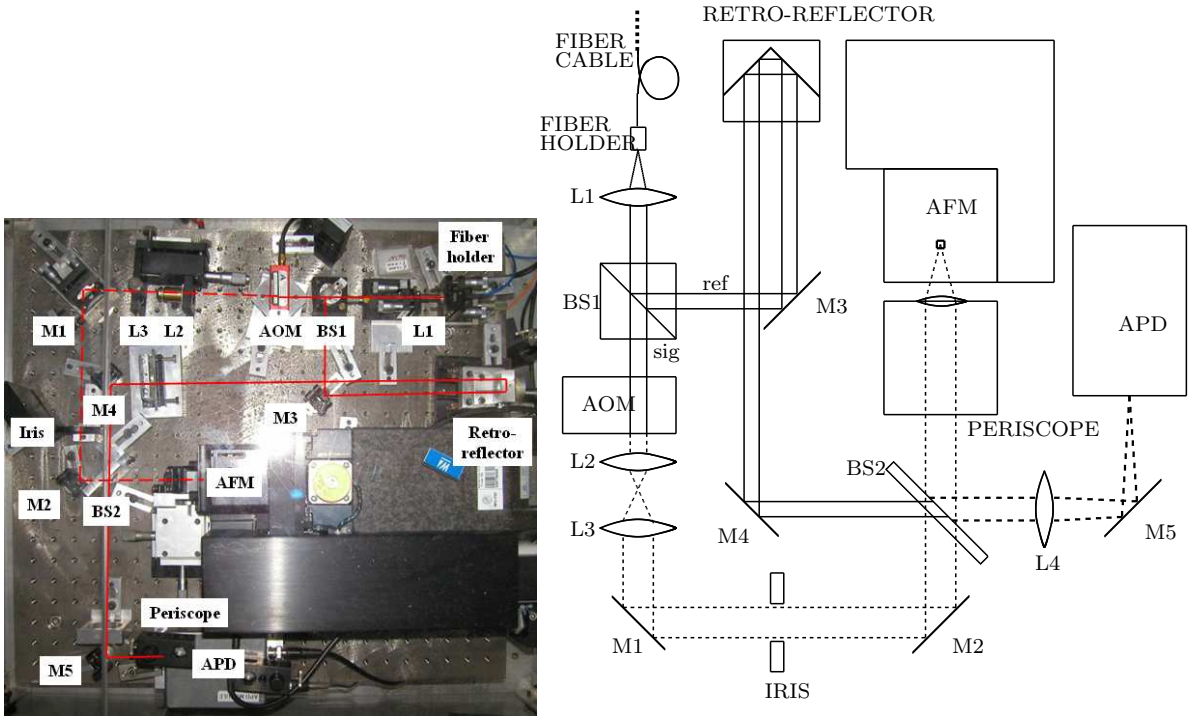

Figure 4.1: Overview photo and sketch of the setup. Around the commercial AFM, all free space optical elements are setup on a single "INVAR 36" base module. Light sources are delivered by "plug and play" glass fibers, allowing for an easy change of excitation wavelength. BS1 splits the beam into reference and signal beam. the signal beam is frequency shifted by an AOM and focused on the AFM tip apex by a periscope. Back scattered light from the tip-sample system is joined with the reference arm at BS2, and the interferometric signal is detected by an APD.

4.1 Mechanical setup

4.1.1 Atomic force microscope (AFM)

The AFM is a commercial amplitude modulation instrument that is operated in the dynamic (non-contact) mode throughout the studies presented here. It is a model M5, Park Scientific Instruments AFM with a 100μm scanner head. It has a travel range of $\sim$ 120μm in both the x and y scan axes and a 9μm travel range along z-axis. The instrument scan-head is installed on a coarse approach stepper-motor actuated z translation stage. The z translation stage is attached to a massive ($\sim$40 kg) granite base through a rectangular cross-section pillar that is made of the same granite material. The AFM is equipped with an imaging camera unit that is capable of doing software remote controlled zooming and focusing. Imaging lens system allows for manual positioning to

the area of interest through two adjustment screws. The AFM unit also has a fiber-optical illumination system accompanying the imaging system which is also remote controllable through the software. A 670nm diode laser is focused and positioned on the reflective side of an AFM cantilever. The laser can be positioned on the cantilever using a slide bar while monitoring the position on the video screen. The reflected beam from the top surface of the cantilever is then positioned on a quadrant diode for beam deflection detection. The fine adjustment of the reflected beam on the quadrant photodiode is done by steering two tilt angles on a miniature mirror stage. This mirror is used to divert the beam towards the photodiode and to center it on the quadrants. Fig. 4.2 gives a simple sketch of the AFM.

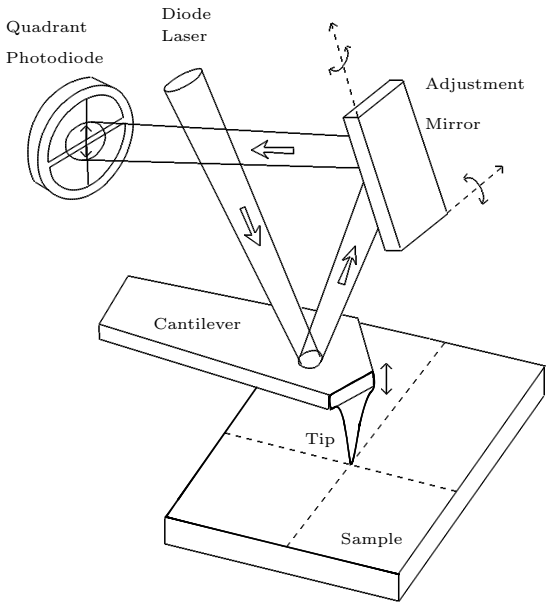

Figure 4.2: Basic AFM sketch using deflection detection.

The cantilevers are loaded on a holder that is attached to a piezoelectric slab crystal. The cantilever is attached at 13° to the laser axis, so that the AFM tip on the lower most side of the cantilever points toward the sample surface. The AFM cantilevers are driven by an applied AC voltage on the piezo-crystal slab to let it swing in z-axis. The amplitude of the difference signal between the upper and lower two quadrants of the photodiode is monitored as the cantilever oscillates at the drive frequency Ω. A feedback mechanism is used to maintain the vibration amplitude of the AFM cantilever

as the tip is raster scanned along the sample surface. This is managed by retracting or extending the tip up and down, depending on the surface topography by the help of a piezoelectric tube on which the tip holder as well as the optical detection mechanism is mounted. The tip vibration amplitude is affected by the interaction of the cantilever tip with the sample surface which can be described as the atomic forces acting between the tip apex and the surface in absence of other types of interaction mechanisms. (Hence the name atomic force microscope.) Fig. 4.3 displays a simple sketch of the tip holder with the AC piezo slab crystal driver. Fig. 4.4 shows the image of the AFM cantilever

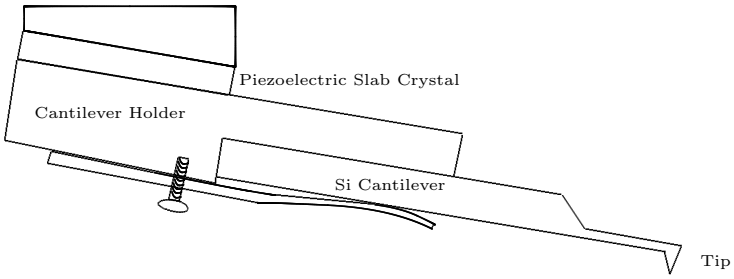

Figure 4.3: Sketch of the tip holder with AC piezo driver.

with the tip underneath imaged from the side. The red colored ($\lambda = 670\,\mathrm{nm}$) cantilever deflection laser spot on the top surface of the cantilever is visible.

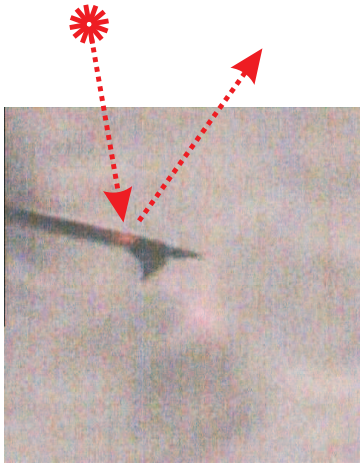

Figure 4.4: Side view of the AFM cantilever tip with the cantilever deflection detection laser illustrated by drawings. Laser spot is visible on the cantilever top.

The cantilever vibration detection unit, the AC piezo driver and the tip holder units

are mounted on a piezoelectric scanner tube in the AFM scan head. The tube is used to raster scan the tip over a surface in both horizontal directions ($150\,\mu$m $\times$ $150\,\mu$m travel in both directions with) and at the same time to retract or extract the tip in vertical direction ($9\,\mu$m travel) while scanning the surface topography. The AFM scanner head also contains the detection electronics. The head is mounted on a coarse approach stepper motor which itself is attached to a granite block from the producer. The AFM unit was installed on a aluminum optical table which was floated on four pneumatic passive vibration isolation legs (Newport). The vibration isolation has improved the AFM operation quality.

4.1.2 Sample scanner stage

For best optical alignment conditions (See Sec. 5.1.2.), it was pursued to scan the sample under the AFM tip rather than scanning the tip over the sample surface, once the tip was aligned to the illumination beam. Because of that reason, a digitally controlled 3-axis sample piezo scanner stage (Physik Instrumente P-517.3CD scanner, E-710.3CD controller) was positioned under the AFM scan head and operated in closed loop mode to scan the sample. The scanner stage was equipped with capacitive sensors in all three axes which allowed for precise positioning of the sample down to 1nm in lateral (x/y) axes and $1\mathring{A}$ in vertical (z) axis. The travel ranges were $100\,\mu$m in x and y and $20\,\mu$m in z. A miniature dove-prism z translation stage was mounted on the piezo scanner for manual coarse approach of the sample towards the tip. The controller unit of the piezo stage was equipped with a digital I/O port, from which trigger signals for every scan line were acquired. The trigger signals were used to synchronize acquisition of other data sources in the setup (e.g. lock-in amplifier in Sec. 4.3.1) with the sample position.

4.2 Optical components

The optics in the *a*-SNOM setup consists free space optics and fiber delivered laser sources which are described in the following sections.

4.2.1 Laser sources and fiber-optics

On top of the granite AFM base, a home-made optical base was fixed in order to keep the optics conveniently close to the AFM unit. The base material was chosen to be "Invar 36" to minimize thermal drift effects on the interferometric measurements. All the optics were mounted such that the beam propagation axis remained at a height of 50 mm from the base surface at which the AFM tip was centered as well. The AFM tip - sample surface system is illuminated by focused laser light and back scattered light is detected by interferometric methods. Fig. 4.5 shows the AFM tip as in Fig. 4.4 but this time illuminated by Ar^+ laser 488nm radiation. I used two different gas lasers in my

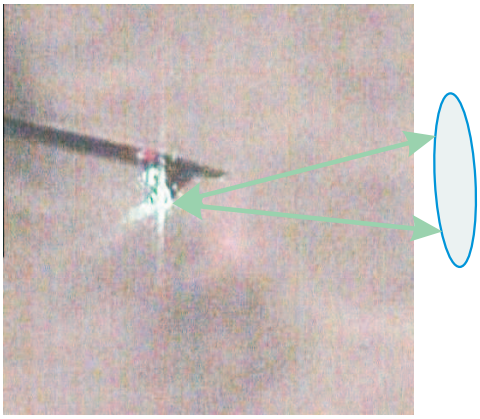

Figure 4.5: Side view of the AFM cantilever tip illuminated by Argon Laser. Cantilever deflection detection laser illustration is removed for clarity. Laser focusing and back-scattering is illustrated.

studies. The first laser source was an Ar^+ ion laser (Coherent Innova 90 Plus) with 1 m cavity giving 5W maximum output power at all lines operation. The output of the laser was vertically polarized. The laser lines at 488nm and 514nm were chosen in the experiments. The other laser source was a HeNe laser (Uniphase 1137) with unpolarized 5 mW output at 633nm wavelength. The optics and the AFM unit were installed on a different optical table than the laser sources. In order to deliver the laser beam to the optical setup, a fiber-optic delivery system was utilized. The Argon laser beam was sharply focused and coupled into a single mode visible wavelength optical fiber by a free-space laser-to-fiber optical coupler (OZ Optics HPUC-23A-488/514-S-6AC-11). The coupler unit was mounted on a five-axis optical mount (Newport M-LP-05) for

fine adjustment of the input axes. The optical fiber was a single end APC-FC (angle polished cleave-fiber connector) connectorized 6 m patch-cord while the second end was left unconnectorized (Schfter-Kirchhoff FC-SM450S#AD025). The APC connectorized end was used for the coupling mounted at 8° of angle to allow for the maximum coupling efficiency. The unconnectorized end was stripped and manually connectorized by a bare fiber FC adapter (OZ Optics) which was connected to an FC receptacle. In the case of HeNe laser, the laser unit was purchased with a variable attenuation fiber optical output pre-mounted on the laser head through a free-space laser-to-fiber optical coupler (Schfter-Kirchhoff 60SMS-1-4-A4.5-02). Output was taken from a 10 m long single mode fiber optical patch-cord, which was FC connectorized on the other end.

4.2.2 Free space optics

The overview of the optical setup is sketched in Fig. 4.1. The laser beam comes from the fiber optical cable which is connected to a fiber holder. The fiber holder is mounted on a two axis optical tilt mount which is fixed on the invar base. The numerical aperture (NA) of the single mode fiber used to deliver the laser is 0.11 resulting in a divergence angle of about 23°. The diverging beam is collimated by a doublet lens (L1) with matching NA and 10 mm focal length and 6 mm diameter (Edmund Industrial Optics). The collimated beam has a diameter of ∼1.7 mm. The collimated beam is split into two by a 50/50 non-polarizing beam splitter cube (BS1) (Edmund Industrial Optics). One of the arms is used as reference, while the other is used to illuminate the tip-sample system. The illumination beam is first frequency upshifted by the aid of an acousto-optic modulator (AOM)(AA Opto-Electronic AA.ST.80/A1-vis-01), operated in frequency shifter mode. The frequency shifter is driven at about $\omega = 80\,\mathrm{MHz}$ by a combination of a frequency tunable driver (AA Opto-Electronic DRF.70-90.B4.1μs) and amplifier (AA Opto-Electronic AMP.50-110.B6) electronics.

Fig. 4.6 gives the sketch of the incoming beam being separated into the 0th order unshifted (ω_0) and undeflected beam (solid line), which is blocked, and the 1st order

beam upshifted in frequency ($\omega_0 + \omega$) and deflected by the AOM (dashed line). The

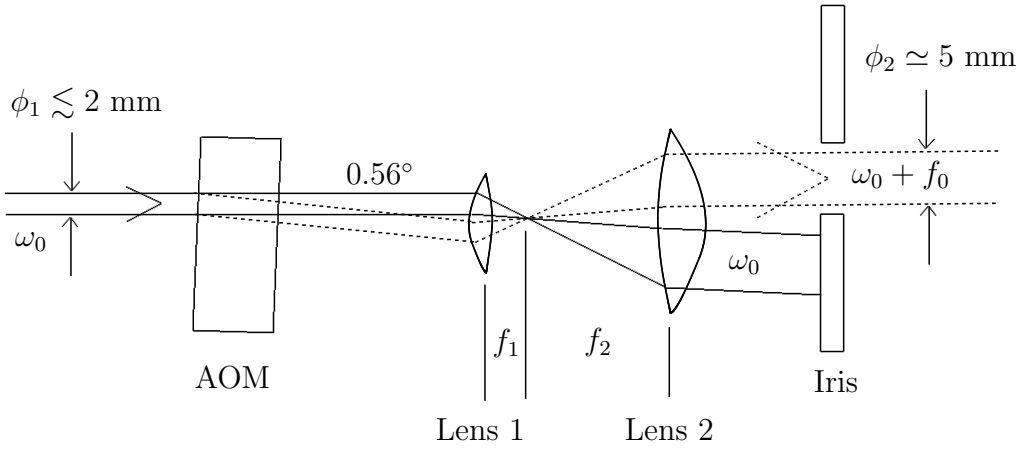

Figure 4.6: Sketch of the light path through AOM together with beam expander. The output beam if upshifted in frequency by Ω_0.

angle between the 0th and 1st order diffracted beams is 0.56°. This much separation between the shifted and unshifted beams requires travel over long distances for sufficient reduction of the overlapping parts of the two beams. In order to shorten this distance both of the beams are expanded with a two lens optical system. The first lens (L2) is a $f_1 = 6.2$ mm asphere (New Focus 5723-A-H), and the second one (L3) is a $f_2 = 18$ mm plano-convex (Edmund Industrial Optics). With the expansion coefficient of $f_2/f_1 \simeq 1.9$ and input diameter of $d_1 \lesssim 2$ mm, the resulting output beam diameter is $d_2 \simeq 5$ mm. The unshifted beam is blocked and the shifted beam is passed through an iris aperture beam stop.

This 5 mm diameter frequency upshifted beam is used to illuminate the tip. The beam first travels through a 50/50 beam splitter (BS2) (Newport 10B20BS.1 $\lambda/10$ surface flatness) which is used to join the reference beam with the back scattered signal from tip-sample system. Then it is projected onto the AFM tip through a home made "periscope" unit with an angle of about 30°. Fig 4.7 shows a sketch of the unit. It is composed of two mirrors and an aspheric lens with $f = 11$ mm. The mirrors (Thorlabs PF05-03-F01/G01) are mounted on two axis tilt stages (Thorlabs KS05/M). The lens

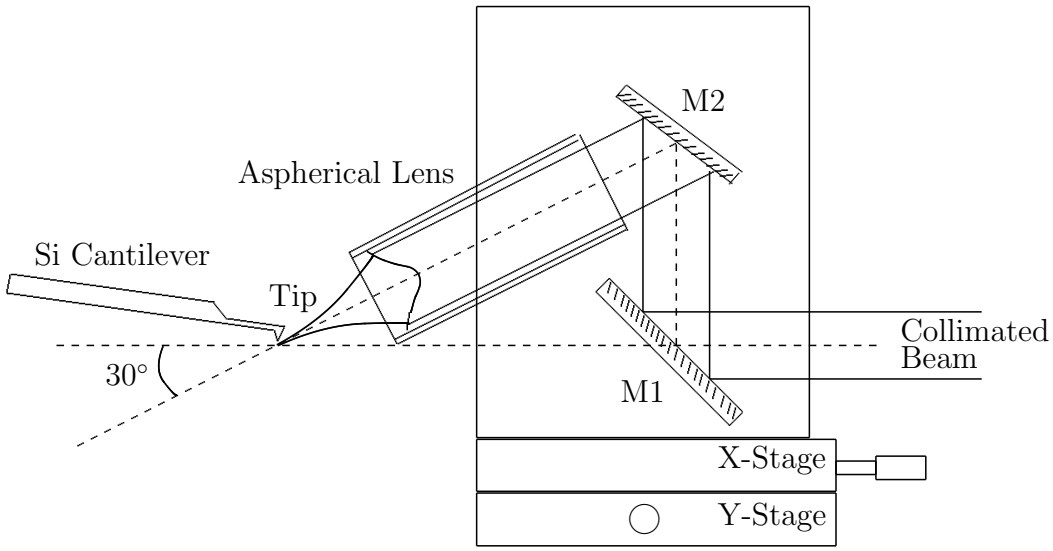

Figure 4.7: Sketch of the periscope for 30° tip illumination.

(Edmund Industrial Optics Geltech 0.25 NA) is fixed at one end of a cylindrical steel tube. All three pieces are attached to a common base which is mounted on an xy translation stage. The illumination beam, with the optical axis at the 50 mm level on the invar base, is first 90° diverted upwards with the first mirror and then reflected down with the second mirror such that it makes 30° angle to the lateral direction. The beam is then focused by the aspheric lens onto the AFM tip apex at about 8 mm working distance. The xy translation stage makes it possible to align the beam on the tip in two dimensions, where the z alignment is done by moving the AFM scan head. When the alignment is accomplished, the sample is approached to the tip from below. The further details about the alignment and approach are given in Sec. 5.1.2.

The back scattered light from the AFM tip is joined with the reference beam at BS2. The reference beam, which is generated at BS1, is first let to travel a delay line. The delay line is simply a retro-reflector positioned at a certain distance to allow for equating the optical path lengths of the reference (ref) and signal (sig) beams. The reason is the short coherent length of the laser source. In order to keep reference and the signal beam paths about the same length, this delay line is introduced in the reference arm of the interferometer. The details about the effect of the coherence length are discussed in Sec. 5.1.1. The joined beams are focused with a $f = 100$ mm lens onto the detector,

which is an avalanche photodiode (AP(d) in the setup (Hamamatsu C5331-02).

In addition, a reflective ND filter attenuates the reference beam to about 0.1 mW optical power which is necessary to keep the APD in the linear response regime. The reflected beam is used to monitor the laser power. The monitoring is done by a photodiode which generates a photo current. This voltage is used to normalize the interferometric detection signal. (See Sec. 4.3.1.)

4.2.3 Interferometric signal amplification

In this section the interferometric detection scheme used in my *a*-SNOM setup is studied. The idea behind following the higher order modes of tip modulation in the heterodyne beat signal is explained by demonstrating how various field components arrive at the interference orders. The field intensities near the tip - surface interaction volume are estimated to be two to three orders of magnitude below the detectability level of highly sensitive photodiodes. In this respect interferometry plays a key role for the realization of the instrument since it involves magnification of the detected signals. This aspect of the interferometry is also described in this section.

The heterodyne detection scheme for optical radiation is rather similar to FM radio reception, where a *local oscillator* is tuned such that the mixing with the weak antenna signal creates a temporal beat signal (usually at 10.7MHz.) This beat signal is then further processed to create audible sound. That is, the energy that creates the detectable signal it *not* provided by the transmitter antenna, but locally in the interference admixture. Similarly in the optical detection; the signal source (*i.e.*, the scattering sample) radiates waves that carry information, but the energy necessary to extract that information is provided locally by a strong, frequency-shifted reference signal.

Consider two fields that overlap at the detector with field strengths

$$\mathbf{E}_j \;=\; \mathbf{E}_{0j} \exp i\left(\omega_j t + \varphi_j\right) \;, \tag{4.1}$$

where $\mathbf{E}$ is the instantaneous field strength, $\mathbf{E}_0$ its amplitude, and φ its phase. $j = 1, 2$ is

the index for the waves. The interferometric sum field $\mathbf{E} = \sum_j \mathbf{E}_j$ results in a detected intensity

$$I = |\mathbf{E}|^2 = I_1 + I_2 + 2\cos(\Delta\omega t + \Delta\varphi)\,\mathbf{E}_{01} \cdot \overline{\mathbf{E}_{02}}\ . \tag{4.2}$$

I am interested in the interference signal, that is, the last term in this equation, as it carries amplitude, phase and polarization information. To understand how I can extract this information, I consider beam 1 as the reference beam, which I manipulate to my desire and beam 2 shall be the radiation signal coming from the sample.

The interference of reference and sample signal exhibits a temporal beat at the frequency $\Delta\omega = \omega_{sig} - \omega_{ref}$ due to the heterodyne frequency difference between the two beams. This allows me to use a lock-in amplifier, operating at the beat frequency (in my case $\Delta\omega \approx 80\,\mathrm{MHz}$,) to very effectively filter out the DC component $I_{sig} + I_{ref}$, as well as take advantage of the excellent noise-reduction of lock-in detection. In an experimental realization, the lock-in amplifier will thus measure at the reference frequency $\Delta\omega$ the signal

$$s\cos(\varphi) \tag{4.3}$$

with the amplitude and phase given by

$$s = 2\mathbf{E}_{sig} \cdot \overline{\mathbf{E}_{ref}}\ , \tag{4.4}$$

$$\varphi = \varphi_{sig} - \varphi_{ref}\ . \tag{4.5}$$

From this expression three important conclusions about measurable quantities can be drawn:

1. The lock-in will measure an amplitude proportional directly to $\mathbf{E}_{sig}$. As the reference field strength is kept constant, this is a direct measure of the *optical field strength* $\mathbf{E}$ of the sample signal. This contrasts with standard direct optical mea-

surements (non-interferometric detection,) which yield an *intensity* $I = |\mathbf{E}|^2$.

2. A dual-phase lock-in amplifier also records the relative phase $\varphi = \varphi_{sig} - \varphi_{ref}$. Most importantly, this phase carries information due to scattering phase shifts, which are highly dependent on the sample material. This provides a another sensitive channel for material contrast.

3. I can select one of two polarization states of the sample signal of my desire (for instance horizontal/vertical linear or left/right circular polarization) by preparing the corresponding polarization $\mathbf{E}_{ref}$ in the reference beam. In principle one may split the signal beam into several individual beams and detect separate polarization states simultaneously by interfering them with different reference beams each. Or one could introduce a reference beam that oscillates between the two polarization states and thus gives a relative difference signal between these two states, similar to reflection anisotropy spectroscopy or circular dichroism spectroscopy.

The focus of the present thesis is on the amplitude and phase of linearly polarized scattered light. In this case, the observed signal amplitude is proportional to

$$s \quad \propto \quad \sqrt{I_{ref} I_{sig}} \,, \tag{4.6}$$

which illuminates another advantage of the heterodyne detection scheme, namely the *amplification* of an otherwise too weak signal. Numerical simulations predict signal intensities of the order of as little as $I_{ref} \approx 10^{-12}\,\mathrm{W} \approx 10^{7}\mathrm{photons/sec}$, which are below the noise floor of current photodiode detectors. (In this case, even photomultiplier tubes and other single-photon detectors do not work well in conjunction with a lock-in amplifier operating at $10^{8}\,\mathrm{Hz}$.) By interfering this signal with $I_{ref} \approx 10^{-4}\,\mathrm{W}$, however, the signal at the detector is boosted to $s \approx 10^{-8}\,\mathrm{W}$, which is well within the detection limits of current photo detectors.

Finally, regarding the optical phase information, a serious artificial contribution has to be mentioned, which is due to the optical path difference of the two beams as they

travelled through the space before reaching the detector. This spurious information is best kept constant by ensuring minimal temperature fluctuations, air convection and sound waves in the experimental setup. I also found that using low thermal expansion coefficient materials such as "INVAR 36" improves the instrument performance dramatically.

4.3 Data acquisition electronics

4.3.1 Generation of the electronic reference signal

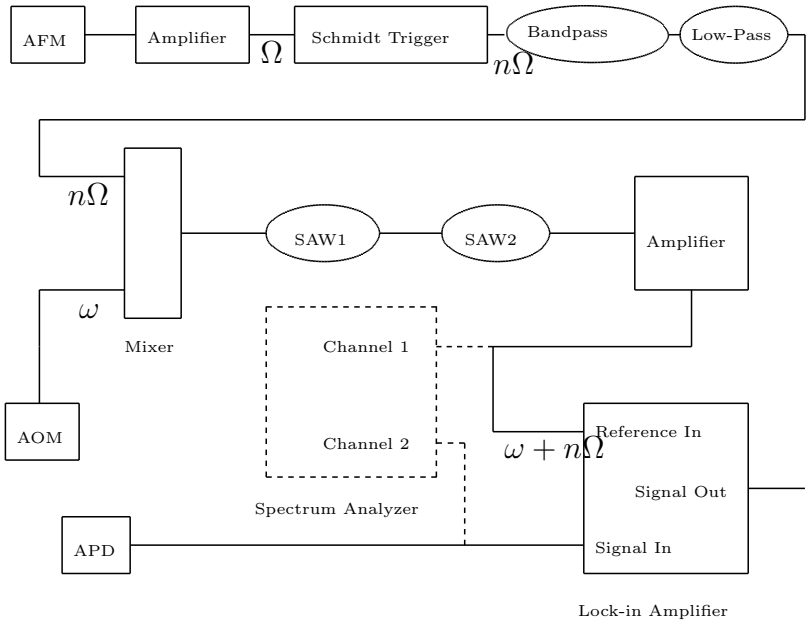

Figure 4.8: The electronics chart.

The detected signal at the APD contains a beat signal at around $\omega = 80\,\mathrm{MHz}$ as a result of heterodyne interference of the two frequency shifted beams. Further, this beat signal is modulated by the AFM tip vibrational motion at the cantilever frequency Ω and its harmonics. Because the harmonics at $\omega \pm n\Omega$ where $n = 1, 2, 3$ are of my interest(see section 4.2.3), I demodulate the detected signal APD at these frequencies. This is done by generating reference signals at $\omega \pm n\Omega$ by the help of specially designed electronics which serve as reference input to a lock-in amplifier (Stanford Research Systems SR844).

The lock-in is used in the so-called ratio mode which divides the detected amplitude to an external normalization voltage. As mentioned in Sec. 4.2.2, the laser power is monitored throughout the experiments with a photodiode. The photocurrent is amplified and converted to voltage which lies between 0 V to 10 V with a home built current-to-voltage amplifier with variable sensitivity. This way the laser power oscillation and settling effects as described in Sec. 5.1.3 are cancelled on the absolute amplitude readings of the lock-in amplifier.

The AFM frequencies usually lie between 50 kHz to 500 kHz. Obtaining a clean, phase-following 80 MHz + 50 kHz is not straightforward. Use of the original signals which drive the AOM and are detected by the AFM is a must in order to maintain the phase information.

The AFM vibration signal from the quadrant detector is taken from the electronic controller box. It is first amplified and then rectified by a Schmidt trigger. The resulting rectangular signal is a superposition of many Fourier orders. When this rectangular signal is filtered with 6th order Butterworth band-pass filters of suitable band widths and band center positions, one can choose a certain target harmonic of the original signal. This way I obtain any order harmonic of the AFM frequency, that is $n\Omega$. Because the cantilever eigenfrequencies span the 50 kHz to 500 kHz range, the harmonics up to 3rd order spanned 150 kHz to 1.5 MHz. A series of 20 such filters were built and tested to meet the requirements and are kept at hand as a batch to choose from with respect to AFM cantilever frequencies.

The signal obtained with this method is low-pass filtered by an 8 MHz edge filter in order to suppress any high frequency noise. The resulting signal is mixed with the 0dB AOM drive frequency ω, that is taken from the reference out port of the RF driver. The resulting signal from the mixer contains $\omega - n\Omega, \omega, \omega + n\Omega$. In order to obtain $\omega + n\Omega$ only, one needs either a sharp edge filter or a very narrow band-pass filter. For example, for a cantilever of $\Omega = 200$ kHz, and interest on second harmonic ($n = 2$), one needs to isolate the 80 MHz + 2 × 200 kHz = 80.4 MHz signal from the 80.0 and 79.6 MHz

mix signals. This is an interesting requirement regime for finding the best suited filters. With classical RLC filters, in order to get such steep filter edges one needed to go to extremely high cascade orders, that would eventually diminish the throughput of the filter. So this solution is impractical. Another solution are quartz filters. But the Q factor of such a filter is too high. The bandwidth of such a filter is so narrow that it would be practically impossible to meet and/or keep the necessary center frequency, because RF circuitry is notoriously difficult to stabilize thermally. Therefore, the use of surface acoustic wave (SAW) filters became an interesting option. These filters have about less than 1 MHz bandwidth with 75dB extinction. I use two cascaded SAW filters of 80 MHz center frequencies with 20dB amplifiers in between in order to maintain the $\omega + n\Omega$ at 80 MHz with the help of a tunable AOM frequency ω (see Sec. 4.2.2). The overview of how the electronics works can be found in Fig. 4.8.

A spectrum analyzer (HP 8568(a) was crucial to determine the most appropriate AOM frequency for a given AFM cantilever frequency in order to adjust $\omega + n\Omega$ to fall into the SAW filter band. The same instrument was also used to analyze the APD signal and the beat signal and cantilever harmonics evolution was monitored live as the optical alignment for interferometry was done.

The sample scanner stage, the spectrum analyzer and the lock-in amplifier, were communicated via IEEE 488 (GPIB communication protocol by a GPIB communication card (National Instruments). The instrument control and data acquisition were automated through a C code (LabWindows). The AFM was controlled by a stand alone software from the producer.

4.3.2 Synchronized scanning and data acquisition

The precise translational movement of the 3-axes sample piezo stage is achieved by a digitally controlled closed loop controller, which can be programmed to generate user-defined waveforms in the x/y plane. For the *a*-SNOM, the pattern is simply a constant speed linear motion through a fast axis (either the x or the y axis.) While the sample

stage is moving under the AFM, the lock-in amplifier periodically records data of up to two channels. For exact synchronization of the start of each fast axis scan, trigger signals from the sample stage are sent to the lock-in amplifier. To avoid lateral distortions, the triggers are defined to signal the beginning of the linear motion of the fast axis scan after the initial acceleration time.

The lock-in amplifier is capable of automatic data acquisition of two channels at a time (at a sampling rate of 1/16 to 512Hz.) Typically, these are the interferometric amplitude s_n, phase φ_n at the n-th demodulation order of the tip frequency, and/or an auxiliary input voltage, such as the topography signal generated by the AFM, thus allowing topography data to be acquired by the lock-in amplifier in perfect synchronization with the optical signals. The data is accumulated in internal memory and transferred en bloc to the computer after each line scan reducing the time, required for data transfer.

Typically, for *a*-SNOM, the line scans are recorded in both the forward and backward direction of the chosen fast scan axis. In one direction the optical amplitude and the optical phase is collected and in the other direction the optical amplitude and the topography. This way at one go four images are produced.

Compared to a pixel-by-pixel data acquisition, the triggered line-by-line acquisition technique is advantageous in shortening the duration of imaging times (more than 10 fold in some cases), providing better line-to-line alignment, and increasing the image quality by reducing long term drift effects considerably.

Chapter 5

Instrument characterization

In apertureless scanning near field optical microscopy (a-SNOM) by means of heterodyne interferometric detection it turns out that the operator has to have good insights into both optics and atomic force microscopy to run the instrument in a proper way to acquire reliable data free of topographical and other artifacts.

In this chapter I report on the results of my studies of the various aspects of instrumentation for the a-SNOM as tested and evaluated for successful operation. These aspects include evaluation of the general properties of individual instrument parts as well as their synchronized operation in generating reliable data. The characterization measurements conducted on individual elements of a-SNOM are: the illumination source power stability, excitation of higher harmonics, coherence length, interferometric stability, tip-sample-illumination alignment, and tip-sample approach. In addition, further tests are made on spatial resolution, simultaneous acquisition of optical amplitude, phase and topography, tip versus sample scan modes, enhancing contrast by higher harmonics demodulation, effects of tip drive and vibration amplitudes.

5.1 Fundamental requirements

The prerequisite condition for a successful a-SNOM operation is that all instrument parts have to meet the requirements for necessary efficiency. These fundamental re-

quirements can be listed as the following: Maintaining the interferometer path length difference at the order of the coherence length of the laser source; proper alignment of the AFM tip with the illumination focal volume; immunization of the optical signal against the time variations of the laser power and maintaining a stable interferometer operation.

5.1.1 Coherence length and contrast

Visibility in coherent optics – that is the ratio of constructive to destructive amplitude – strongly depends on the path length difference of the two interfering arms. The reason is that the two arms must be coherent in time and space as much as possible for the best constructive and destructive interference result. For this the difference of the two interfering beam path lengths must be kept smaller than the effective coherence length of the laser in order to obtain reasonably strong interference.

Introducing a delay line at the reference arm has proved to be crucial for optimizing the interference amplitude in my setup. In the first version of the interferometer setup, the observed interference signal was strikingly less than expected and hardly recordable. Therefore I have placed a retroreflector in the reference arm mounted on a linear translation stage. The reference beam coming from the first beamsplitter is first 90° reflected by a mirror and then back-reflected from a retroreflector in an off centered way with $1-2\mathrm{cm}$ beam separation back into the original direction. A Δl translation of the retroreflector causes a $2\Delta l$ change in the reference path length without changing the relative alignment of the beams. In this way I was able to steer the reference beam arm length in a controlled manner and optimize the interference signal on the detector.

For the minimization of the path length difference I have replaced the AFM tip with a reference mirror. So both of the reference and frequency shifted arms' powers could be easily set to have equal portions at the detector by the help of variable ND filters. The interference signal in the detector is fed into a spectrum analyzer for observation. In this setup I expected to observe a strong beat signal between the shifted and reference

arms at the shift frequency of $\sim 80\,\mathrm{MHz}$.

Fig. 5.1 shows the interference signal as monitored by the spectrum analyzer as a function of path length difference between the two interfering arms.

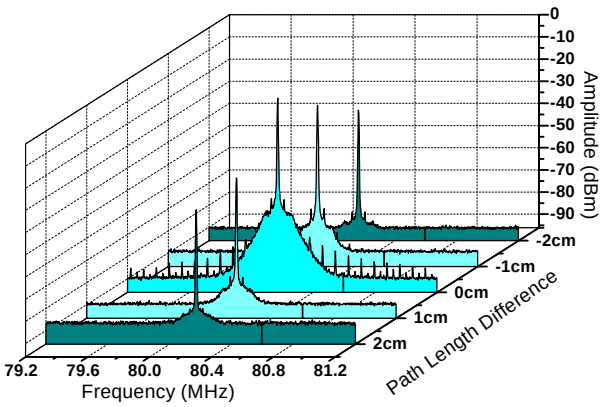

Figure 5.1: Effect of the path length difference on the interference amplitude.

It can be seen that minimization of the path length difference successfully achieves optimal amplification of the interference signal.

5.1.2 Opto-mechanical alignment

Overlapping spatially an AFM tip apex with an illumination beam focal spot about 2μm width and the sample under investigation in three dimensions with accuracy of less than 10 nm is not a trivial task. There are several pitfalls one encounters while moving one or the other. In this section I give the methodology that I developed in order to maintain reproducible and reliable alignment by the help of the flexibility I had having both the sample stage and the AFM tip as scanning units.

With relative ease, two of those can be brought together: AFM tip with sample by the aid of AFM feedback. The first step is therefore to scan the illumination beam focus with the AFM tip with the sample retracted to far below the tip apex/beam focus volume. In Fig. 5.2 the focal volume imaged by scanning the tip through the illumination beam focus is illustrated. The scan is made in a horizontal plane and s_1 is recorded. The scan is made on a $23\mu\mathrm{m} \times 23\mu\mathrm{m}$ area. The peak appears extended in the beam propagation direction as a result of the 30° angle between the beam field depth and the

scan plane. By repeating these scans at various horizontal planes in z direction, one can map the whole focal volume of illumination. This allows one to choose the optimal 3-dimensional position.

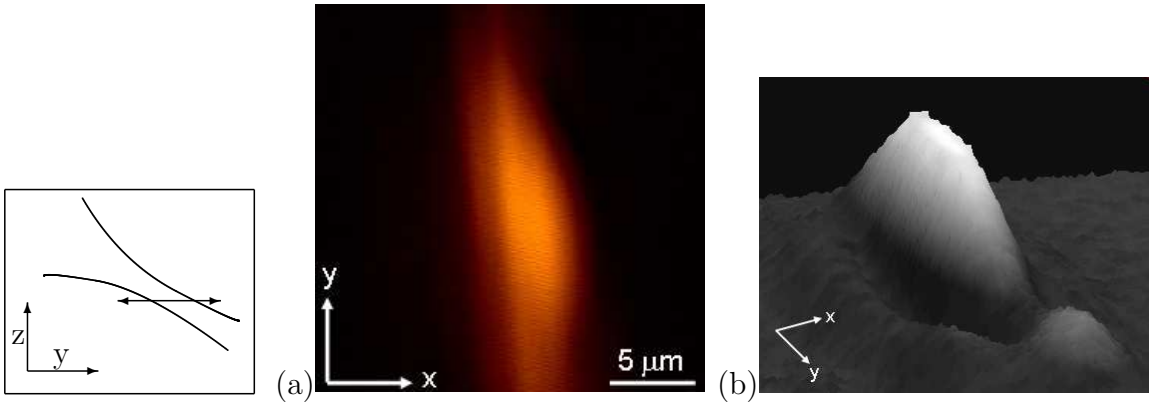

Figure 5.2: (a) The s_1 signal recorded while the tip scanned a $23\,\mu\mathrm{m} \times 23\,\mu\mathrm{m}$ area containing the illumination focus with the sample retracted. (b) The 3D view of the focal volume cross-section imaged by scanning the tip through the illumination beam focus. Such scans allow an easy alignment of AFM tip and optical focus before the sample is approached.

The geometry of the most common AFM tip architecture (See Fig. 5.4.) is found to be not the best for apertureless SNOM. The fact that the tip protrudes downward, somewhat obscured below the AFM cantilever beam, results in several difficulties in optical alignment in case of oblique incidence of 30° for tip illumination. The effect of this geometrical obstruction is displayed in Fig. 5.3. In this figure a side view photo shot of the illuminated tip is recorded for different tip positions in the horizontal plane. The photos correspond to the positions as marked on the left hand scan, which is a similar scan as displayed in Fig. 5.2.

The corresponding photos in Fig. 5.3 suggest that the strong signal lobe observed in the lower quarter of the left hand side of Fig. 5.3 is a result of strong scattering from the cantilever beam end instead of the tip apex which is a large obstacle in the path of the illumination beam travelling towards the tip apex.

Although this type of alignment procedure works fine, it takes up to several hours for the user to establish the optimum conditions using this type of cantilever after a simple tip exchange. Taking x/y scans at different z planes to find the optimal z position,

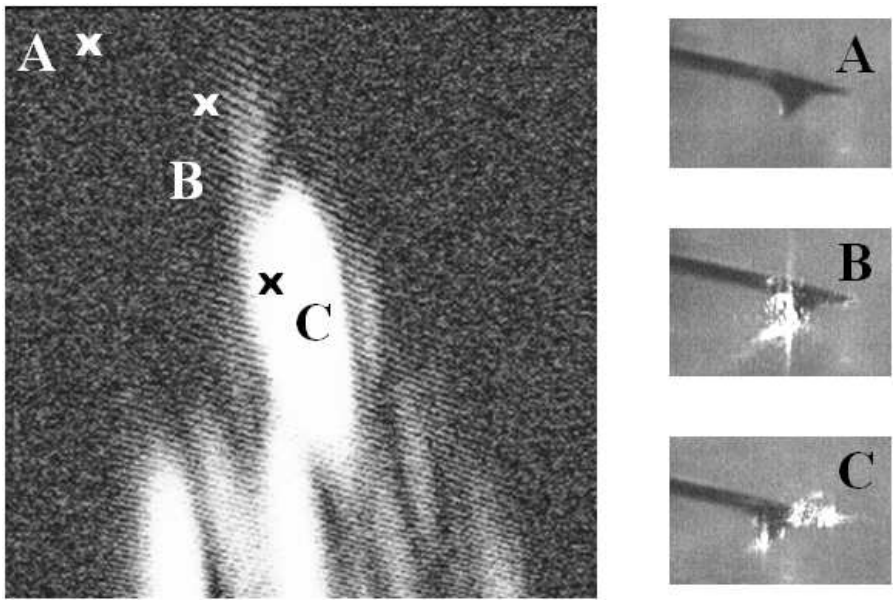

Figure 5.3: The cross signs show the position of the tip on an s_1 $x-y$ scan image as the photos on the right were taken.

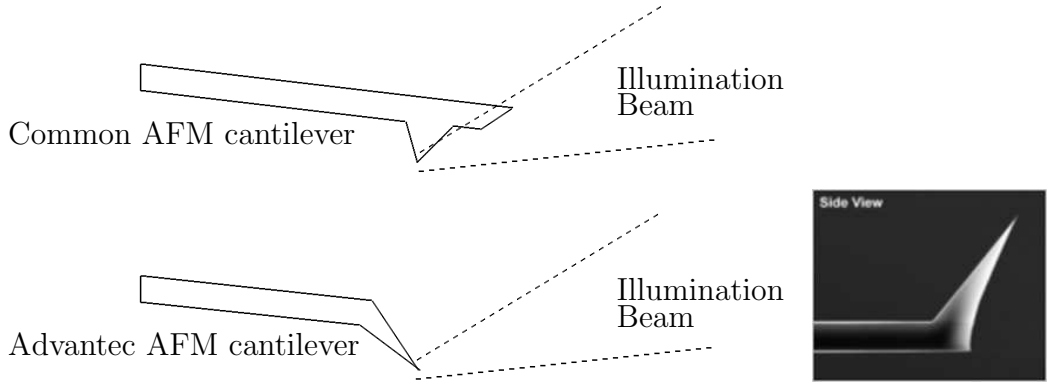

Figure 5.4: The first sketch shows how the end of the cantilever beam enters the beam, shadowing the tip apex in the common AFM cantilever geometries. The second sketch shows the geometry of a more suitable cantilever that could be used for *a*-SNOM. An SEM image from the manufacturer of this type of tip is displayed on the right.

and then positioning the tip and/or taking side-view photos for finding the optimal x, y position and is a long and impractical solution. One can remove the need for such a long optimization procedure by switching from regular AFM cantilever-tip geometry to a special geometry as shown in Fig. 5.4. The lower cantilever-tip profile was a simple sketch of a kind of tip that suits best the needs of the *a*-SNOM both for ease of alignment and more reliable imaging. Luckily this type of cantilevers (Nanosensors, AdvanTEC® Silicon SPM-sensors) became available in the AFM probe market almost simultaneously

as the apertureless SNOM instrument construction was approaching its final form.

5.1.3 Stability

Laser stability

After turn-on, the HeNe laser shows a long term trend of rising power which settles after about one hour. On top of this slow trend one observes small oscillatory amplitude fluctuations of varying frequency over time that settle over several hours. In Fig. 5.5(a) the laser power monitored during the first and sixth hours after turn on can be seen.

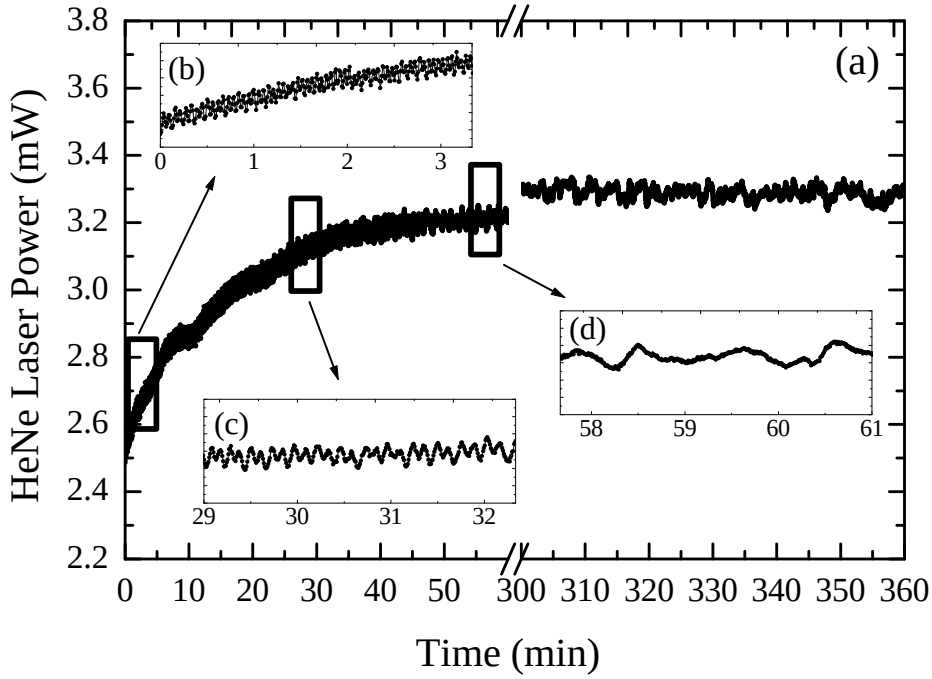

Figure 5.5: Laser power monitored during first and sixth hours after turn on

When zoomed into 200 second periods of data taken at the beginning, 30 minutes after, and 60 minutes after turn on; the change in the short term variation of the laser power can be seen. Figs. 5.5(b), (c) and (d) show that the frequency of this short term variation in power drops. This kind of behavior most likely originates from laser cavity reaching thermal equilibrium. After 5 hours of operation the laser power still shows fluctuations, which are, however, no more of oscillatory but random behavior. 1 hour long monitored laser power after 5 hours of laser operation is shown in the second half

of Fig. 5.5. One option to control these fluctuations in power is to introduce a so-called "noise-eater" right after the laser, before its radiation is delivered to the experiment. For sake of simplicity, I chose an alternative option, namely, to measure the instantaneous power at the sample and to normalize the lock-in amplifier output with this signal. The details have been described in Sec. 4.3.1.

Interferometer stability

Another aspect of the *a*-SNOM is the time stability of the interferometric measurements. A bidirectional surface scan, acquiring 4 channels with 256 lines at about 2.5 sec/line takes about 21 min of acquisition time. Moreover, the acquisition time increases linearly with number of scan lines implying even longer acquisition times when more number of lines is required. In some cases the acquisition times may reach 30 minutes to one hour. This brings up the question of interferometer stability over time.

Since the detection scheme depends on the superposition of two optical signals at the detector, the optical paths travelled by the superposed beams play a role in the amplitude and phase of the monitored signals, s_n and φ_n. The spatial overlap of the signals are affected by the deviation of the optical paths from optimal position adjustment due to thermal effects. The first version of the interferometer was built on an Al baseplate which had a considerable thermal expansion coefficient at room temperature; the *a*-SNOM was operated in ambient conditions such that the *a*-SNOM setup was not ideally isolated from any air movements or density fluctuations in the optical paths. This has brought problems with it, since during the acquisition times as long as 30 min the optical adjustment of the interferometer was drifting away from optimal.

In order to overcome this time stability problem, I replaced the aluminum base plate of *a*-SNOM with an "INVAR 36" base plate with less than 15 times the thermal expansion coefficient of Al at room temperature. In addition, I placed the entire *a*-SNOM setup inside a plexiglass isolation enclosure which sufficiently isolated it from air convection and sound waves. The effect of the invar base and acoustic isolation dome

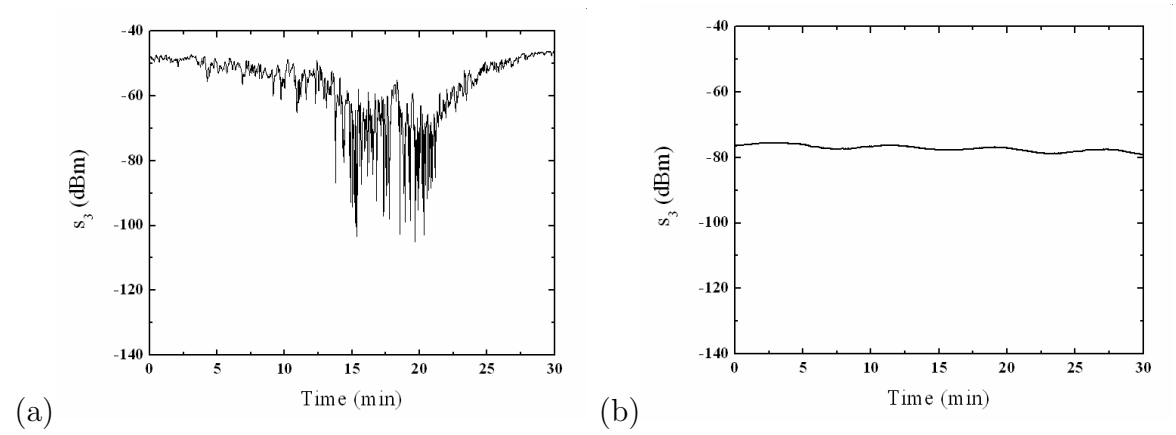

Figure 5.6: The s_3 amplitude monitored over 30 min with interferometer (a) built on aluminum base and in ambient conditions, (b) built on invar base and placed in an acoustic isolation dome. Here, the interferometer was operated in homodyne mode. The dramatic effects on the amplitude would translate to similar effects on the phase in the case of heterodyne operation.

are displayed in Fig. 5.6. A 30 min acquisition of s_3 is given in Fig. 5.6 with (a) Al baseplate and without isolation enclosure, (b) invar baseplate and with acoustic isolation enclosure. As a further improvement, I also replaced long and thin posts carrying the optics with short and thick ones to ensure robustness of the interferometer and replaced regular mirror and lens holders with ultra-stable versions.

5.2 Scanning data acquisition

5.2.1 Simultaneous imaging of topography and near field optical amplitude and phase

It is highly desirable for the implementation of *a*-SNOM as a standard lab instrument to be able to *simultaneously* acquire the sample topography with the optical near field amplitude and phase (and possible further user-defined data channels.) As the *a*-SNOM is based on a dynamic mode operation AFM (see Sec. 4.1.1), the topography information is already generated in the AFM feedback electronics that control the tip-sample distance.

The commercial AFM was originally designed to operate in tip scan mode with stationary samples. In order to keep the AFM tip versus illumination beam alignment

undisturbed during the scan, I opted to change the AFM operation mode into a sample scan mode with stationary tip. (For convenience, the tip-scan mode is still available, though; see Sec. 5.2.2.) For being able to keep the simultaneous AFM imaging capability in this new configuration, an optional external signal access module specially designed for this AFM instrument was obtained from the manufacturer. With the help of this unit, it is possible to read out the topography data in form of a voltage signal. Feeding that into one of the auxiliary input ports of the lock-in amplifier, allows to record the topography signal and the near-field signal truly simultaneously in the two different input channels recorded by the lock-in.

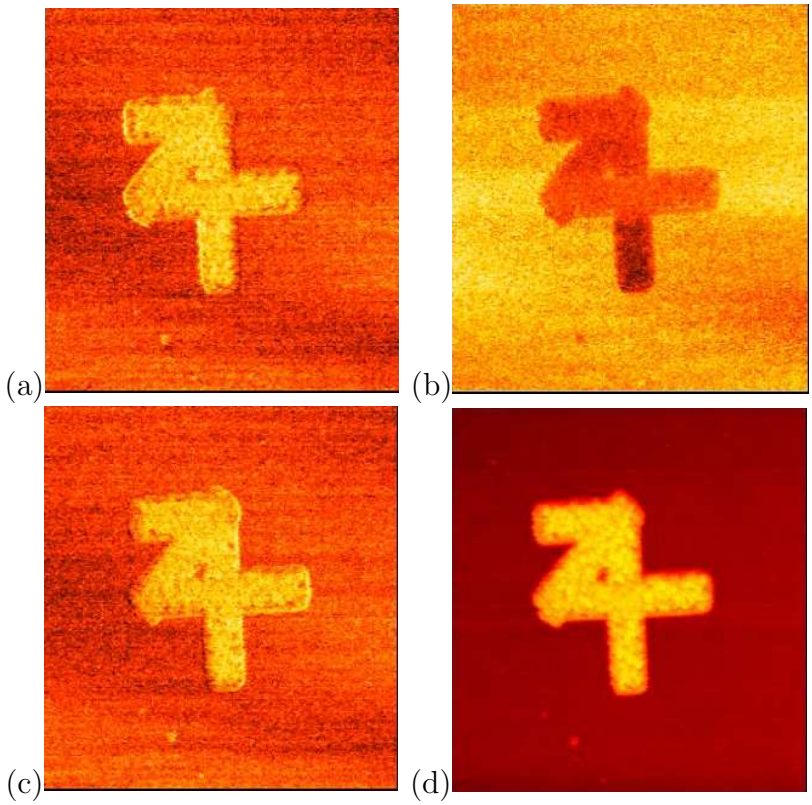

Figure 5.7: Standard set of data recorded with the *a*-SNOM. Shown here is a 5μm $\times$ 5μm area with a 60nm thick Au pattern on a 100nm thick SiO_x substrate on Si. Simultaneously acquired are (a) s_3 and (b) φ_3 during the fast scan axis forward motion (here left-right) and (c) s_3 and (d) topography data on the return track.

A demonstration of the simultaneous imaging capability of *a*-SNOM is given in Fig. 5.7. Imaged was a 5μm $\times$ 5μm area of a silicon oxide-on-silicon (SOS) substrate surface (100nm oxide layer), with a 60nm thick Au pattern fabricated by lithography

and metal evaporation. The four partial images represent the standard mode of data acquisition now established with the a-SNOM. (a) s_3 and (b) φ_3 are recorded simultaneously in the forward scan direction along each line, and (c) s_3 and (d) the AFM topography are recorded on the back track. Here, the fast scan axis is the horizontal axis.

5.2.2 Tip scanning versus sample scanning

As mentioned in Sec. 5.2.1, the sample scanning configuration is favorable in a-SNOM as it maintains an undisturbed tip apex/optical focus alignment during the scan. Nevertheless, for a scan area that is sufficiently illuminated by the exciting focal field, it is possible to do imaging by tip scan and still acquire optical data—modulated, of course with the envelope of the local amplitude and phase of the exciting beam focus. Tip scanning has the advantage of being some 2 to 8 times faster due to the high-speed data acquisition of the commercial AFM and is thus very useful for gaining an overview.

(a)  (b) 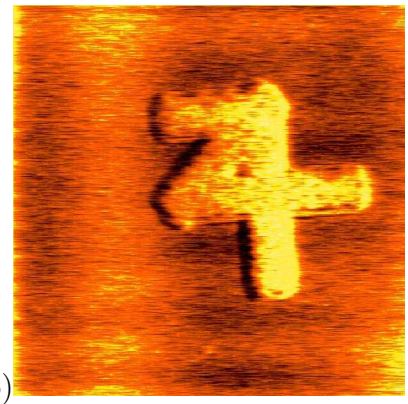

Figure 5.8: This figure shows s_3 belonging to a $5\mu\mathrm{m} \times 5\mu\mathrm{m}$ area with 60 nm thick Au pattern on a 100 nm thick SiO_x substrate on Si. The image in (a) is acquired by scanning the sample below the fixed AFM tip, whereas in (b) acquired by scanning the AFM tip on the fixed sample. The illumination spot had about $3\mu\mathrm{m}$ wide waist at the focus. Clearly, imaging artifacts are perceptible in the tip-scanned image due to the high speed and the focal amplitude envelope.

In this operation mode, the strategy of data acquisition was different from the previously explained sample scan mode. It utilizes the external signal input capability of the AFM electronics for obtaining the optical images. For instance, the s_n is taken out from

the lock-in amplifier in form of an analog voltage signal and fed into the auxiliary input port of the AFM electronics. By activating the corresponding auxiliary input channel with the AFM control software, it is possible to get the tip scan s_3 image of the same sample as in Fig. 5.7. For a comparative display, the tip scan image was line by line flattened by an image processing software. Two typical images of the same sample area, taken by the two different operational *a*-SNOM modes are displayed in Fig. 5.8.

5.3 Mechanical and optical contrast crosstalk

Ideally, the interference signal between the unshifted reference beam and the 80 MHz frequency shifted beam, scattered off the bulk of an AFM tip vibrating at Ω (i.e., not the scattered near field contribution from the apex,) contains only components at 80 MHz and 80 MHz $\pm\,\Omega$. This holds strictly, only if the AFM tip motion is purely sinusoidal. However, the AFM tip vibration can and usually does deviate from a purely harmonic $n \times \Omega$ form and has non-vanishing Fourier components at higher overtones $n \times \Omega$ ($n = 2, 3, ...$). Generally this occurs when the cantilever is driven too hard and the effective potential describing its motion becomes significantly anharmonic. Unfortunately for *a*-SNOM, when this *mechanical anharmonicity* sets in, it generates crosstalk with the purely optical anharmonic near-field signal contributions (see Sec. 3.1.2.) I have developed a number of strategies to ensure the truly near field optical nature of the recorded signals when the sample is in engaged by the *a*-SNOM (Sec. 6.2.)

Certain limitations on the allowable cantilever amplitude, however, can be obtained even without the sample. A *minimum* amplitude is set by having to avoid the "snap-in" problem when the sample is approached. If the vibrational amplitude is not large enough, true non-contact mode conditions can not be accomplished, and the AFM tip makes spontaneous contact with the sample at close distances, leading to a highly anharmonic "intermittent contact" mode. A quantitative study [96] of true non-contact AFM reports that if

$$A \gtrsim \frac{200\,\mathrm{nN}}{k} \ ,$$

where k is the spring constant (in N/m) of the cantilever and A is the vibrational amplitude, snap-in is avoided.

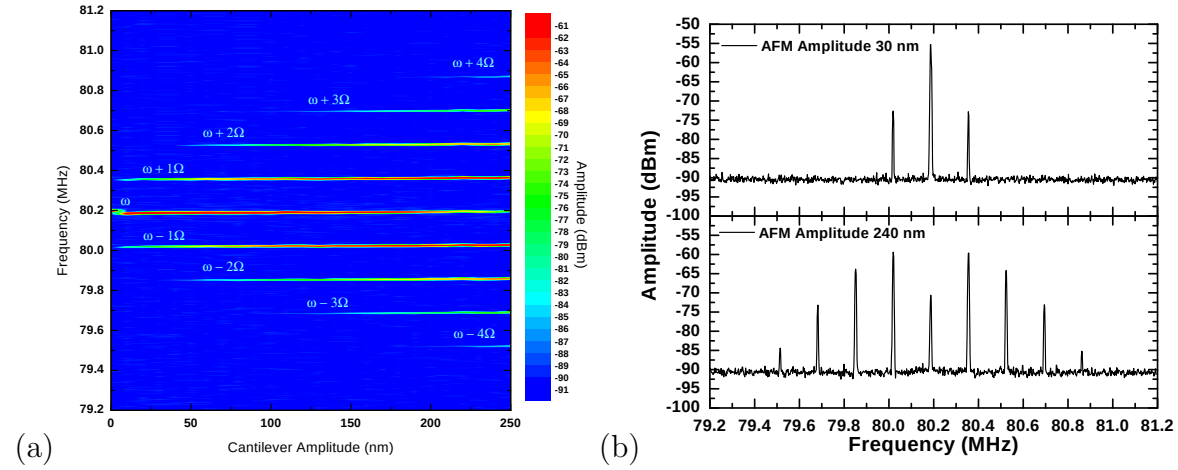

Figure 5.9: (a) As the AFM amplitude exceeds $\sim$ 30 nm, higher order interference terms start to emerge which are entirely due to mechanical anharmonicities of the free cantilever. The AOM shift and AFM vibration frequencies are denoted by ω and Ω, respectively. (b) The interference signal for 30 nm and 240 nm vibration amplitudes.

An upper limit for the vibrational amplitude allowable for sinusoidal motion can be measured with the help of the optical detection setup of the *a*-SNOM. During this check, the backscattered signal from the properly aligned AFM tip is monitored on a spectrum analyzer as the AFM cantilever vibration amplitude is increased. Fig. 5.9(a) displays the recorded interference signal from the bulk of the tip (off-apex) for different vibration amplitudes in a 2-D color map plot. For comparison Fig. 5.9(b) shows the interference signals at 30 nm and 240 nm vibration amplitudes.

When the AFM tip vibrates with 30 nm amplitude, the interference signal contains only the 80 MHz and 80 MHz $\pm\,\Omega$ signals. But when the AFM tip vibrates at 240 nm amplitude, the interference signal contains up to $n = 4$ higher orders in addition—giving clear evidence of mechanical anharmonicity in the tip vibration.

Fig. 5.10 demonstrates the effects of too low and too high vibrational amplitudes for the case of a Au pattern on Si. While in Fig. 5.10(b) the amplitude is too low to generate any sufficient s_3 signal, in (d) it is too high and the mechanically induced contribution overwhelms the optical. Only in (c) can the optical material information be clearly observed. (These images where taken in tip-scanning mode and exhibit therefore the

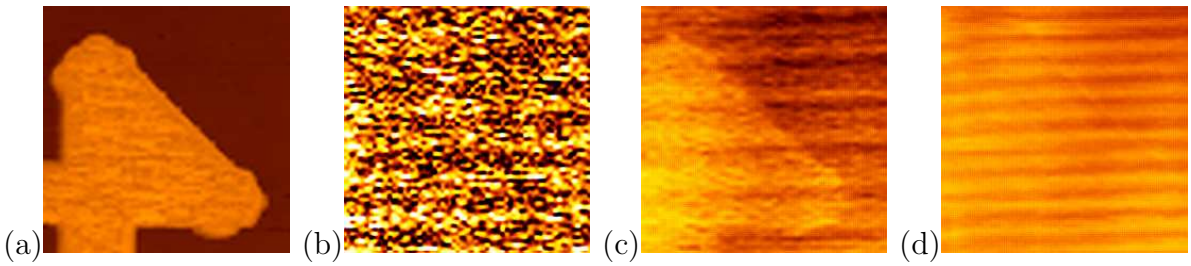

Figure 5.10: 2μm $\times$ 2μm area of an e^--beam lithographically produced Au pattern on Si. (a) topography, (b-d) s_3 near field optical amplitude images acquired in tip-scanning mode with tip vibrational amplitudes of 9nm, 20nm, 80nm respectively.

characteristic envelope modulation of the intensity with the optical excitation intensity in the focus region.)

In conclusion, keeping the AFM cantilever motion as sinusoidal as possible avoids generation of higher order mechanical vibration harmonics which otherwise may lead to unwanted crosstalk with the optical contrast.

Chapter 6

Demonstration of the *a*-SNOM performance

Having built and characterized the *a*-SNOM, I performed investigations with the instrument on samples with sub-wavelength material contrast at the used laser wavelength. The samples were chosen to have a few tens of nm features in order to demonstrate how the *a*-SNOM achieves superior resolution.

I was able to reveal information on the material contrast, resolution limit and one clear indication of a topography induced effect on the image formation of *a*-SNOM with these experiments.

6.1 *a*-SNOM imaging at various demodulation orders

In this section the *a*-SNOM performance at increasing demodulation orders is demonstrated by using a nanosphere lithographically (NSL) patterned [97] Au structure on glass with nm-sized features. As these images exhibit a number of interesting features to be discussed later they are presented here in a concise overview and will also be referred to in the following sections.

The Au pattern was created by deposition of $0.58\,\mu$m diameter latex beads on a glass surface and evaporation of a 40 nm thick gold layer, leading to a hexagonal gold coating pattern at the interstitial gaps with characteristic trigonal shapes, and continuous islands of gold at places which were not covered with latex spheres. In this way the beads were used as a shadow mask to pattern the metal coating on the surface. When the coated latex beads were lifted off the surface, there remained a finely structured metal pattern on these interstitial gaps with sharp corner features.

The 632.8 nm wavelength, randomly polarized HeNe laser had a coherence length well above 1 cm, as determined by changing the optical path difference in the reference beam of the interferometer. By tuning the AOM driver frequency ω the AOM was operated such that $\omega + n \times \Omega \simeq 80\,\mathrm{MHz}$, shifting the desired frequency into the pass band of the SAW filter. The laser illumination was delivered to the setup through a single mode optical fiber which acted also as a spatial filter for obtaining Gaussian field distribution. The laser was coupled to the optical fiber with an 8° tilt coupler to minimize back reflection into the laser. The signal beam of the interferometer had a diameter of 4 mm before the final focusing lens and the reference beam had a diameter of about 2 mm. The diameters were different because the 2 mm diameter was optimal for the AOM operation but the final focusing lens had an aperture of 4 mm. In order to achieve tightest possible focus, I expanded the beam from 2 mm to 4 mm diameter by using a double lens system. The first beamsplitter was a cube beamsplitter with 50/50 splitting ratio, whereas the other beamsplitter was a thin film beamsplitter with the same splitting ratio. The illumination power was 0.8 mW on the sample and the reference beam power was 0.1 mW on the detector. The detector was an avalanche photodiode.

A 10 nm Au coated Advantec Si tip with a resonance frequency of $\Omega = 320\,\mathrm{kHz}$ was used as the apertureless probe. The dynamic mode tip vibration amplitude was 15 nm at the AFM feedback condition. The free space tip vibration amplitude was 16 nm, meaning that the feedback amplitude to free space amplitude had a $15/16 > 90\%$ ratio

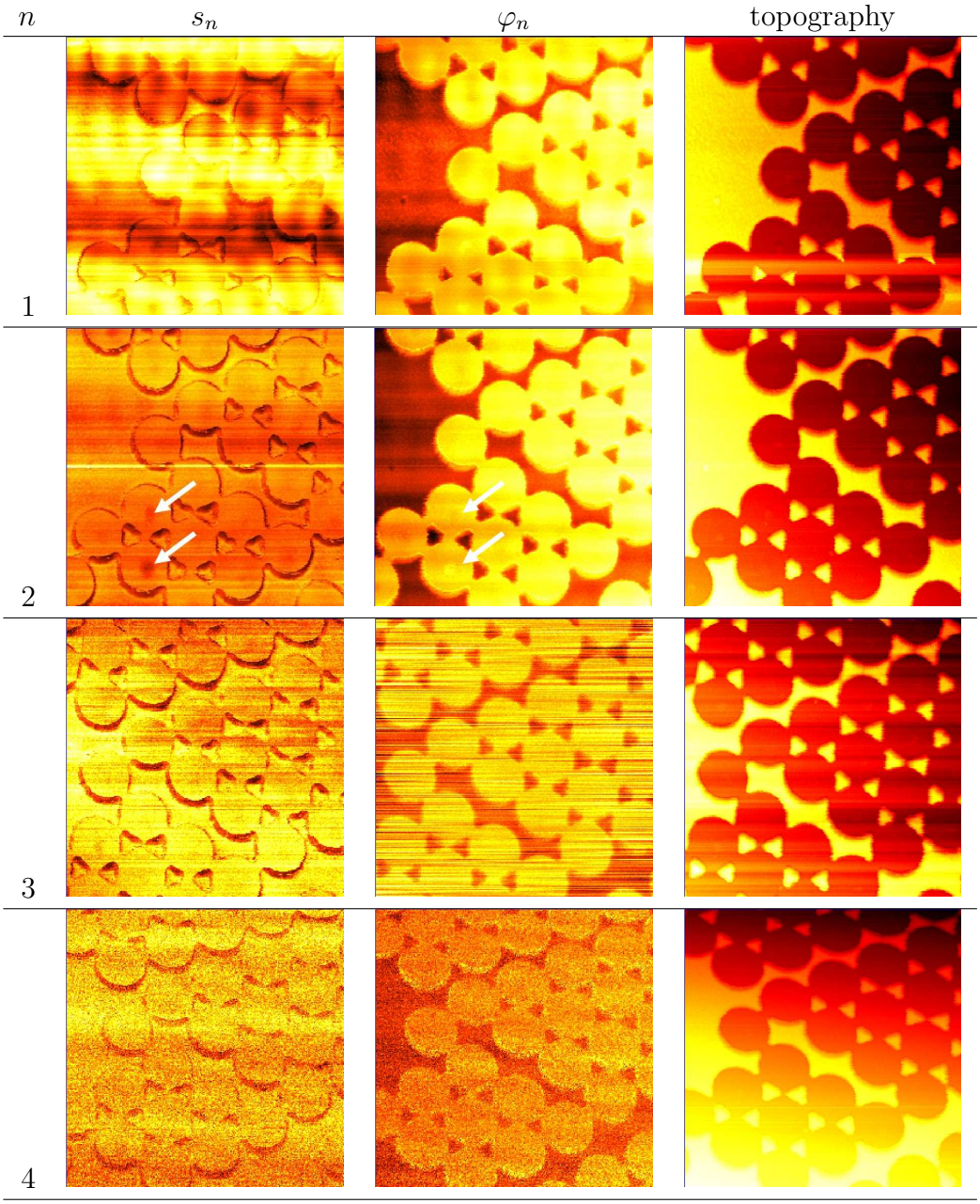

Figure 6.1: *a*-SNOM scans of $3\mu\text{m} \times 3\mu\text{m}$ sample area at $n\Omega$ demodulation, $n = 1, 2, 3, 4$. Shown are the optical amplitude and phase and the topography image. The arrows indicate locations of left-over material from the latex beads at places where the beads were in contact with the glass substrate.

which was crucial for operation with minimal mechanical anharmonicity. The scan speed was 1.5 sec/line and the scan size was $3\mu\text{m} \times 3\mu\text{m}$.

Fig. 6.1 shows an overview of optical amplitude and phase as well as topography images of a representative area acquired at 1Ω, 2Ω, 3Ω, and 4Ω demodulations. For each demodulation frequency, shown are the optical amplitude s_n and phase φ_n as well

as the AFM topography. For all images in this section, the raw data are presented, with the exception of phase images φ_n, in which case a post-acquisition line by line background subtraction is applied. Since lock-in acquisition generates phase data in the $[-180°, +180°]$ domain, at regions in which a $\pm 180°$ cross over takes place, an additional $360°$ was added to the raw data and line correction was applied afterwards.

Fig. 6.1 shows how the $n = 1$ images are dominated by the linear reflections and shadowing contributions from the bulk of the tip, while in the higher orders this parasitic scattering is better suppressed as expected. At fourth order, the amplitude signal contrast is basically diminished below detectability and only some topography-related artifacts at steps are observed (Sec. 6.5.) The phase contrast, however, is still quite well detected.

6.2 Detection of purely near field optical signals

In the following I outline three possible verifications of true near field optical contrast. First and quite elementary, off-apex illumination must show a dramatic effect on the optical information obtained, as the near field optical contribution is effective turned off. Another fundamental check is the improved image quality at higher demodulation order (as long as signal intensity is not too low). Finally, as was presented in Sec. 3.1.2, the optical near fields should appear very confined to the sample surface under investigation. Therefore, approach curves, which exhibit a strong increase of the optical signal only for tip sample distances of a few nm or less are another clear indication of the true near field optical nature of the detected signal.

6.2.1 Off-apex-illumination check

Fig. 6.2 compares images taken with conditions identical to those used in the acquisition of Fig. 6.1 with one exception; the illumination beam was targeted away from the apex of the AFM tip to the body of the cantilever. This way, the near-field optical tip-sample interaction was essentially turned off.

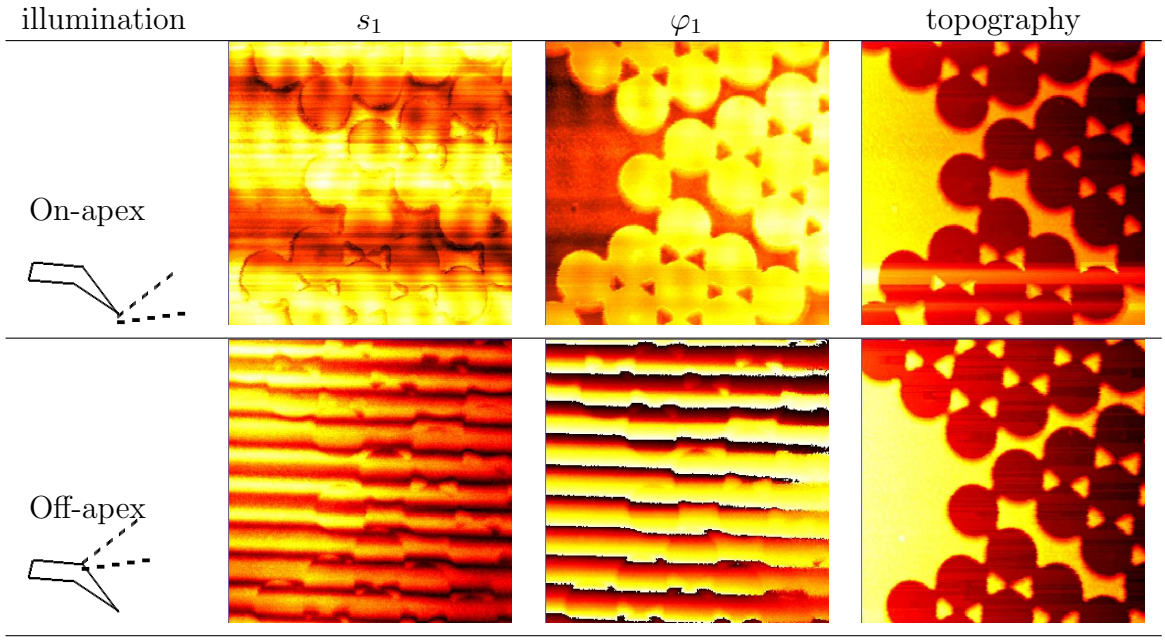

Figure 6.2: *a*-SNOM scans of $3\mu\mathrm{m} \times 3\mu\mathrm{m}$ sample area at 1Ω demodulation. The upper line is the set of 1Ω images from Fig. 6.1. The lower line was obtained under *identical* experimental conditions, but the excitation beam was focussed at the top of the cantilever, not at the apex.

In the off-apex amplitude image, a long range interference pattern on the entire image can be observed particularly on the left half of the image which is an extended flat plateau. It shows that topography adds only a constant far field shift to the amplitude which remains also constant over the same elevation. Therefore, one can conclude that topography mostly adds a far field component. It shows a behavior expected for optical path difference changes. The optical phase in the off-apex illumination shows an opposite contrast with respect to phase images taken at all demodulations with regular *a*-SNOM operation in Figs. 6.1, which gives another evidence that the strong deviation of the optical phase in the near field of the surface with respect to the far field phase can be detected interferometrically by an apertureless probe. Another observation is the absence of the shadowing artifact due to topographical edges. This establishes yet another proof that the features observed at the images are genuinely resulting from the interaction of light with the tip-sample system at the very apex of the tip.

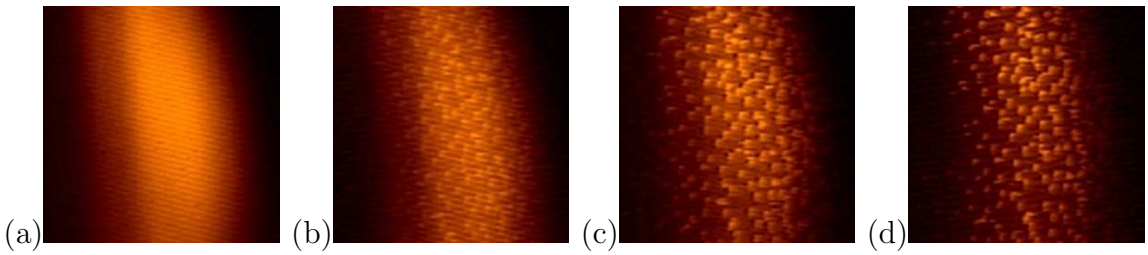

Figure 6.3: Optical amplitude images of a 10μm square area of Ag colloids on a Si substrate acquired in high-speed overview tip-scanning mode. (a) s_1, with the sample retracted, shows the field strength envelope in the optical focus. (b-d), with the sample in contact, show the s_1, s_2, s_3 optical amplitudes recorded at $1\Omega - 3\Omega$ demodulation frequencies. Clearly, the far field contribution dominates the s_1 image, but is efficiently suppressed in the s_3 image.

6.2.2 Anharmonic near field contrast enhancement

The far field contribution to the detected interferometric signal can be suppressed by demodulating the detected signal at the AFM cantilever frequency and its harmonics. As the demodulation is done at higher harmonics an improved near field contrast is obtained. In Fig. 6.3, the AFM tip (5nmCr/15nmAu coated AdvanTec Si tip with $\Omega \simeq 530$kHz) scans an area of $10\mu\text{m} \times 10\mu\text{m}$. The sample is a Si surface hosting Ag colloids of 20nm diameter with low coverage. The scans are done in tip scanning mode for fast overview and show therefore the characteristic amplitude envelope of the optical focus as measured in (a) with the sample removed. The interferometric detection of the scattered beam is demodulated at the cantilever frequency and the signal (s_1) is recorded. In (b) the sample is engaged by the AFM and as for (a) s_1 is recorded. This image shows that the colloids do produce more signal than the Si substrate, but there is still some far field contribution on the overall image. In (c) and (d) the recorded signals are s_2 and s_3 respectively. With the increasing demodulation order, the background signal reduces, leaving enhanced contrast from the near field of the sample.

6.2.3 Complex-optical approach curves

In section 3.1.2, an analysis of the scattered near field by a small dynamic sphere was made by calculating the field amplitude and phase at different sphere heights as it was

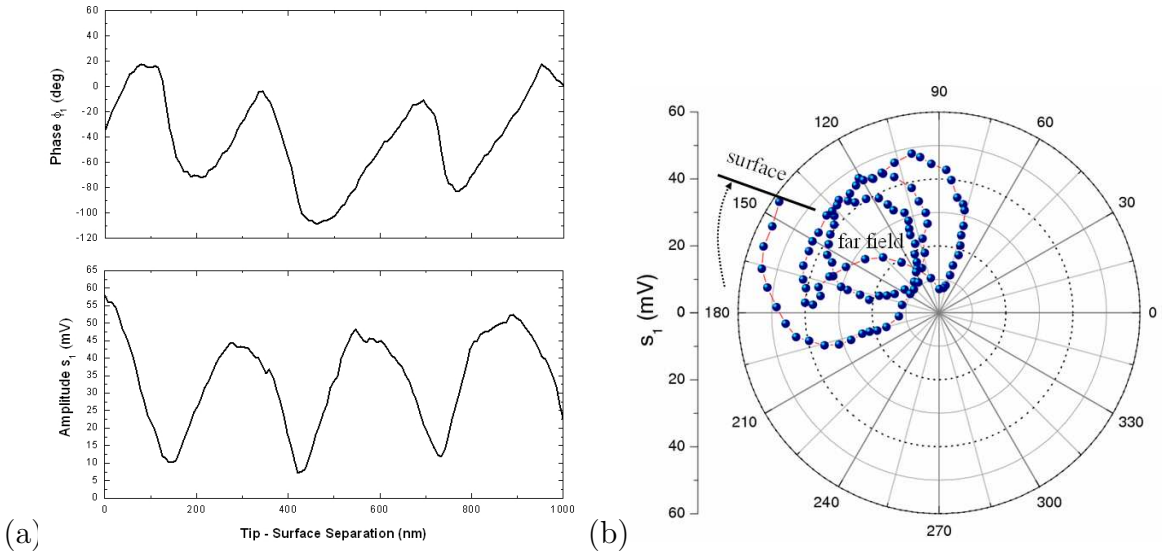

Figure 6.4: (a) Amplitude (s_1) and phase (φ_1) approach curves at the tip frequency demodulation. (b) Polar plot of the same information.

approaching a surface (Fig. 3.7). The small sphere was chosen as a model object to represent an *a*-SNOM tip apex approaching a sample surface irradiated with an optical field. As a demonstration for the effect of detected near field in *a*-SNOM experiments, I acquired complex approach curves which show the expected behavior.

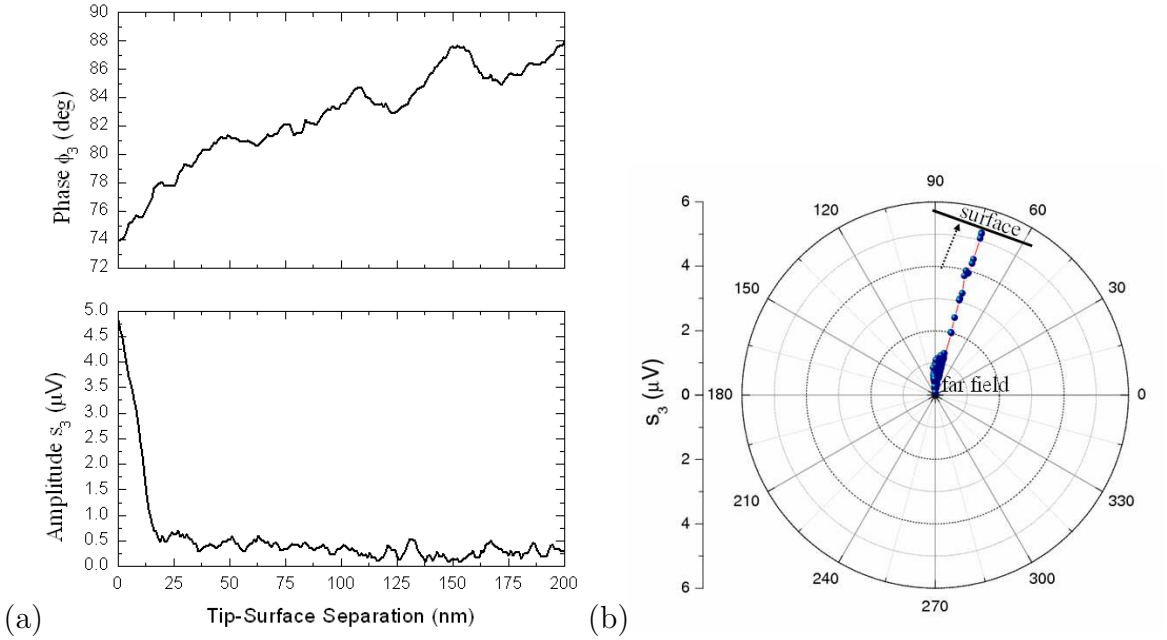

Figure 6.5: (a) Amplitude (s_3) and phase (φ_3) approach curves at the tip frequency demodulation. (b) The polar plot shows shows that a strong amplitude emerges at the near field of the surface.

In Fig. 6.4, the detected optical amplitude (s_1) and phase (φ_1) at the tip vibration

frequency 1Ω as the *a*-SNOM tip approaches a Au surface is displayed. A long-distance modulation observed in both the amplitude and phase, as the sample is approaching the tip. This is a result of spatially interfering incoming and reflected far field detected in the 1Ω demodulation. In (b) the same data is shown in a polar plot, which shows how the near field is hardly detectable compared to the far field contributions.

Fig. 6.5, a similar approach curve is presented as in Fig. 6.4, only for third harmonic demodulation. At large tip-sample distances almost no amplitude signal is observed and the phase exhibits a small unspecified drift. As the sample approaches the tip closely, to less than 20nm, a marked increase in the amplitude is observed, due to the near field optical signal setting in.

In summary, approach curves are an essential and easily performed test for true near field optical contrast. They have proved to be a valuable tool for detecting faulty experimental conditions and correcting them.

6.3 Spatial resolution in amplitude and phase near field optical images

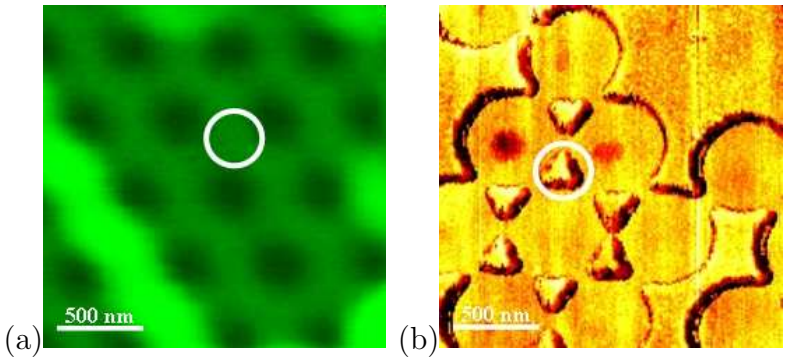

Figure 6.6: NSL patterned Au sample imaged with (a) confocal laser scanning microscopy (b) *a*-SNOM at 2Ω demodulation after line-by-line subtraction of linear components. The circles mark equivalent areas on the images. Au island inside the circle is resolved with superior spatial resolution in (b) where a similar island appears as a blurred lobe in (a).

The main objective of a near field optical microscope is to increase the spatial resolution beyond what is possible with reflective/diffractive far field optical microscope.

The most promising advantage of *a*-SNOM is that the spatial resolution is limited only by the AFM tip apex diameter, which can be as small as a few nm in case of AFM tips. This statement holds independently of wavelength, in contrast even with apertures of standard SNOM instruments, whose diameter is limited to about $\lambda/20$ in the best of cases. The strong confinement of the near field which extends about the radius of the tip makes it possible to achieve generally tip limited resolution.

A direct comparison of the performance of *a*-SNOM and a confocal far field microscope is given by Fig. 6.6, which shows images of two similar regions on the sample already discussed in Fig. 6.1. Both images where obtained with the same illumination laser frequency. Whereas the scanning laser confocal microscope image appears blurred and does not resolve the local structure, the *a*-SNOM faithfully resolves the triangular shaped gold islands.

In general, as the *a*-SNOM not only records the optical field strength but also its phase, the resolution can be tested in both amplitude and phase images. In many of the images I recorded, I observed a better sensitivity in the phase images than in the amplitude. Consequently, the best indications for optimal spatial resolution I obtained in phase images. In the following I discuss both.

Spatial resolution of *a*-SNOM can be studied very well on small feature size samples. For that reason I chose to image metal colloids deposited on a dielectric surface. The sample was a Si surface covered with Ag colloids of nominal 20nm diameter.[1]

Amplitude spatial resolution

In Fig. 6.7 the optical amplitude lateral resolution is studied with Ag colloids deposited on Si. The imaging tip in this case was an uncoated Si AdvanTec tip that evidently had already been slightly degraded, predominantly along the x-direction. Therefore,

[1]The colloids were brought onto the surface from a water based colloidal solution (Pelco Inc.). A polished Si surface was first cleaned with acetone and isopropanol by sonication. Then the surface was treated with 0.01% DAS (Sigma-Aldrich, 97%) (aq) for 5 minutes which served as an immobilizer for the colloids on the surface. The surface was then rinsed with deionized water and placed in the colloidal solution for 10 minutes. Afterwards the surface was rinsed again with deionized water and nitrogen blown. The surface coverage was controlled by the time the sample is left in the colloidal solution, provided that the solution had enough colloid material.

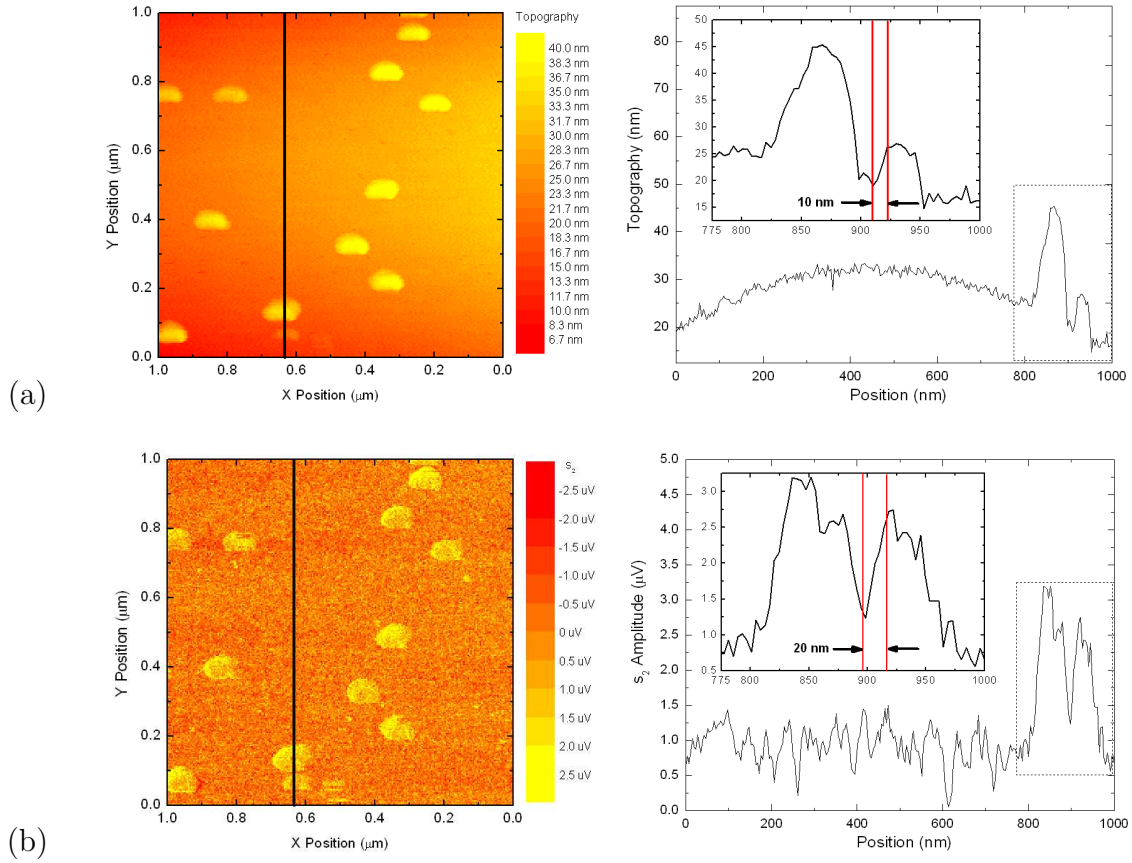

Figure 6.7: A 1μm $\times$ 1μm scan of nominally 20nm diameter Ag colloids deposited on Si. (a) Topography (b) optical s_2 signal.

the resolution along the y is analyzed. Cuts along the vertical lines indicated in (a) and (b) are displayed on the right. Two closely spaced colloids are located on the right of these line scans, one being slightly smaller than the other, as witnessed by the different heights. In the optical image, however, both of them give similarly strong signals, and are thereby clearly identified as gold. Notice how the optical signal is not dependent on the topography but only on the material. The spatial resolution of the two objects is slightly worse in the optical signal than in the topographical. It can be estimated to be around 20nm, which is to be expected in accordance with the slightly dulled tip apex radius.

A further optical amplitude resolution study is made on SiO_x grown Si sample. The sample is cut and polished. The polished edge is scanned with a 5nm Cr + 10nm Au coated Si AdvanTec tip. Fig. 6.8 part(a) shows an optical s_2 (left) and a topography (right) image of a 500nm $\times$ 500nm area for overview. In part (b) zooms to the marked

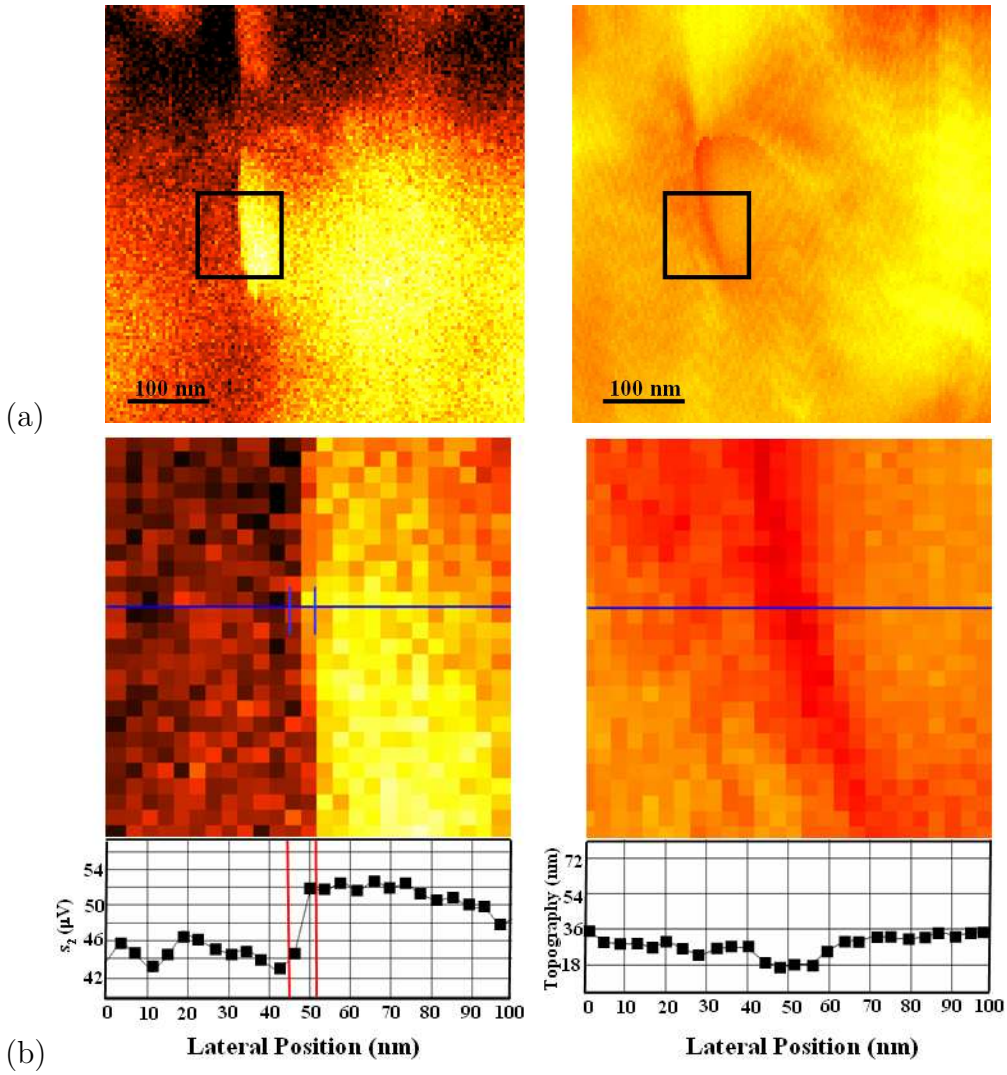

Figure 6.8: (a) A 500nm × 500nm scan of SiO_x grown Si substrate polished edge. Left: Optical s_2 signal, Right: Topography, (b) 100nm × 100nm zoom to the marked areas. The line plots given at the bottom of each image belong to the marked positions in the images.

areas in (a) with 100nm × 100nm dimensions are displayed respectively. Line plots of optical amplitude and topography are given at the bottom corresponding to the marked lines in the images. In the zoomed area a clear material interface is recognized from the optical amplitude change, whereas in topography such a material can not be determined. One finds an optical s_2 amplitude lateral resolution of about 2 pixels $\approx$ 8nm as marked between the red vertical lines. In the topography, no such sharp interface feature appears.

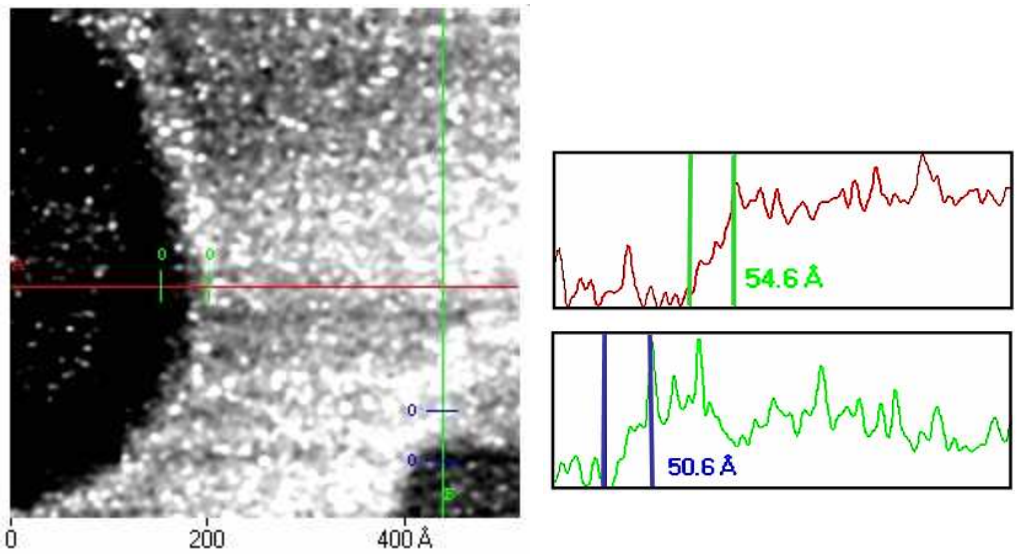

Figure 6.9: On the left a 50nm × 50nm phase image made on Ag colloid deposited silicon surface is displayed. On the right are the line scan data belonging to the marked positions on the image.

Phase spatial resolution

A 50nm × 50nm phase image is presented in the left part of the Fig. 6.9. The dark areas correspond to two Ag colloids. On the right hand side of the figure, line scans corresponding to the lines on the image are displayed. It can be noticed from the line scans that the near field phase of Ag colloid develops within approximately 5nm, which manifests the sharpness of the near field confinement.

Ideally, for a true resolution test a perfectly flat sample with a sharp lateral material contrast is required to avoid the morphological convolution of the tip shape with the image being sampled. For objects of diameter ≈ 20nm such as these colloids this convolution results in a larger effective diameter imaged. Here, a cross sectional diameter of the scanning AFM tip of about 25 to 30nm (at the 10nm height where tip and colloids touch) results in an image diameter of slightly less than 50nm. Therefore an optical resolution of 5nm can not be claimed with confidence, but the actual optical resolution can be estimated to be considerably less than the imaged object's size, i.e., < 20nm.

6.4 Material contrast from complex optical near fields.

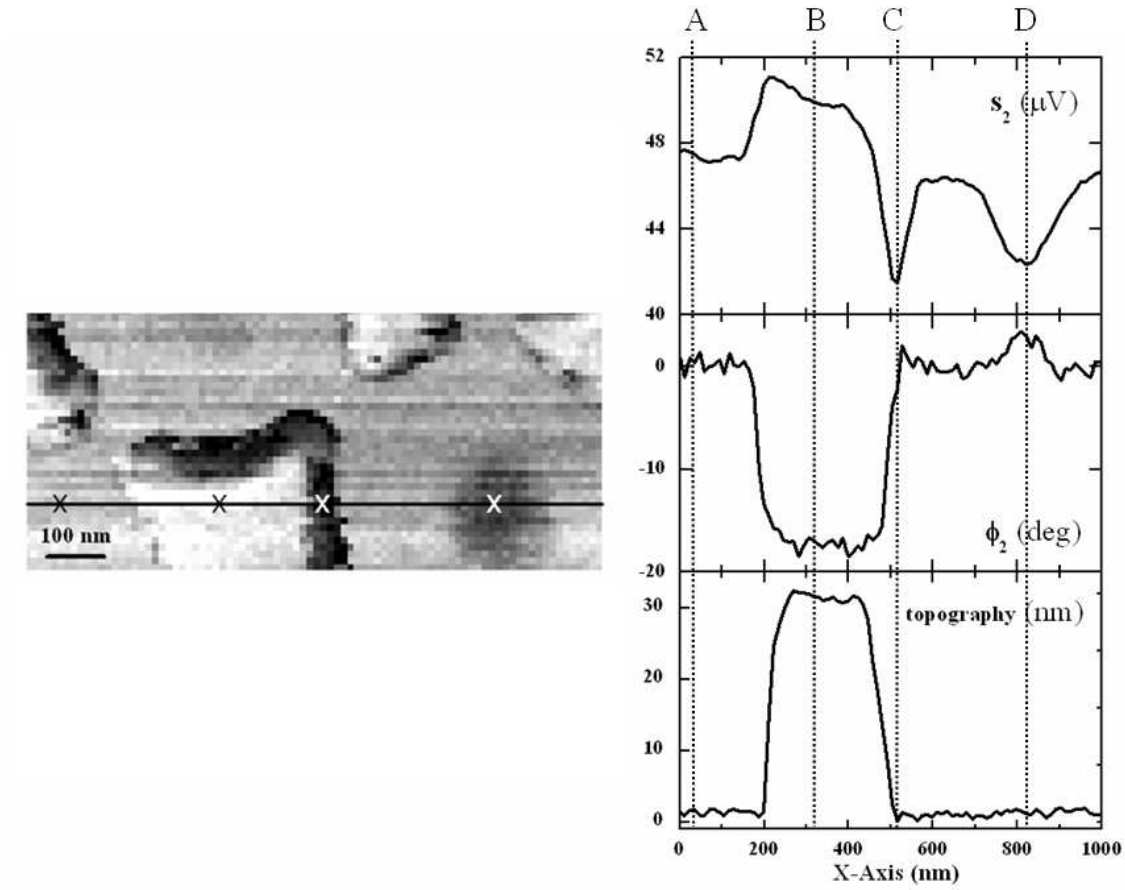

Figure 6.10: The figure shows a 1μm $\times$ 450nm zoom-in on the s_2 image of Fig. 6.1. On the right, topographical and optical amplitude and phase information are displayed for the horizontal line cut indicated on the left image.

In a few places in the Fig. 6.1 images such as at bottom left quadrant of the s_2 image leftovers from the latex spheres located before lift-off are detected, offering excellent opportunities to demonstrate how the *a*-SNOM can provide additional material information not accessible by any other means.

As indicated in Fig.6.10, I discuss four significant locations: (A) the glass substrate, (B) the slightly elevated Au islands, (D) leftover material from the latex spheres, and (C) a geometrical artifact, which is discussed in Sec. 6.5.

Compared to the substrate (A), the Au islands (B) exhibit a stronger near field optical amplitude – in full accordance with the behavior expected from the material

contrast calculated with the dipole model of Sec. 3.1.2 – and a negative shift in the phase by some 17°. At the center of the circular shadows left during Au evaporation by the latex sphere masks, occasionally, a different optical signal is detected (D), again in agreement with the dipole model (Sec. 3.1.2). This is presumed to be due to minute amounts of leftover latex material. Notice how the topographic information does not reveal any structural changes at such locations. But the optical amplitude is reduced compared to the Si levels and the phase is increased by about 4°.

This clear evidence for a very sensitive material-related contrast in *a*-SNOM offers exciting prospects for its application to material science, considering in particular how little material is detected at location (D) in Fig. 6.1, if it is not picked up in the topographical contrast.

6.5 Geometrical artifacts

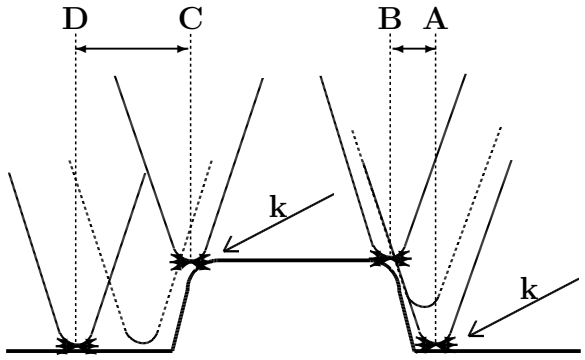

Figure 6.11: Sketch of the shadow effect on imaging is displayed by help of a ridge like topographical structure. The vectors labelled k show the incident beam propagation direction. On the positive slope side of the ridge, between positions A and B, tip-sample interaction is hindered due morphology as illustrated, resulting in a low signal region between A-B. On the negative slope side, between positions C and D, the illumination of the tip-sample system is shadowed by topography, which results in a low signal region between C-D.

Another observation can be made in the images of Fig. 6.1 regarding the near-field amplitude at the edges of gold islands and plateaus. Apparently, some artifact mechanism leads to the decoration of the edges with dark rims in the amplitude images. They can be explained as simple geometrical consequences of the near field enhancing

tip apex temporarily losing contact as well as shadowing.

The illumination laser was incident on the surface at an oblique angle of 30° entering from the bottom of the images into the image plane as displayed in Fig. 6.1. In this configuration, a relatively large shadowing effect appears on the upper edges of the Au islands due to the oblique nature of the illumination. Notice that the collection of the tip-sample interaction was also made with the same lens as the illumination lens in back-scattering direction.

In addition, smaller dark zones are observed at the other parts of the island rims, due to the temporary loss of contact of the apex with the substrate; instead parts of the tip side walls are in contact with the sample. Fig. 6.11 illustrates these effects on imaging. The vectors labelled by k show the incident beam propagation direction. On the positive slope side of the ridge, between positions A and B, tip-sample interaction is hindered due to convolution between the tip and sample geometry, resulting in a low signal region between A-B. In this range, surface of the sample in contact with the tip is not below the apex of the tip but resides at the back side of the tip with respect to k. On the negative slope side, between positions C and D (tip shown in dashed line), the illumination of the tip-sample system is shadowed by topography, which results in a low signal region between C-D. The vector k shows the incident beam direction.

Chapter 7

Conclusion

In this thesis, I proposed, realized and characterized an apertureless scanning near field optical microscope abbreviated as *a*-SNOM. The technique was based on utilizing a metallic or dielectric AFM tip with a sharp apex as a local probe on a surface illuminated at an oblique angle. The AFM tip was let to interact with the surface in a dynamic fashion by vibrating the tip cantilever at its resonance frequency. The resulting scattered field amplitude originating from the very local interaction zone as small as the tip apex, was elevated to detectable levels by means of interferometrical amplification. The heterodyne interferometry method has the added benefit that it allows to obtain both local optical amplitude and phase information. Use of coherent, monochromatic laser sources together with a lock-in amplifier based detection scheme resulted in a sensitive instrument to to detect optical near fields. The parasitic scattering generated at illuminated surfaces other than the tip apex were effectively suppressed by demodulating the detected scattering amplitude at higher harmonics of the vibration frequency of AFM cantilever.

I performed systematic characterization experiments to assess the performance of the *a*-SNOM. These characterization experiments yielded information regarding the illumination source power stability, coherence, cantilever dynamics, generation of high harmonics, optical alignment, stability of the interferometer, tip-sample approach, spatial resolution, simultaneous amplitude, phase and topography acquisition, tip versus

sample scan, suppression of parasitic scattering by higher harmonics demodulation, cantilever drive and amplitude effects on image formation. These experiments have shown that the sensitivity of the instrument relies on the coherence of the illumination source. The optical path length difference has to stay below the coherence length of the source in the interferometry setup, which was measured to be around 1 to 2cm in my case. Another outcome of these characterization experiments is that care has to be taken not to excite the high harmonics of AFM cantilever by applying too strong drive forces as the higher harmonics amplitude components should exclusively result from the sharply confined near field at the surfaces free from any mechanical signal crosstalk. Another observation is that the tip scan and sample scan modes result in principally identical results with a factor of illumination beam focus convolution in the tip scan mode which could successfully be nullified in the sample scanning operation mode. I was able to acquire the near field optical amplitude and phase data together with topography simultaneously from surfaces. The field amplitude above the detection noise background in the near field zone of a gold surface is shown to be confined to within 10nm proximity of the surface, which implied a resolution limit of 10nm is possible with respectively small AFM tip radius. The theoretical prediction of parasitic scattering suppression by higher cantilever frequency harmonics demodulation has also proven to be effective with these characterization experiments.

a-SNOM investigations were undertaken of nano-structured surfaces such as NSL patterned gold nets on glass. In the light of the results of performance tests, the *a*-SNOM operation conditions were selected carefully for problem free operation to remove any sources of avoidable artifacts. In these experiments material dependent near field contrast was observed. The spatial resolution was found to be ~ 8nm, i.e., well below the optical diffraction limit and better than the resolution of aperture based SNOMs. It was found to depend critically on the AFM tip sharpness. Optical phase images indicate that even ~ 5nm resolution should be possible.

In addition, the features in near field images when compared to the simultaneously

acquired topography images showed that the oblique incidence nature of the illumination beam results in unavoidable artifacts in areas featuring steep topographical slopes ("dark rims" of islands.) In order to show that all the features obtained in these images genuinely result from the near field optical tip-sample interaction, I conducted the same experiment with an offset illumination beam onto the body of the AFM cantilever from the tip zone. This way all the mechanical interaction effects on the scattered amplitude were kept identical as the near field optical effects were turned off. In this experiment the effects of topography and mechanical interaction of the tip with the sample surface have shown to generate only constant backgrounds in the images which did not vary over long distances, much longer than the near field zone.

As a summary, the *a*-SNOM is shown to be a useful tool to produce sensitive material contrast near field images of the surfaces with a spatial resolution less than the diffraction limit, when operated at carefully selected conditions to avoid mechanical artifacts. The image properties are found to depend on illumination geometry, tip sharpness, and sample material. In addition I demonstrated some topography related artifacts which are necessarily there because of oblique incidence. The *a*-SNOM I constructed has the potential of becoming a routine tool for nano-optical investigations. Experiments possible with kind of instrument beyond what has been demonstrated in this thesis include investigations of spectroscopic material resonances (using tunable excitation lasers), optical antenna effects, polarization effects such as electro-optics, magneto-optics, etc.

Bibliography

[1] G. Binnig and H. Rohrer, Helvetica Physica Acta **55**, 726 (1982).

[2] G. Binnig, C. F. Quate, and C. Gerber, Phys. Rev. Lett. **56**, 930 (1986).

[3] M. Minsky, US Patent 3,013,467 (1961).

[4] G. J. Brakenhoff, Journal of Microscopy-Oxford **Nov**, 233 (1979).

[5] S. Chandra, E. P. W. Kable, G. H. Morrison, and W. W. Webb, Journal Of Cell Science **100**, 747 (1991).

[6] H. M. Wang, A. Bardo, M. M. Collinson, and D. A. Higgins, J. of Phys. Chem. B **37**, 7231 (1998).

[7] J. S. Avery, Proceedings of the Physical Society of London **559P**, 1 (1966).

[8] E. H. Synge, Phil. Mag. **6**, 356 (1928).

[9] E. A. Ash and G. Nicholls, Nature **237**, 510 (1972).

[10] D. W. Pohl, W. Denk, and M. Lanz, Appl. Phys. Lett. **44**, 651 (1984).

[11] A. Lewis, M. Isaacson, A. Harootunian, and A. Muray, Ultramicroscopy **13**, 227 (1984).

[12] E. Betzig *et al.*, Science **251**, 1468 (1991).

[13] H. A. Bethe, Phys. Rev. **66**, 163 (1944).

[14] Y. Inouye and S. Kawata, Opt. Lett. **19**, 159 (1994).

[15] R. Bachelot, P. Gleyzes, and A. C. Boccara, Optics Letters **20**, 1924 (1995).

[16] L. Novotny, E. J. Sánchez, and X. S. Xie, Ultramicroscopy **71**, 21 (1998).

[17] K. Dickmann, J. Jersch, and F. Demming, Surface And Interface Analysis **25**, 500 (1997).

[18] S. Nie and S. R. Emory, Science **275**, 1102 (1997).

[19] B. Pettinger, G. Picardi, R. Schuster, and G. Ertl, Electrochemistry (Japanese Electrochemical Society) **68**, 942 (2000).

[20] M. S. Anderson, Appl. Phys. Lett. **76**, 3130 (2000).

[21] B. Pettinger, G. Picardi, R. Schuster, and G. Ertl, Single Molecules **3**, 285 (2002).

[22] R. Stockle, Y. Suh, V. Deckert, and R. Zenobi, Chem. Phys. Lett. **318**, 131 (2000).

[23] N. Hayazawa, Y. Inouye, Z. Sekkat, and S. Kawata, Optics Communications **183**, 1 (2000).

[24] M. Fleischmann, P. J. Hendra, and A. J. Mcquillan, Chem. Soc. Chem. Commun. **80**, (1973).

[25] M. Fleischmann, P. J. Hendra, and A. J. Mcquillan, Chem. Phys. Lett. **26**, (1974).

[26] D. L. Jeanmaire and R. P. Van Duyne, J. of Electroanal. Chem. **84**, (1977).

[27] A. Hartschuh, E. J. Sanchez, X. S. Xie, and L. Novotny, PRL **90**, 095503 (2003).

[28] M. Ashino and M. Ohtsu, Appl. Phys. Lett. **72**, 1299 (1998).

[29] Y. Kawata, C. Xu, and W. Denk, Journal of Applied Physics **85**, 1294 (1999).

[30] F. Zenhausern, Y. Martin, and H. K. Wickramasinghe, Science **269**, 1083 (1995).

[31] R. Hillenbrand, Ph.D. thesis, Technische Universität München, 2001.

[32] B. Knoll, F. Keilmann, A. Kramer, and R. Guckenberger, Appl. Phys. Lett. **70**, 2667 (1997).

[33] B. Knoll and F. Keilmann, Appl. Phys. A **66**, 477 (1998).

[34] F. Keilmann, B. Knoll, and A. Kramer, physica status solidi (b) **215**, 849 (1999).

[35] B. Knoll and F. Keilmann, Appl. Phys. Lett. **77**, 3980 (2000).

[36] R. Hillenbrand, T. Taubner, and F. Keilmann, Nature **418**, 159 (2002).

[37] R. M. Bright, D. G. Walter, and *et al.*, Langmuir **12**, 810 (1996).

[38] Z. Q. Tian, B. Ren, and D. Y. Wu, J. of Phys. Chem. B **106**, 9463 (2002).

[39] R. G. Freeman, K. C. Grabar, and *et al.*, Science **267**, 1629 (1995).

[40] L. A. Bottomley, Anal. Chem. **70**, 425R (1998).

[41] H. K. Wickramasinghe, Acta Materialia **48**, 347 (2000).

[42] L. M. Falicov, D. T. Pierce, and *et al.*, Journal of Materials Research **5**, 1299 (1990).

[43] J. D. Jackson, *Classical Electrodynamics* (Wiley, New York, 1975).

[44] J. L. Heinrich *et al.*, Science **255**, 66 (1992).

[45] L. Novotny, D. W. Pohl, and B. Hecht, Opt. Lett. **20**, 970 (1995).

[46] M. Muranishi, K. Sato, S. Hosaka, and *et al.*, Jap. J. of Appl. Phys. **36**, L942 (1997).

[47] J. A. Veerman, M. F. Garcia-Parajo, L. Kuipers, and N. F. V. Hulst, Journal of Microscopy **194**, 477 (1999).

[48] B. Sick, B. Hecht, U. Wild, and L. Novotny, Journal of Microscopy **202**, 365 (2001).

[49] B. Hecht, Phil. Trans. R. Soc. Lond. A **362**, 881 (2004).

[50] J. Jersch, F. Demming, and K. Dickmann, Appl. Phys. A **64**, 29 (1997).

[51] H. F. Hamann, A. Gallagher, and D. J. Nesbitt, Applied Physics Letters **73**, 1469 (1998).

[52] F. Demming, J. Jersch, K. Dickmann, and P. I. Geshev, Appl. Phys. B **66**, 593 (1998).

[53] Y. Inouye, in *Apertureless Metallic Probes for Near-Field Microscopy* (Springer, Berlin, 2001), Chap. Near-Field Optics And Surface Plasmon Polaritons, pp. 29–48.

[54] F. H'dhili *et al.*, Appl. Phys. Lett. **79**, 4019 (2001).

[55] E. Hecht, *Optics* (Addison-Wesley, Reading, Massachusetts, 1974).

[56] S. W. Hell and J. Wichmann, Optics Letters **19**, 780 (1994).

[57] C. Hettich *et al.*, Science **298**, 385 (2002).

[58] N. Hayazawa, A. Tarun, Y. Inouye, and S. Kawata, Journal of Applied Physics **92**, 6983 (2002).

[59] M. N. Islam *et al.*, Applied Phsics Letters **20**, 2886 (1997).

[60] Y. D. Suh and R. Zenobi, Advanced Materials **12**, 1139 (2000).

[61] E. Betzig and J. K. Trautman, Science **257**, 189 (1992).

[62] K. Karrai and R. D. Grober, Appl. Phys. Lett. **66**, 1842 (1995).

[63] Nanonics Imaging Ltd., Manhat Technology Park, Malcha, Jerusalem, Israel 91487.

[64] S. Roark, D. Semin, and K. Rowlen, Anal. Chem. **68**, 473 (1996).

[65] V. Shalaev and A. Sarychev, Phys. Rev. B **57**, 13265 (1998).

[66] A. Sarychev, V. Shubin, and V. Shalaev, Phys. Rev. B **60**, 16389 (1999).

[67] H. Xu, J. Aizpurua, M. Kall, and P. Apell, Phys. Rev. E **62**, 4318 (2000).

[68] J. Jiang, K. Bosnick, M. Maillard, and L. Brus, J. Phys. Chem. B **107**, 9964 (2003).

[69] B. Pignataro *et al.*, J. Chem. Phys. **113**, 5947 (2000).

[70] R. M. Stöckle, V. Deckert, C. Fokas, and R. Zenobi, Applied Spectroscopy **54**, 1577 (2000).

[71] C. Douketis *et al.*, J. Chem. Phys. **113**, 11315 (2000).

[72] Y. Saito, J. J. Wang, D. A. Smith, and D. N. Batchelder, Langmuir **18**, 2959 (2002).

[73] W. E. Doering and S. Nie, J. Phys. Chem. B **106**, 311 (2002).

[74] K. Kneipp *et al.*, Phys. Rev. Lett. **78**, 1667 (1997).

[75] K. Kneipp *et al.*, Chemical Reviews **99**, 2957 (1999).

[76] K. Kneipp *et al.*, Phys. Rev. B **63**, (2001).

[77] D. Zeisel *et al.*, Anal. Chem. **69**, 749 (1997).

[78] D. Zeisel, V. Deckert, R. Zenobi, and T. Vo-Dinh, Chem. Phys. Lett. **283**, 381 (1998).

[79] R. Stockle *et al.*, Vibrational Spectroscopy **22**, 39 (2000).

[80] W. X. Sun and Z. X. Shen, Mater. Phys. Mech. **4**, 17 (2001).

[81] T. Kalkbrenner, M. Ramstein, J. Mlynek, and V. Sandoghdar, Journal of Microscopy **202**, 72 (2001).

[82] I. S. Averbukh, B. M. Chernobrod, O. A. Sedletsky, and Y. Prior, Optics Communications **174**, 33 (2000).

[83] E. Oesterschulze *et al.*, Journal of Microscopy **202**, 39 (2001).

[84] H. F. Hamann, M. Kuno, A. Gallagher, and D. J. Nesbitt, The Journal of Chemical Physics **114**, 8596 (2001).

[85] K. B. Crozier, A. Sundaramurthy, G. S. Kino, and C. F. Quate, Journal of Applied Physics **94**, 4632 (2003).

[86] J. Borrajo and J. M. Heras, Thin Solid Films **2**, 267 (1973).

[87] L. Brus, Applied Physics A **6**, 465 (1991).

[88] A. Bouhelier, M. R. Beversluis, and L. Novotny, Appl. Phys. Lett. **82**, 4596 (2003).

[89] B. Knoll and F. Keilmann, Optics Communications **182**, 321 (2000).

[90] O. D. Kellogg, *Foundations of Potential Theory* (Springer Verlag, New York, 1967).

[91] S. G. Mikhlin, *Mathematical Physics, an Advanced Course* (North-Holland, Amsterdam, 1970).

[92] D. R. Fredkin and I. D. Mayergoyz, Phys. Rev. Lett. **91**, 253902 (2003).

[93] J. Van Bladel, *Singular Electromagnetic Fields and Sources* (Oxford University Press, Oxford, 1991).

[94] S. Gresillon *et al.*, physica status solidi (a) **175**, 337 (1999).

[95] P. Gadenne *et al.*, Physica B **279**, 52 (2000).

[96] F. J. Giessibl, *Progress in Atomic Force Microscopy* (Universität Augsburg, Augsburg, 2000).

[97] J. C. Hulteen and R. P. Vanduyne, J. of Vac. Sci. and Tech. A **3**, 1553 (1995).

Curriculum vitae

Name:	Alpan Bek
Date of Birth:	March 10, 1975
Nationality	Republic of Turkey
1985–1992	High School at the Anatolian High School at Bornova-İzmir, Turkey
1992–1996	"Bachelor of Science" studies in physics at the Bilkent University, Ankara, Turkey
1996–1998	"Master of Science" studies in physics at the Bilkent University, Ankara, Turkey, MS Thesis: "Low loss optical waveguides and polarization splitters with oxidized $Al_xGa_{1-x}As$ layers"
Dec. 1997–Jun. 1998	Research scholar at the University of California at Santa Barbara, California, USA
Sep. 1996–Sep. 1999	Research and teaching assistant at the Bilkent University, Ankara, Turkey
Sep. 1999–Sep. 2004	PhD student in the group of Prof. Dr. K. Kern at the Max Planck Institute for Solid State Research, Stuttgart, Germany, PhD thesis: "Apertureless SNOM: A new tool for nano-optics"

Acknowledgements

I would like to thank several people for their contributions in this thesis. In particular:

Prof. Klaus Kern for giving me the opportunity to work in the **Max-Planck Institute for Solid State Research**, one of the highest level research institutes in the world, and guiding me through the course of the thesis with his exciting ideas;

Dr. Ralf Vogelgesang (rafl), for EVERYTHING as a mentor and friend;

Wolfgang Heinz, Ulrike Weizmann, Technology Service Group in the institute, for their help in technical design & machining, SEM, and AFM tip metallization, respectively;

Prof. Leiderer, Dr. Christian Klinke, Dr. Roman Sordan, Dr. Giovanni Costantini, for their time and effort in supplying me samples, and the last two also as friends;

my dear friends in the group, **Michael Vogelgesang, (Dr.) Dominik Hoffmann, (Dr.) Mato Knez** (Kollege), **Dr. Alexander Bittner, (Dr.) Xiaouchun Wu, Dr. Klaus Kuhnke, (Dr.) Carlos Manzano, Kannan Balasubramanian** (Kumpel), **Giorgios Katsaros, Diego Repetto, Dr. Alicia Maroto, Ruben Esteban** and **all the others**, for their support, collaboration and a very pleasant time in the institute;

my dear friends outside the group, **(Dr.) Erol Sağol**, (Herr) **Dr. Kaan Güven**, (türk) **Martin Geisler, (Dr.) Erik Ahlswede, Afif & Ayşe Sıddıki, Dr. Mete Atatüre, Koray Atasoy, Arıkan Açar, Burak Agaççıoğlu**, for sharing their time,

support, joy, music, wine and food with me;

Arya Döner, **Mehmet** and **Hekim**, for looking after me and sharing their philosophical thoughts about life and everything during the writing phase of the thesis;

and my beloved **parents İlkgün and Suat, grandparents Muammer and Süeda, brother Efe, aunts Gülgün and Suzan, uncle Recep** and other **relatives**, for being always with me, no matter what their physical condition and coordinates are.